Geoscience Frontiers 15 (2024) 101779

Contents lists available at ScienceDirect

Geoscience Frontiers

journal homepage: www.elsevier.com/locate/gsf

Research Paper

Application of geophysical well logs in solving geologic issues: Past, present and future prospect

Jin Lai [a,b,*], Yang Su [b], Lu Xiao [b], Fei Zhao [b], Tianyu Bai [b], Yuhang Li [b], Hongbin Li [b], Yuyue Huang [b], Guiwen Wang [a,b], Ziqiang Qin [c]

[a] National Key Laboratory of Petroleum Resources and Engineering, China University of Petroleum (Beijing), Beijing 102249, China
[b] College of Geosciences, China University of Petroleum (Beijing), Beijing 102249, China
[c] Department of Petroleum Engineering, University of Wyoming, Laramie, WY 82071, USA

ARTICLE INFO

Article history:
Received 9 August 2023
Revised 21 November 2023
Accepted 3 January 2024
Available online 6 January 2024
Handling Editor: Richard Damian Nance

Keywords:
Geophysical well logs
Sequence stratigraphy
Source rock
Unconventional oil and gas resources
Artificial intelligence

ABSTRACT

Geophysical well logs are widely used in geological fields, however, there are considerable incompatibilities existing in solving geological issues using well log data. This review critically fills the gaps between geology and geophysical well logs, as assessed from peer reviewed papers and from the authors' personal experiences, in the particular goal of solving geological issues using geophysical well logs. The origin and history of geophysical logging are summarized. Next follows a review of the state of knowledge for geophysical well logs in terms of type of specifications, vertical resolution, depth of investigations and demonstrated applications. Then the current status and advances in applications of geophysical well logs in fields of structural geology, sedimentary geology and petroleum geology are discussed. Well logs are used in structural and sedimentary geology in terms of structure detection, *in situ* stress evaluation, sedimentary characterization, sequence stratigraphy division and fracture prediction. Well logs can also be applied in petroleum geology fields of optimizing sweet spots for hydraulic fracturing in unconventional oil and gas resource. Geophysical well logs are extending their application in other fields of geosciences, and geological issues will be efficiently solved via well logs with the improvements of advanced well log suits. Further work is required in order to improve accuracy and diminish uncertainties by introducing artificial intelligence. This review provides a systematic and clear descriptions of the applications of geophysical well log data along with examples of how the data is displayed and processed for solving geologic problems.

1. Introduction

Geophysical well logs are important for hydrocarbon formation evaluation and resource assessment, groundwater, mineral deposit, and geothermal energy, as well as engineering and paleoclimate or paleoenvironmental research (Kana et al., 2015; Zhang et al., 2018; Farrag et al., 2019; Shan et al., 2021; Lai et al., 2023a). The continuous recordings of geophysical parameters (acoustic, electrical and nuclear properties) along borehole produce geophysical well logs (Carrasquilla and Lima, 2020; Lai et al., 2023a). Wireline geophysical well logs are continuous and sophisticated records of geophysical properties of boreholes, and include abundant geological information (Farrag et al., 2019; Carrasquilla and Lima, 2020; Marzan et al., 2021; Lai et al., 2022). Due to economic and technical problems, the (side-wall) cores and cuttings are very limited (Lai et al., 2017). In addition, the core data from mechanical coring have limitations of high cost, lack of orientation and low recovery rate (Khoshbakht et al., 2012; Zazoun, 2013; Aghli et al., 2016). Conversely, well logging, which measure acoustic properties (sonic transit time and sonic amplitudes), nuclear properties (natural radioactivity, Compton scattering, photoelectric effect), electrical properties (resistivity, dielectric log) and other petrophysical properties (temperature, pressure, etc) of rocks, have evident advantages of continuous data acquisition, high vertical resolution, low cost and even orientability (Ji et al., 2022; Lai et al., 2022). Therefore, for wells or intervals lacking core control, well logs are needed to solve geological issues (Ozkan et al., 2011; Al-Mudhafar, 2020; Carrasquilla and Lima, 2020; Marzan et al., 2021).

* Corresponding author at: China University of Petroleum (Beijing), 18 Fuxue Road, Changping, Beijing 102249, China.
E-mail address: sisylaijin@163.com (J. Lai).

https://doi.org/10.1016/j.gsf.2024.101779

Well logs are important subsurface mapping techniques for geologists, and help petrophysicist quickly find the hydrocarbon bearing reservoirs, and can provide complementary data for surface seismic analysis for geophysicists, additionally give insights into hydraulic simulator for a reservoir engineer (Ellis and Singer, 2007; Marzan et al., 2021; Lai et al., 2023a; Podugu et al., 2023). Well logs are widely used in various aspects of earth science since its initial invention by Conrad Schlumberger and Henri Doll in 1927 in France. Over the past decades, well log data, which comprise a series of conventional well logs, electrical and sonic image logs, geochemical Elemental Capture Spectroscopy (ECS) log, array acoustic log, and nuclear magnetic resonance (NMR) log are widely used in the discipline of structural geology (Laubach et al., 2004; Ameen, 2016), sequence stratigraphy (LaGrange et al., 2020; Magalhães et al., 2020), sedimentology (Folkestad et al., 2012; Xu et al., 2015), petroleum geology (Dixit et al., 2017; He et al., 2019; Zhao et al., 2019), petroleum engineering (Avanzini et al., 2016; Iqbal et al., 2018), and unconventional oil and gas resource evaluation (Josh et al., 2012; Shalaby et al., 2019; Lai et al., 2022). However, though the continuous and high vertical resolution well log data contain abundant geological information, there are considerable incompatibilities between well logs and geological characteristics (Lai et al., 2023a). In addition, well log data need fine interpretation to solve issues existing in geological fields, and well log data interpretation can be ambiguous, and there exist ambiguity during geological interpretation given the absence of core (Rider, 2002; Lai et al., 2023a).

To fill the gaps between well log data and geological application, this review starts with looking back the origin and development histories of well logs. Then the vertical resolution, depth of investigation and applications of various well log suits are summarized. Next the applications of well logs in geological and engineering fields are discussed. Well logs are used in calculating petrophysical parameters and finding the hydrocarbon reservoirs. Lithology, lithofacies as well as depositional microfacies can be recognized and described by conventional well log curve values and shapes as well as image logs. Sequence stratigraphy division can be performed by the logging curve shape and vertical stacking patterns as well as wavelet transformation. Structure including unconformity, fold and fault can be detected by the image logs and dipmeter log derive dip patterns. The *in situ* stress direction and *in situ* stress magnitude can be determined and evaluated using conventional, sonic and image logs. Fracture attitudes (strike, dip direction and dip angle) and status (open, fill or open-fill) are evaluated using image logs. Then the geological and engineering sweet spots in unconventional oil and gas resources are predicted using well logs. Lastly, the research prospects of well logs are discussed, and well logs are applied in other aspects of geosciences, and will solve geological issues more efficiently with the developments of logging tool and artificial intelligence. The ultimate goals of this study are to summarize the application of well logs in the geological fields, and hope the readers can use for future work. This comprehensive review bridges the gaps between well log and geology, and will extend the application of well log data for petrophysicists, and can also provide new ideas to solve problems for geologists.

2. Origin and developments of geophysical well logs

Geophysical well logging was invented in 1927 (Allaud and Martin, 1977; Ellis and Singer, 2007). In 1927, Henri Doll and Schlumberger brothers measured the first resistivity curve at Pechelbronn, announcing the birth of geophysical well logging (Allaud and Martin, 1977; Luthi, 2001; Ellis and Singer, 2007). Well logs have been widely used for geological, geophysical and engineering fields since then (Ellis and Singer, 2007). Well logs, which continuously measure the borehole petrophysical parameters (acoustic, electrical and nuclear), are alternate or supplement to the core and seismic data, and they have the advantages of continuous distribution, low cost and high vertical resolution (Ellis and Singer, 2007; Aghli et al., 2016).

The vertical resolution of seismic data is limited as the ¼ wave length, and is mainly in the range of tens of meters (20–30 m) (Fig. 1). Core data (naked eyes or with magnifying glass) can detect millimeter to centimeter-level variations (Fig. 1). Core analysis data have a wide range of resolution from nanometer to micrometer scales. Resolution of thin section by optical microscope is restricted to 10 μm, however, scanning electron microscope helps detect the nanometer scale pore systems (organic matter pores in shales or micropore associated with clay minerals in tight sandstones) (Fig. 1). In addition, X-ray computed tomography (X-CT or simply known as CT) scanning analysis can provide micrometer to millimeter scale images of three-dimensional pore throat structure (Fig. 1). X-CT is based on the attenuation recording variations of an X-ray beam through rocks, and it provides *in situ* studies of the three-dimensional distribution of pores and fractures in rocks (Yao et al., 2009). The petrophysical well logs, which have vertical resolutions ranging from millimeter scales (the vertical resolution of image logs is 5 mm) to meter scales (the vertical resolution of conventional logs is mainly meter scale), help link core data and seismic data (Fig. 1). In addition, the well logs data include abundant geological information, and they can help extend the formation evaluation and geological interpretation for intervals or wells without core data (Lai et al., 2017).

Well logging has undergone constant and sweeping changes since its birth in 1927 in France (Tiab and Donaldson, 2004). Luthi (2001) summarizes the development history of well logging, and four distinct phases can be divided.

(1) The conceptual phase (1921–1927)

In order to understand the geological characteristics of the subsurface formation, there is in great need to record petrophysical properties using wirelines. On September 5, 1927, the birth of electric well logging is created (Luthi, 2001).

(2) The acceptance phase (1927–1949)

In this stage, there are many commonly used logging tools developed. Gamma ray logging was introduced in the late 1930s, and was directly used for differentiating shaly from clean formations (Ellis and Singer, 2007). In 1942, Schlumberger introduced the first dipmeter tool (Luthi, 2001). The earliest attempt to detect borehole sound wave speed was made by Conrad Schlumberger in 1935 (Bateman, 2020). Then Schlumberger company entered the velocity logging business in 1955 (Ellis and Singer, 2007). Induction logging tool was introduced in 1940s, and it rapidly became widespread and dominated the entire resistivity survey market due to its applicability in oil based drilling muds (Liu, 2017). Conversely, the laterolog type tools are used in saline drilling fluids. The deep-induction measurement (ILd) was developed in 1960 and it is still being run nowadays (Ellis and Singer, 2007). Neutron logging tool was firstly introduced in 1948 with a chemical source of neutrons and a single detector recording "neutron count rate" (neutron logs were not calibrated and thus the logs were scaled to neutron counts), and neutron log was used for porosity calculation and hydrocarbon type (oil or gas) determination (Bateman, 2020).

The initial uses of well logs were finding hydrocarbon-bearing formations (Ellis and Singer, 2007). In 1942, Gus Archie (Shell Company) proposed Archie's equation, which unravels the empirical

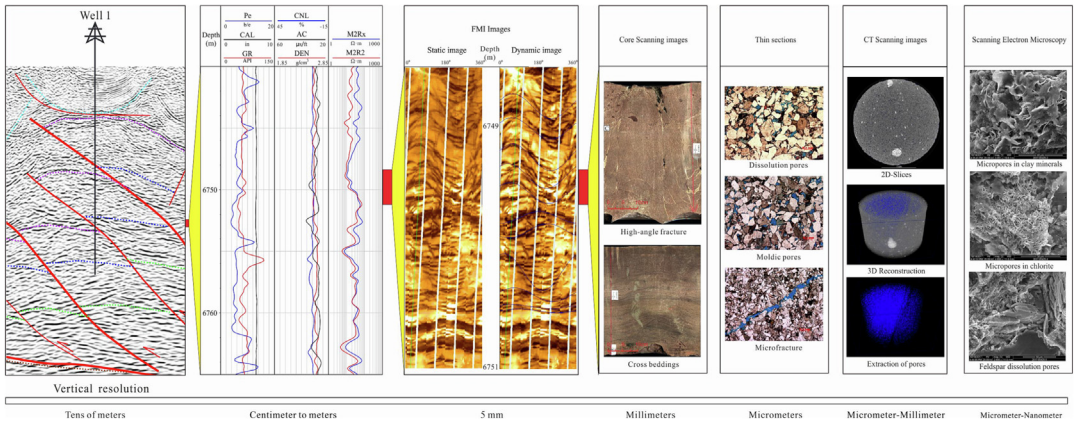

Fig. 1. Correlation between various geological data and well log data of various vertical resolution.

relationships between porosity, resistivity and water saturation (Archie, 1942; Luthi, 2001). The Archie's equation builds the relationships between rock electricity and oil bearing property, and well log interpretation is transformed from qualitative analysis to quantitative determination of fluid saturations (Luthi, 2001; Tiab and Donaldson, 2004). Then fluid saturations can be determined from porosity and deep resistivity logs (Luthi, 2001). In this acceptance stage, the well logs are increasingly used for layer correlation, hydrocarbon-bearing zone identification, well surveying and perforating (Luthi, 2001).

(3) The maturity phase (1949–1985)

In the early 1950, Schlumberger developed several electrical measurements such as the micro resistivity log, and the early version of neutron porosity log was brought onto the market (Luthi, 2001). In addition, Doll proved the feasibility of induction logging, which can be applied in wells drilled with freshwater or oil-based muds (Luthi, 2001). The dual laterolog, which was developed for salty drilling mud systems, was introduced in 1972 and provided two laterolog measurements (shallow and deep) and a near-wellbore resistivity measurement (Bateman, 2020). Laterolog type tools need galvanic contact of the electrodes with a conductive drilling fluid/mud.

The bulk density log (DEN), or photoelectric (Pe) log, measure formation density, were introduced in 1956, and are used to derive total porosity (Liu, 2017). In the 1960s, density logging was put in commercial use (Luthi, 2001). The sidewall neutron porosity (SNP) was introduced in 1962, and then the compensated neutron logging tools (CNL) were introduced in the late 1960s.

The NMR effect was first measured in 1946 and NMR logging was performed since the 1960s, then NMR logging was brought to the market in 1991 (Liu, 2017). NMR logs are widely used for porosity calculation, permeability estimation, and fluid property determination (Liu, 2017). The "borehole televiewer" (BHTV) was developed by Mobil in the late 1960s, and BHTV logging provides borehole images (Luthi, 2001). High-resolution dip meter (HDT) was introduced in 1967 to measure four micro resistivity curves, two caliper curves and three azimuth curves, are used to determine stratigraphic dip (Luthi, 2001). Logging-while-drilling (LWD) (log curves are collected during drilling) was introduced in 1980s (Luthi, 2001).

The advent of porosity and resistivity logs, as well as new petrophysical logging methods, such as BHTV, SHDT as well as NMR logs, have expanded the application of well logs in geological fields. Numerous technological breakthroughs redefine well logging as an important aid for reservoir development and management (Luthi, 2001). The initial use of logs, i.e., finding hydrocarbon-bearing zones, was slowly supplanted by "formation evaluation", or petrophysics (Luthi, 2001).

(4) The reinvention phase (1985–2000)

All well log recordings were made using analog systems up until the 1970s, and the logs were made on paper with an ink pen or with a light beam on photographic film (Bateman, 2020). Well log data become digital since the 1980s. Two breakthroughs had been made in the 1990s, and one of them is the introduction of multi-array induction tools–devices with multiple simple arrays (Ellis and Singer, 2007). Another is the introduction of imaging logging tool by Schlumberger (Formation Micro-Imager tool (FMI)) in 1991. FMI is the next generation of the FMS (Formation MicroScanner) tool (developed in the 1980s), and the birth of FMI indicates that the well logging technology came into a new era (Lai et al., 2018). Also in the 1990s, NMR logging became available as a robust wireline measurement (Luthi, 2001).

The multi-array induction tools have improved the vertical resolution of logs from 1 m (dual lateral logs have 1 m vertical resolution) to 1–2 feet (0.3048 m–0.6096 m), and the ability to identifying thin layers has been improved. The FMI imaging logging tool, of which contains 8 pads and 192 electrodes, can collect 192 microresistivity curves. Then the microresistivity curves can be processed into high-resolution images (up to 5 mm) of the wellbore wall (Goodall et al., 1998; Khoshbakht et al., 2009; Rajabi et al., 2010; Moreau and Joubert, 2016; Lai et al., 2018, 2022).

(5) The advanced well logging phase (since 2000)

In the 21st century, advanced borehole geophysical logging techniques were developed to provide fine-scale data on petrophysical parameters such as mineralogy, reservoir quality, fluid property. The geological objects (vugs) that are 5 mm or larger can be recognized from the image logs. Fine-scale features as small as 50 μm are visible on the FMI logs (Maliva et al., 2009).

NMR logs provide a measure of porosity and pore size distribution, and moveable water distribution (Coates et al., 1999; Wang et al., 2020).

The geochemical elemental capture spectroscopy (ECS) log provides weight content of a total of 26 elements, and the abundance of carbonate, total clay, QFM (quartz, feldspar, and mica), siderite, pyrite, anhydrite, salt and coal can be obtained (Schlumberger, 2006; Maliva et al., 2009).

Array acoustic logging tools have multiple receivers (Xiang et al., 2015), and they record full wave-forms, and can be used to

extract the slownesses of compressional wave, shear-wave, Stoneley wave and pseudo-Rayleigh wave (Collett et al., 2011; Zaree et al., 2016; Lai et al., 2017).

The history of well logging depicts how the logging technique has developed from its humble beginnings to a wide range of market services with the increasing demands for geological interpretation (Luthi, 2001). Well logs have gradually been applied in structural mapping, reservoir description, fracture detection and sedimentological characterization (Ellis and Singer, 2007).

3. Vertical resolutions, depth of investigation and applications of various well log data

3.1. Conventional well logs

The nine conventional logs, which include three lithology logs (caliper (CAL), natural gamma ray (GR) and spontaneous potential (SP)), three porosity logs (bulk density (DEN, RHOB), neutron porosity (CNL, NPHI), and sonic interval transit time (AC, DT)), and three resistivity logs (micro resistivity, shallow resistivity and deep resistivity logs), are widely used for formation evaluation and geological interpretation (Nabawy et al., 2010).

The CAL log measures the diameter of borehole, and it is widely used for recognition of lithology, determination of borehole shape and size, fracture and borehole breakout recognition.

The natural gamma ray (GR) log detects the intensity of radioactivity including K, Th and U elements, and has vertical resolution of about 1 m with a depth of investigation of 15 cm (Fig. 2). About 90% of the signal of gamma rays comes from formation with 15 cm thick depth of investigation (Ellis and Singer, 2007; Liu, 2017). GR logs are used for recognition of radioactive minerals and lithology, calculating clay content, dividing of reservoir (clay-free) zones and sedimentary characterization.

The spontaneous potential (SP) log measures the diffusion and absorption electromotive force at the sandstone-mudstone contacts, and has vertical resolution of about 2.0 m (Fig. 2). SP log is firstly treated as a porosity indicator, and now is used for identification of permeable zones, indicating the amount of clay in a reservoir, determining the water flooding zone and calculating the formation water resistivity or even indicating depositional environment (Luthi, 2001; Ellis and Singer, 2007; Bateman, 2020).

Sonic log, or acoustic log (AC, DT), measures the speed of sound waves, has a very low depth of investigation (1–3 cm) and a vertical resolution of 0.6 m (Fig. 2). Sonic logs are used for determining porosity or the fluid content, recognizing lithology, fracture detection, gas bearing layer recognition, abnormal pressure evaluation and calibrating with seismic data (Ellis and Singer, 2007; Liu, 2017; Bateman, 2020). Sonic logs can be further used for source rock characterization combined with resistivity logs (Passey et al., 1990; Bateman, 2020).

Neutron porosity log (CNL, CNC, NPHI), which measures the formation hydrogen index, has a vertical resolution of 1 m and depth of investigation of 25 cm, and is used in the fields of calculating porosity, lithology recognition, gas bearing layer determination combined with density log (Liu, 2017).

Density log (DEN, ZDEN, RHOB) measures the bulk density of formation according to the Compton effect, and has a very shallow depth of investigation of about 5–10 cm (90% of the signal). The vertical resolution is also about 1.0 m scale, and density logs (in some cases combined with litho-density Pe log) can be used for calculating porosity, and recognizing lithology or certain minerals.

During well drilling, the drilling muds will invade the formation, and a profile with resistivity fluctuation will be encountered (Ellis and Singer, 2007; Liu, 2017). Firstly, a thin layer of mudcake will be formed around the borehole, and recognized by resistivity R_{mc} (Ellis and Singer, 2007). Beyond the mudcake is the flushed zone, whose resistivity is determined by resistivity of the mud filtrate, and is denoted by R_{xo} (Ellis and Singer, 2007). Then the uninvaded or virgin zone with true formation resistivity R_t (resistivity is not influenced by resistivity of the mud filtrate) lies beyond the

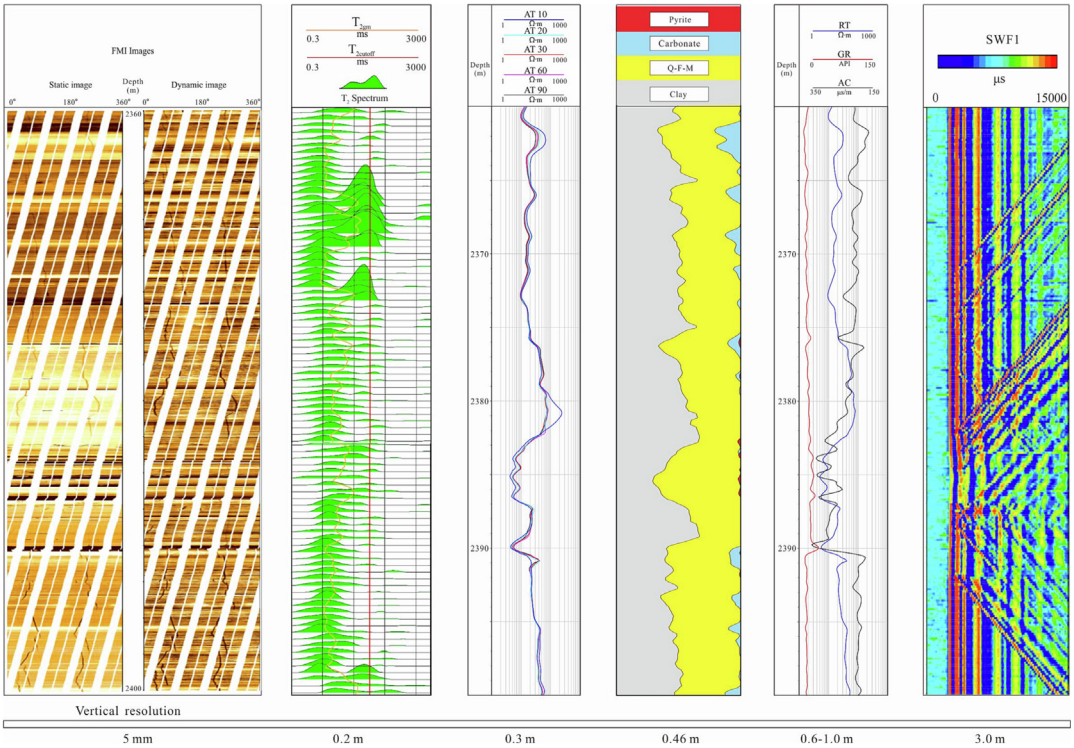

Fig. 2. Geophysical well log data of various vertical resolution.

invaded zone (Ellis and Singer, 2007). However, there is a transition zone separating the flushed zone from the virgin zone (Ellis and Singer, 2007).

Three resistivity logs are called according to their depth of investigation. The resistivity logs can be divided into lateral log (LLS, LLD) (used in saline drilling muds), induction log (ILM, ILD) (used in nonconductive oil-base muds) and micro log (MSFL). As is known, the micro resistivity log, which has a depth of investigation of 2.5–10.0 cm, measures the mudcake resistivity (R_{mc}). Conversely, the shallow lateral or shallow induction logs, which have depth of investigation of 0.3–1.0 m, detect the resistivity of flushed zone (R_{xo}). The deep lateral or shallow induction logs have depth of investigation of >1.0 m, and they can measure the resistivity of uninvaded zone, and are used for true formation resistivity (R_t). Resistivity logs are used for fluid property determination, source rock characterization, lithology identification (Ellis and Singer, 2007).

3.2. Advanced well logs

Conventional resistivity logs have a vertical resolution of 1 m (Fig. 2). However, the high definition induction log (HDIL) (M2Rx, M2R9, M2R6, M2R3, M2R2, M2R1 or AT10-AT90) can reach a vertical resolution of 1–2 ft (about 0.3 m – 0.6 m) (Fig. 2). Therefore, the high definition induction logs are widely used for the thin layer identification due to their high vertical resolution.

The acoustic logging tool only measures sonic transit time (Δt), while the array acoustic logging tools (Schlumberger's Dipole Sonic Imager (DSI), Baker Hughes's XMAC and Halliburton's Wave Sonic tool) have multiple receivers, and they can detect the full waveforms (amplitudes) including the compressional wave velocity, shear-wave velocity, V_p/V_s ratio, Stoneley wave and pseudo- Rayleigh waves (velocity and amplitude) (Collett et al., 2011; Xiang et al., 2015; Lai et al., 2017; Liu et al., 2018). The array acoustic logs have vertical resolution of about 3.0 m (Fig. 2), and they can be used for *in situ* stress field evaluation by shear wave birefringence, fracture and permeable zone identification (Zaree et al., 2016; Liu et al., 2018; Zhao et al., 2018; Lai et al., 2022).

Elemental Capture Spectroscopy (ECS) uses an americium beryllium (AmBe) neutron source and bismuth germanate (BGO) detector to detect released gamma rays (Maliva et al., 2009). The relative elemental spectral yields are then converted to dry-weight elemental concentrations. The ECS logs can then provide information on the mineralogy including total clay, carbonates, Q-F-M (quartz, feldspar, and mica), siderite, pyrite, anhydrite, salt, and coal (Maliva et al., 2009). The ECS logs have high vertical resolution of 0.46 m (1.5 ft) (Fig. 2), and ECS well logs can be used for lithology recognition, mineral rock skeleton calculation, sedimentary environment research, and clay minerals identification.

Nuclear magnetic resonance (NMR) is sensitive to the quantity and distribution of fluids in the formation (Ellis and Singer, 2007). NMR logging, which have vertical resolution of 0.2 m (Fig. 2), allow quantifying or estimating the properties including total porosity, bound and free pore fluids, presence and type of hydrocarbons, intrinsic permeability and pore size distribution (Luthi, 2001; Tan et al., 2014; Liu, 2017; Olatinsu et al., 2017; Wang et al., 2020). Additionally, the two-dimensional NMR data consist of transversal relaxation time (T_2) spectrum and diffusion coefficient (D) (Tan et al., 2014; Bauer et al., 2015), and they can be used for fluid property discrimination and estimate the movable oil content (Wang et al., 2020).

The first dipmeter log (SHDT) tool or the "anisotropy tool" has four or six pads, and the 4 or 6 pads that will measure 4 or 6 micro resistivity curves, and provide 2 or 3 caliper logs, i.e., C13, C24 as well as a azimuth curve (Luthi, 2001). The dipmeter log aids in determining large-scale tectonic structures as well as smaller-scale sedimentary structures in the vicinity of wellbore (Luthi, 2001). The dipmeter log can be used for fracture detection, borehole collapse recognition, and picking out of cross bedding.

The development of dipmeter logging with a larger number of electrodes has laid the foundation for electrical imaging logging tool (Luthi, 2001). The earlier used Formation Micro Scanner (FMS) tool consists of four orthogonal pads, and each pad contains 16 electrodes (Luthi, 2001). The borehole coverage is only 30% in an 8.5-inch borehole (Serra, 1989; Khoshbakht et al., 2012). Fullbore Formation MicroImager (FMI) imaging tool improves the borehole coverage to about 80% since there are effectively eight pads of 24 buttons, or a total of 192 electrodes (Luthi, 2001; Schlumberger, 2004; Folkestad et al., 2012; Wilson et al., 2013; Lai et al., 2020). The electrical imaging tools have very shallow depth of investigation (a few inches) compared to other logging tools (Liu, 2017), however, the vertical resolution of image logs can reach as high as 5 mm (Fig. 2) (Lai et al., 2021).

4. Applications of well logs in solving geological issues

4.1. Structural geology

4.1.1. Attitude of strata

Besides conventional well logs, dipmeter logs and image logs play more important roles in structure interpretation (Schlumberger, 1981; Luthi, 2001; Lai et al., 2018). The dipmeter tool is the first structure revealing tools. The dipmeter logging tool has four or six pads, and will provide 4 or 6 micro resistivity curves, and provide 2 or 3 caliper logs, i.e., C13, C24 (C14, C25, C36) and an azimuth curve. The 4 or 6 micro resistivity curves can be used for cross-correlation to obtain the stratigraphy dip direction (Luthi, 2001).

There are three wells (YS 4, YN 4, YN 2) drilled in the Kuqa depression (Fig. 3), which is a foreland basin (Lai et al., 2019a). Many complex structures including faults, folds as well as fault related fold are formed in the complex tectonic histories. The pole chart picked out from image logs reveals that the Well YS 4 and Well YN 4 are characterized by steep dip angles and varied dip direction, and the seismic interpretation results confirm the presences of faults (reserve faulting) and anticlines, which result in the high dip angles and varied dip direction in the pole charts (Fig. 3). Conversely, the Well YN 2 was drilled in a uniform structure as interpreted from seismic profiles, and the dip direction and angle are uniform in the vertical direction (Fig. 3). Therefore, the image log derived pole charts will provide insights into the attitudes of stratum, and can give accurate interpretation results even in complex geological settings.

4.1.2. Detection of fault, fold and unconformity

Conventional well logs can evidently recognize the unconformity surfaces due to the rapid changes of logging readings and well log curve shapes. Unconformable surfaces are often evident in conventional well logs because of significant changes in well log values and curve shapes (Fig. 4). The large-scale unconformity between Cambrian Qiulitage Formation ($\epsilon_3 q$) and Cretaceous Kapushaliang Group ($K_1 kp$) in the Tarim Basin are easily to be picked out from the well logs, as can be seen from Fig. 4, the GR curve and the three porosity logs change rapidly at the unconformity surfaces. The overlying Cretaceous Kapushaliang Group ($K_1 kp$) is deposited in fan-braided deltaic facies environments, and the lithologies are dominantly sandstones or conglomerates (Fig. 4). In contrast, the underlying Cambrian Qiulitage Formation ($\epsilon_3 q$) is dolostones deposited in large shallow carbonate platform (Fig. 4) (Du et al., 2018). Consequently, the unconformity which implies a long term depositional hiatus, will result in rapid

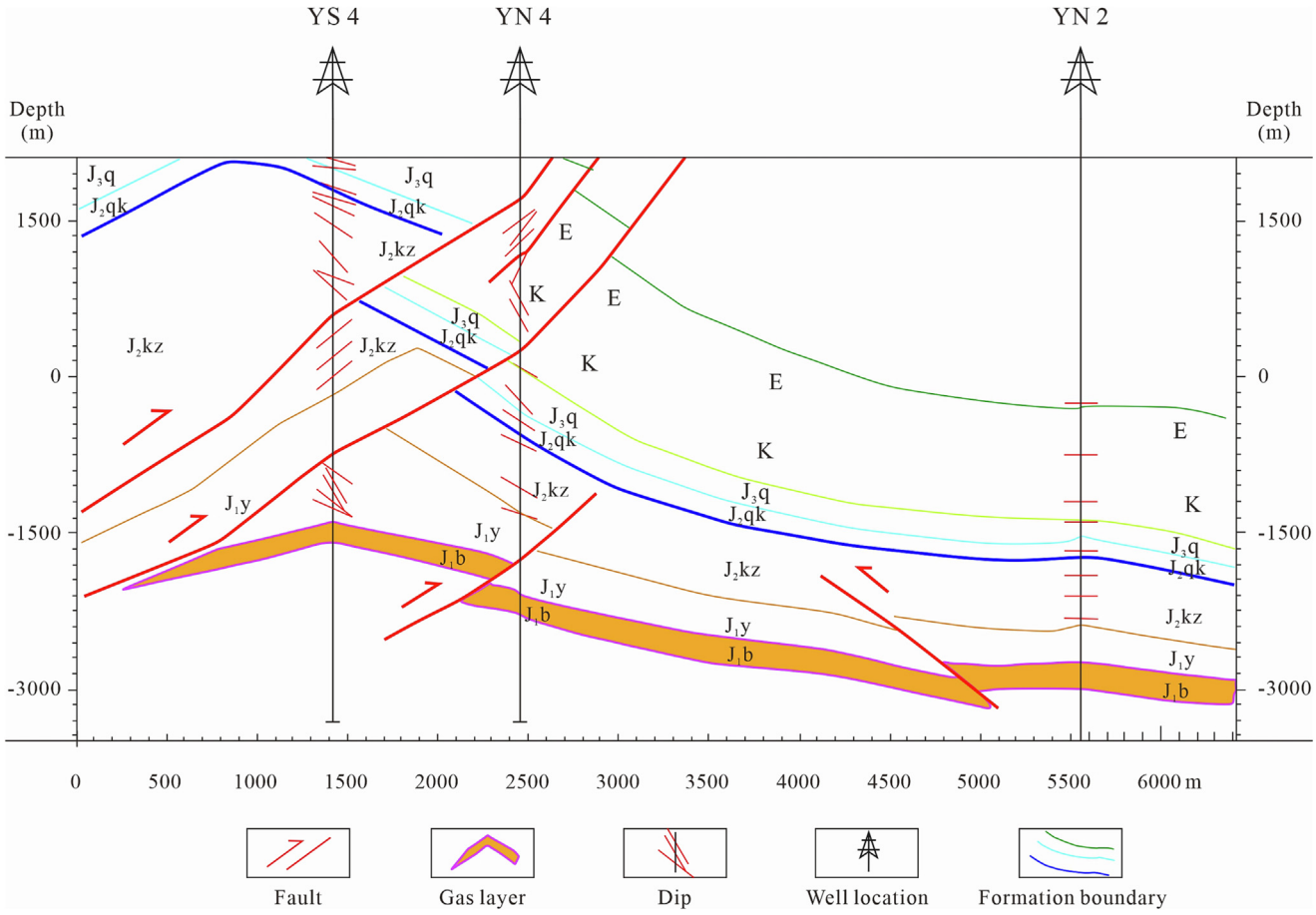

Fig. 3. Determination of attitude of strata using borehole image logs and their calibration with seismic profile in Kuqa depression, Tarim Basin.

variations in mineral composition and lithofacies association, and therefore will contribute to the rapid changes of log values and well log curve shapes (Fig. 4).

The cross-correlation methods are mathematical procedures with the aim to produce dips at regular intervals, and four types of dip patterns can be divided according to the sequences where the dip changes with depth in a typical manner. Among them, the red pattern refers to an upward decrease in dip angle (constant dip direction), conversely, the blue pattern refers to an upward increase in dip angle (constant dip direction) (Luthi, 2001). The constant dip angles and dip direction is the green pattern, and the scattered dips (no ruled dip angles and direction) is called white or yellow pattern (Luthi, 2001). Green pattern often indicates structural dip, while the red and blue patterns are indicative of sedimentary structures (bedding) and geological objects (Luthi, 2001). The white pattern generally contains no geometric information (Luthi, 2001). The dip patterns are proven to be particularly useful for large-scale geological structures (fault, fold), and for sedimentary structure interpretation (Schlumberger, 1989; Luthi, 2001; Schlumberger, 2013).

Image logs, which are the improvements of dipmeter logs, have great potentials for structure interpretation. Image logs provide high resolution images for borehole walls, and can easily pick out fracture (induced and natural), unconformity and fault. For instance, an unconformity is easily to be picked out from the image logs since there are rapid color pattern changes at the unconformity surfaces (Fig. 4). Additionally, image logs can also provide the dip patterns (manually of machine automatically picked) (Zhao et al., 2019) (Fig. 5). The dip patterns will provide important information on the dip angles and dip direction, and the presence of fault or fold will cause a rapid change in dip angle or direction, and therefore the fold or fault can be recognized (Fig. 5). Actually, possible faults and folds exist when red and blue dip patterns change alternatively. Therefore, the graphical method can be used for discerning potential faults/folds from color coded dig information.

Image logs which provide high resolution images and additional borehole dip patterns, are also widely used for structure analysis (Lai et al., 2018, 2022). Dips are manually picked out from the images, and the dip direction is rapidly changed at the depth intervals of 2769–2771 m (Fig. 6). In addition, the rose diagram as well as the dip patterns show that the dip direction is significantly varied, implying the presences of fault (Fig. 6). Dip pattern analysis combined with image log observation from well logs allows identification of structures around the borehole such as fault, fold and unconformity.

4.1.3. In situ stress status and direction

In situ stresses are the present-day natural stresses in the earth's crust, and are closely associated with gravitational (overburden rocks) and tectonic stresses (Bell, 1996; Ameen and Hailwood, 2008; Ju et al., 2017). The *in situ* stress status include five components: (1) vertical stress (S_v), (2) pore pressure (P_p), (3) maximum principal horizontal stress (SH_{max}), (4) minimum principal horizontal stress (Sh_{min}), and (5) the horizontal stress orientation (Zoback et al., 2003; Dixit et al., 2017; Hassani et al., 2017; Ju and Wang, 2018). The S_v is related to the gravity of overburden rocks, while the horizontal SH_{max} and Sh_{min} are perpendicular with

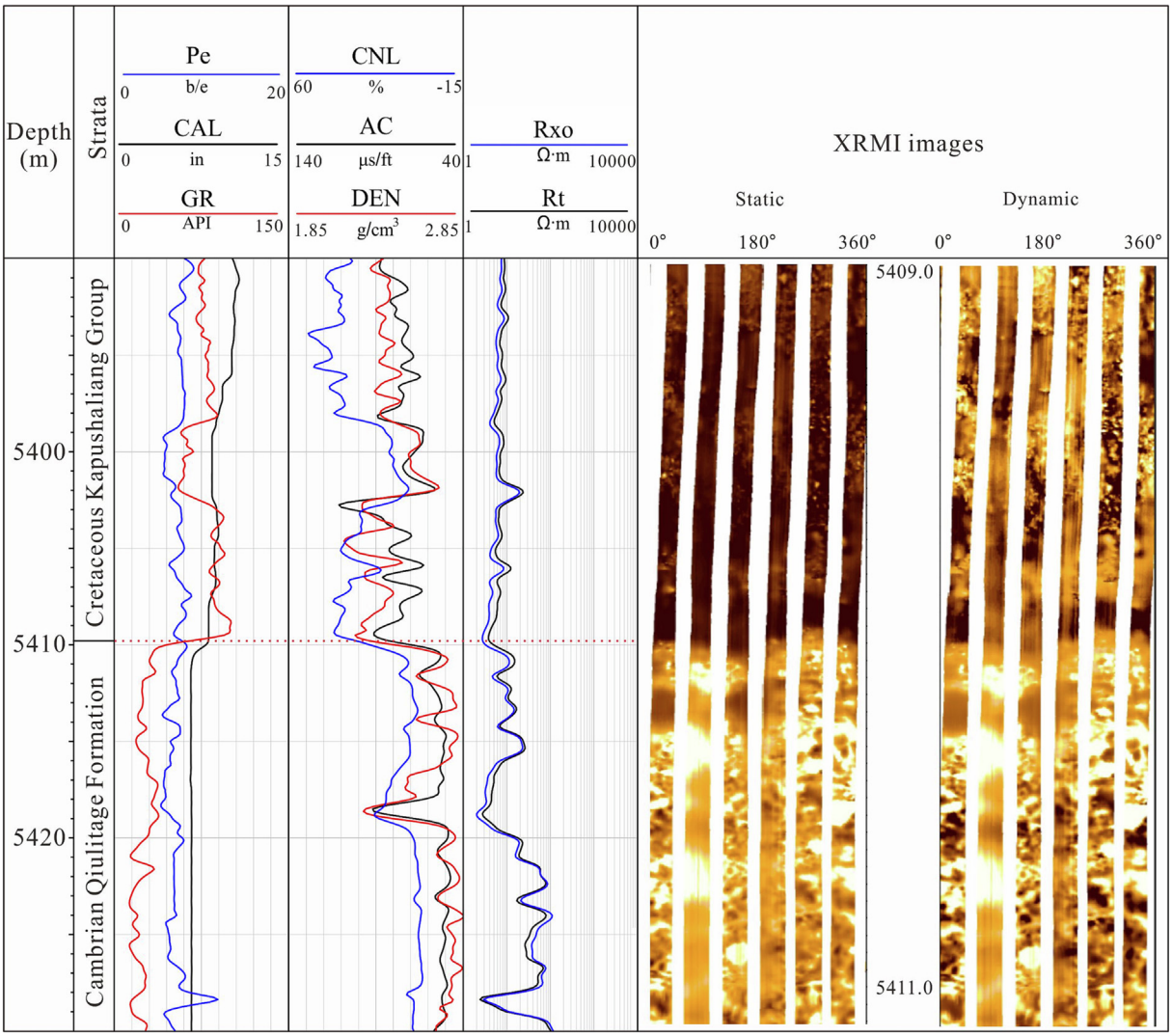

Fig. 4. Well logs showing the unconformity between Cambrian Qiulitage Formation and Cretaceous Kapushaliang Group in Tarim Basin.

each other, and are caused by the overburden rocks and horizontal tectonic stress (Engelder, 1993; Hassani et al., 2017). The S_v, SH_{max} and Sh_{min} are called three orthogonal principal stresses (Engelder, 1993; Tingay et al., 2009; Lai et al., 2019a). Well log data can be used to determine the *in situ* stress direction and calculate stress magnitudes. The sources of stress exceeding rock strength are related to the pressure of the column of fluids and drilling mud within the borehole, as well as tectonic activity.

4.1.3.1. Orientation of horizontal stress. The orientations of *in situ* stress (SH_{max} and Sh_{min}) can be interpreted from drilling-induced fractures and borehole breakouts (Zoback et al., 1985; Prioul et al., 2007; Lai et al., 2018; Stadtmuller et al., 2018). The borehole breakouts indicate the orientations of Sh_{min} (Zoback et al., 2003; Massiot et al., 2015). Borehole breakouts are easily recognized as wellbore enlargements appearing as broad, parallel, dark bands separated by 180° on image logs (Rajabi et al., 2010). Borehole breakouts occur when the stresses exceed the rock strengths around the borehole wall (Lai et al., 2017).

The drilling induced fractures, which indicate the orientations of SH_{max}, are divided into two types, and they include drilling induced tensile and shear fracture (Brudy and Zoback, 1999; Ameen and Hailwood, 2008). The drilling induced shear fracture refers to the en-echelon fractures around the wellbore, and they are 180° offset at the borehole surface with en-echelon distribution characteristics (Brudy and Zoback, 1999). The drilling induced tensile fractures are recognized as narrow, sharply defined features on the image logs (Brudy and Zoback, 1999). In addition, the drilling induced tensile fracture is recognized as two vertical fracture traces on images oriented at 180° apart (Ameen et al., 2012; Lai et al., 2017). The orientation of induced fractures indicates a maximum horizontal-stress orientation of 0–10°. There are no doubts that the induced fractures appear as 90° in orientation from borehole breakouts.

The shear wave will split into fast and slow waves in anisotropic rocks (Stadtmuller et al., 2018). Therefore, fast S-wave azimuth direction from array acoustic logging tools can also be used for SH_{max} direction determination (Fig. 7). The variations of shear wave velocities and further varied polarization orientations of shear waves will be encountered in anisotropic formation (Liu et al., 2018), and the shear wave birefringence due to formation anisotropy will result in the formation of fast shear and slow shear waves. The fast S-wave azimuth is parallel to SH_{max}, and the SH_{max} direction can be determined as NW–SE from fast shear wave azimuth (Fig. 7).

4.1.3.2. In situ stress magnitude. In situ stress magnitude plays vital roles in geomechanical modeling and hydraulic fracturing

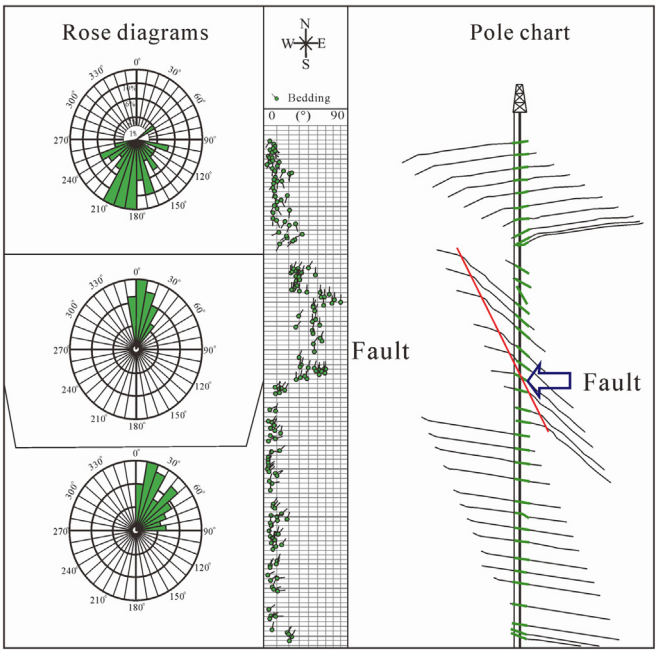

Fig. 5. Borehole dip analysis and fault interpreted from the dip patterns (Zhao et al., 2019).

treatment (Zoback and Townend, 2001; Maleki et al., 2014; Najibi et al., 2017; Iqbal et al., 2018). Design of hydraulic fracture without *in situ* stress analysis will give rise to error in fracture length (Iqbal et al., 2018). Besides acoustic emission (AE) tests, geophysical wireline logs can be used to calculate in-situ stress magnitudes (Fig. 8) (Iqbal et al., 2018).

The magnitude of S_v equals to the weight of the overburden rocks at a certain depth, and is calculated by integration of bulk density (Eq. (1)) (Maleki et al., 2014; Verweij et al., 2016; Lai et al., 2019a).

$$S_v = \int_0^Z \rho g dz \tag{1}$$

where Z is the burial depth (m), ρ is the bulk density (kg/m^3), g is gravitational acceleration (m/s^2) (Maleki et al., 2014; Verweij et al., 2016).

Pore pressure (P_p) can be calculated by Eaton's method (Eq. (2)) (Eaton, 1969; Grollimund et al., 2001; Tingay et al., 2009; Zhang, 2011; Ju et al., 2017).

$$P_p = P_0 - (P_0 - P_w)(\Delta t_n/\Delta t)^c \tag{2}$$

Where P_w is the hydrostatic pressure, and is equal to 9.8 MPa/km, Δt_n is sonic interval transit time at normal pressure, Δt is the sonic transit time from logs, and c is compaction (Zhang, 2011; Rajabi et al., 2016).

The Sh_{min} and SH_{max} magnitude can be calculated based on S_v, P_p, Poisson's ratio (v), Young's modulus (E) (Fig. 8) (Eq. (3); Eq. (4)) (Eaton, 1969; Zoback et al., 2003; Maleki et al., 2014; Iqbal et al., 2018).

$$SH_{max} = \frac{v}{1-v}(S_v - \alpha P_p) + \alpha P_p + \frac{E\varepsilon}{1-v^2} \tag{3}$$

$$Sh_{min} = \frac{v}{1-v}(S_v - \alpha P_p) + \alpha P_p + \frac{Ev\varepsilon}{1-v^2} \tag{4}$$

where S_v is the vertical stress, P_p is the pore pressure, Sh_{min} and SH_{max} are minimum and maximum horizontal stress, respectively. α is the effective stress coefficient, "Epsilon" ε=strain factor (Zoback et al., 2003; Iqbal et al., 2018). Knowledge of the geomechanical characteristics (Poisson's ratio υ, Young's modulus E, Biot's coefficient α) is necessary for calculating horizontal stresses (Stadtmuller et al., 2018). In Addition, the information about the amount of strain ε also can be obtained from core test (Stadtmuller et al., 2018).

The state of *in situ* stress controls formation of faults and most of the fractures (Khair et al., 2015). The stress regimes are divided into normal ($S_v > SH_{max} > Sh_{min}$), thrust ($SH_{max} > Sh_{min} > S_v$), and strike-slip ($SH_{max} > S_v > Sh_{min}$) according to the values of the three stress components (Zoback et al., 2003; Verweij et al., 2016; Stadtmuller et al., 2018). The stress regime is typically strike-slip in Fig. 8.

In normal stress regimes, S_v is the maximum principal stress, and fractures and normal faults form parallel to SH_{max} with high dip angle (Khair et al., 2015). The S_v is the minimum principle stress in reverse stress regime, and fractures (low angle) and reverse faults form parallel to SH_{max} (Khair et al., 2015). The S_v is the intermediate principal stress in a strike-slip stress regime, and vertical fractures and strike-slip faults form at 30° intersection angles with SH_{max} (Khair et al., 2015).

The difference between SH_{max} and Sh_{min} ($\Delta\sigma$) has great impacts on directional drilling and hydraulic fracturing (Stadtmuller et al., 2018). Additionally, the fractured zones are mainly related to the layers with low $\Delta\sigma$ value (Fig. 8). The horizontal stress difference ($\Delta\sigma$) control reservoir quality and pore structure, and high quality reservoirs are mainly associated with low $\Delta\sigma$ values (Fig. 9) (Lai et al., 2019a). Porosity has an evidently negative correlation relationship with $\Delta\sigma$, and when the $\Delta\sigma$ is less than 55 MPa the porosity is higher than 9.0% (Fig. 9).

4.1.4. Fracture detection and characterization

Subsurface fractures can significantly improve permeability and hydrocarbon productivity (Ameen and Hailwood, 2008; Laubach et al., 2019; Lai et al., 2023b). Hydrocarbon reservoirs require the presence of fractures around the wellbore to allow the flow of oil and gas to the wellbore (Laubach, 2003; Ameen et al., 2012; Khoshbakht et al., 2012). Therefore, the comprehensive detection and characterization of fractures using a combination of core, well log and seismic data are of great importance. However, seismic data can only recognize large-scale fractured zones due to their low vertical resolution, additionally core data are very limited due to their high cost (Khoshbakht et al., 2012; Aghli et al., 2016; Lai et al., 2017). Consequently, petrophysical well logs, which have the advantages of low cost, high vertical resolution and vertical continuity, are important tools for the detection and characterization of subsurface fractures (Tokhmchi et al., 2010; Aghli et al., 2016; Lai et al., 2017).

4.1.4.1. Qualitative recognition of subsurface fractures. In water based drilling muds, the resistivity logs will be significantly reduced in front of fractures (Fig. 10). Rapid decrease of resistivity logs will be encountered in the heavily fractured zone (Fig. 10) (Shazly and Tarabees, 2013). The presences of fractures will cause minor negative deviations in fractured zone due to the low density of filled drilling muds (Fig. 10) (Zazoun, 2013). Sonic transit time (AC) is sensitive to the fracture appearances, and there is evident increase in sonic transit time in front of fractures (Zazoun, 2013; Aghli et al., 2016) (Fig. 10).

Natural fractures can be interpreted from the image logs by picking out sinusoidal waves because inclined planar fractures appear sinusoidal when borehole wall images are unwrapped axially (Khair et al., 2015). In case there are natural fractures crosscutting the borehole wall, the corresponding resistivity will be low since fracture surfaces are filled with conductive drilling muds (Fig. 10) (Serra, 1989; Ameen et al., 2012; Nie et al., 2013). Natural

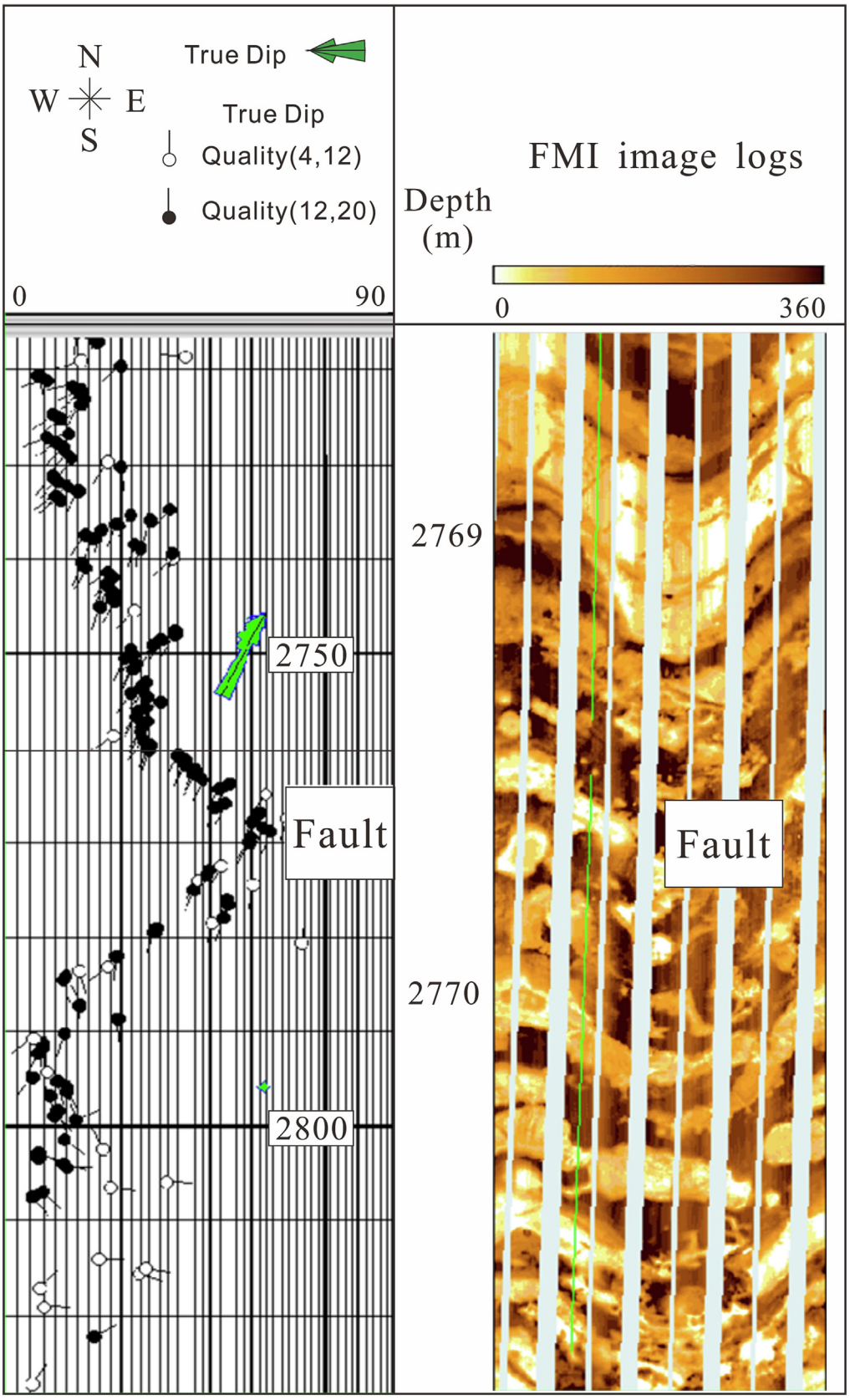

Fig. 6. Fault interpreted from the dip patterns and image logs.

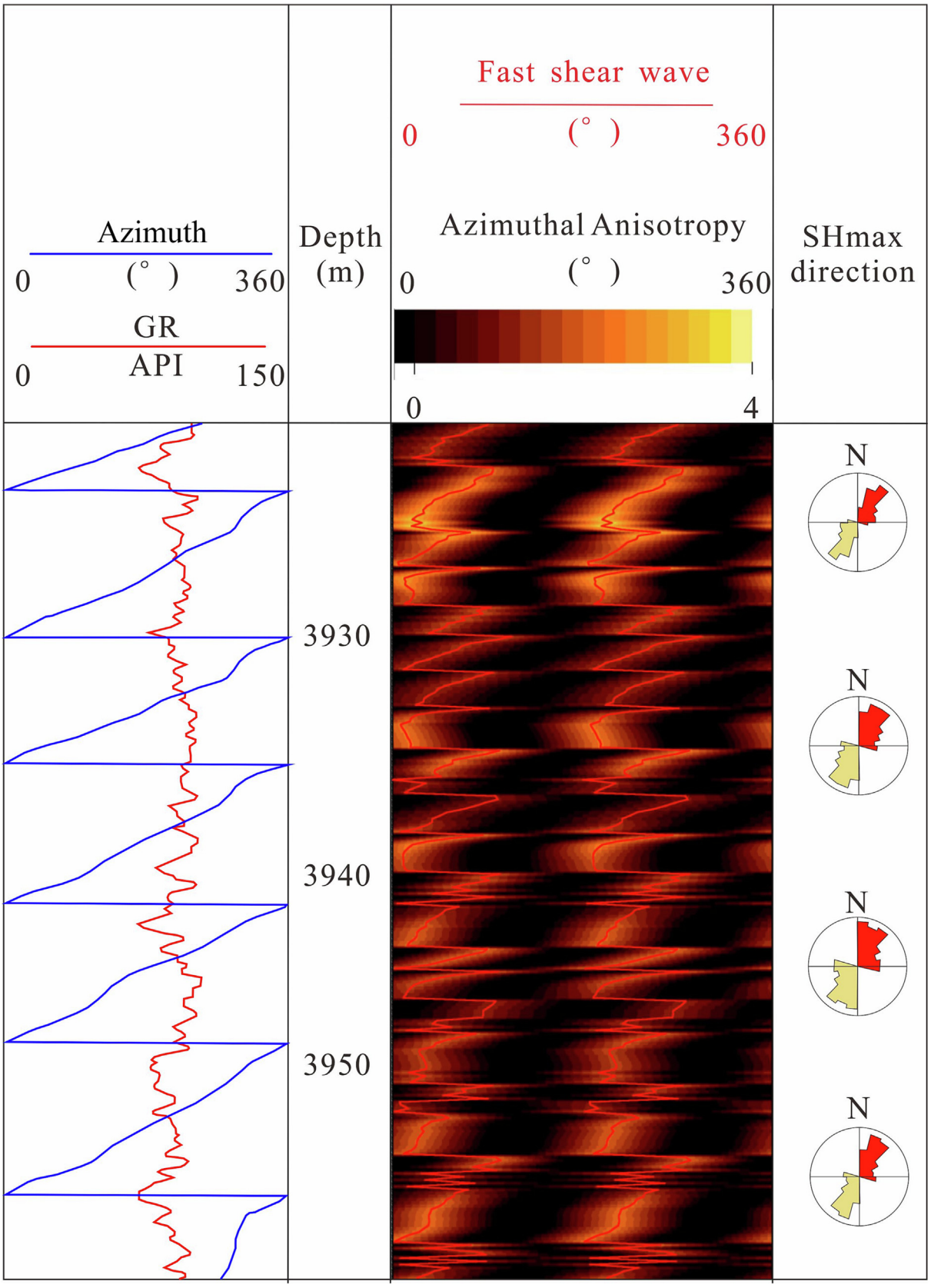

Fig. 7. Comprehensive map of XMAC full-waveform sonic fast shear wave orientation in Well Ji 19.

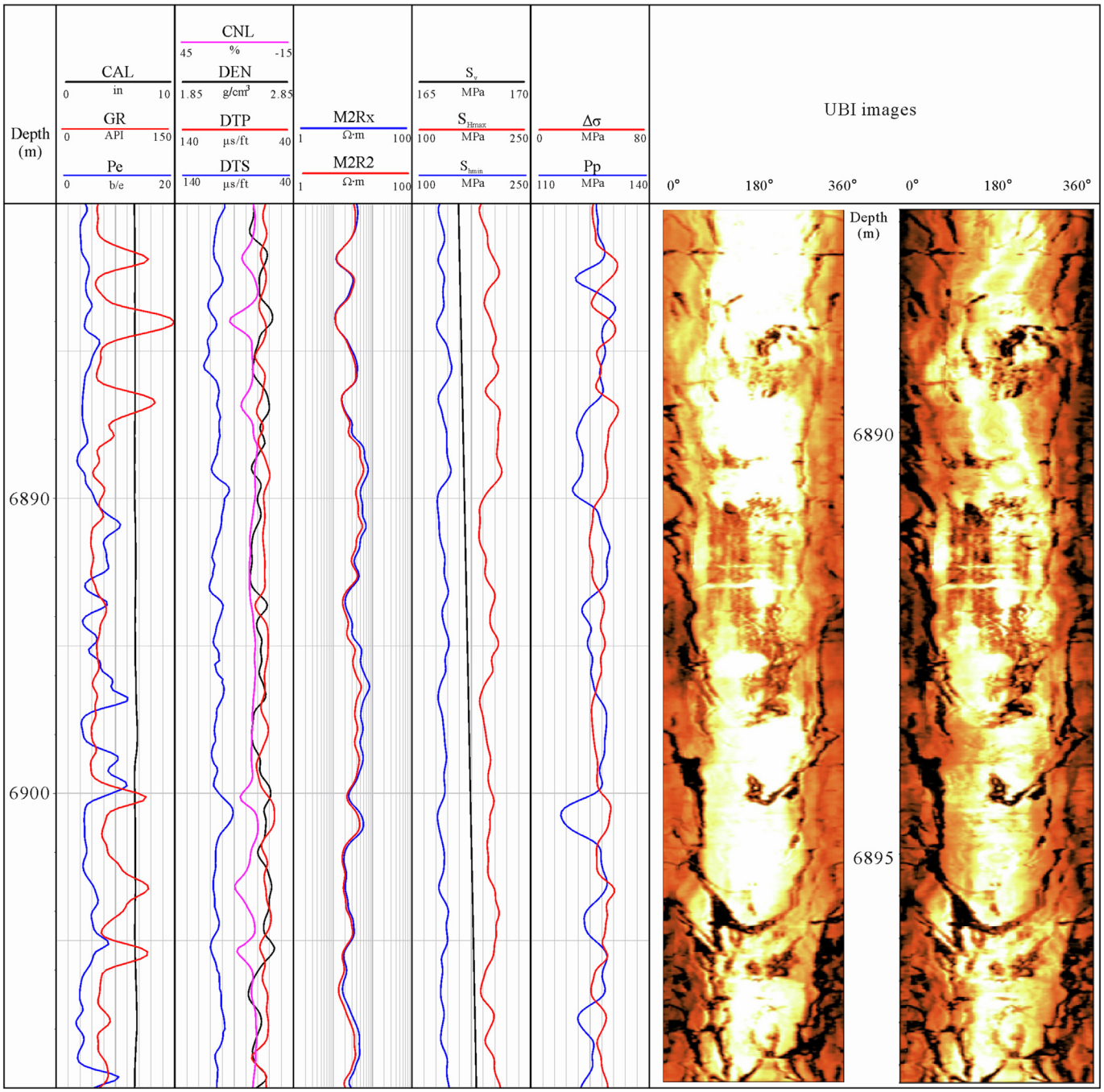

Fig. 8. Determination of the *in situ* stress magnitude (S_v, SH_{max}, Sh_{min}, and P_p) via well logs (Keshen 8004).

open fractures are considered to be filled with drilling mud, giving them a dark, electrically conductive appearance on image logs (Khair et al., 2015). However, there are also resistive fractures, which are closed and/or cemented, and will result in the light, electrically resistive appearance on image logs (Fig. 10) (Khair et al., 2015).

Natural fractures can be distinguished from drilling induced fractures and borehole breakouts on image logs by their continuous nature (continuous sinusoids), while induced fractures and borehole breakout are vertical bands or traces 180° apart (Khair et al., 2015). In addition, drilling induced fractures and borehole breakouts are always open (not filled), while natural fractures can be resistive (filled by resistive carbonate cements) or open status (Khair et al., 2015).

However, there are many wells drilling with oil based muds with the aim of providing better protect hydrocarbon reservoirs and avoid borehole collapse (Gozalpour et al., 2007). The nonconductive mudcakes result in difficult in fracture interpretation using electrical image logs (Movahed et al., 2014). The fractures are replaced by bright sinusoidal waves if the drilling muds are oil based. However, the sonic logs are evidently not affected by the types of drilling muds, and even in oil based drilling muds, the sonic image logs can pick out the fractures as dark sinusoidal waves (Fig. 11) (Khoshbakht et al., 2009; Egbue et al., 2014; Lai et al., 2017). Acoustic logs like AC only provide a single value for each depth, while ultrasonic image logs provide a colorful image.

In addition, the array acoustic logging tools can provide images full wave-forms (Zaree et al., 2016), and are also good indicators for

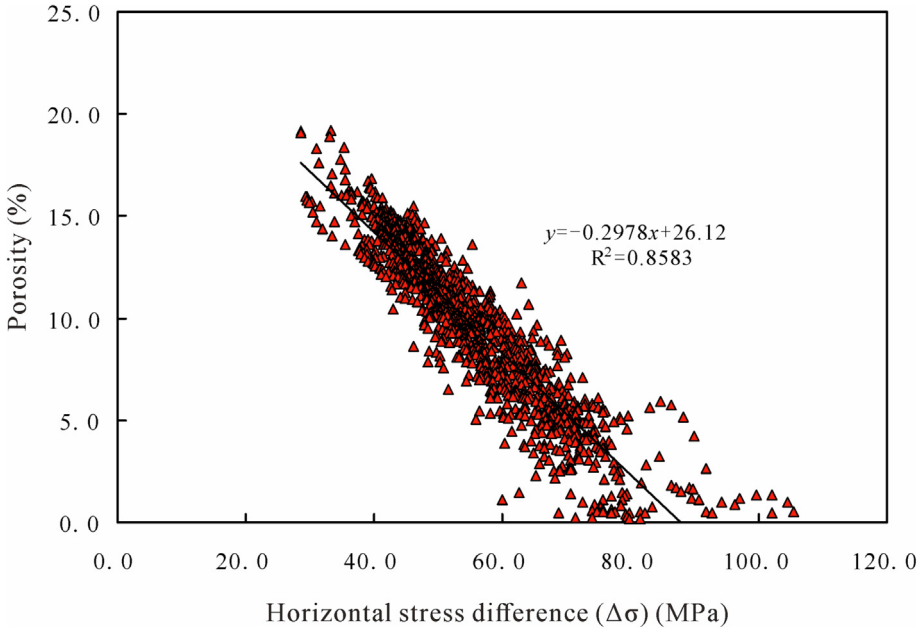

Fig. 9. Crossplot of porosity versus horizontal stress difference (Δσ) of Cretaceous Bashijiqike Formation in Kuqa depression, Tarim Basin of China.

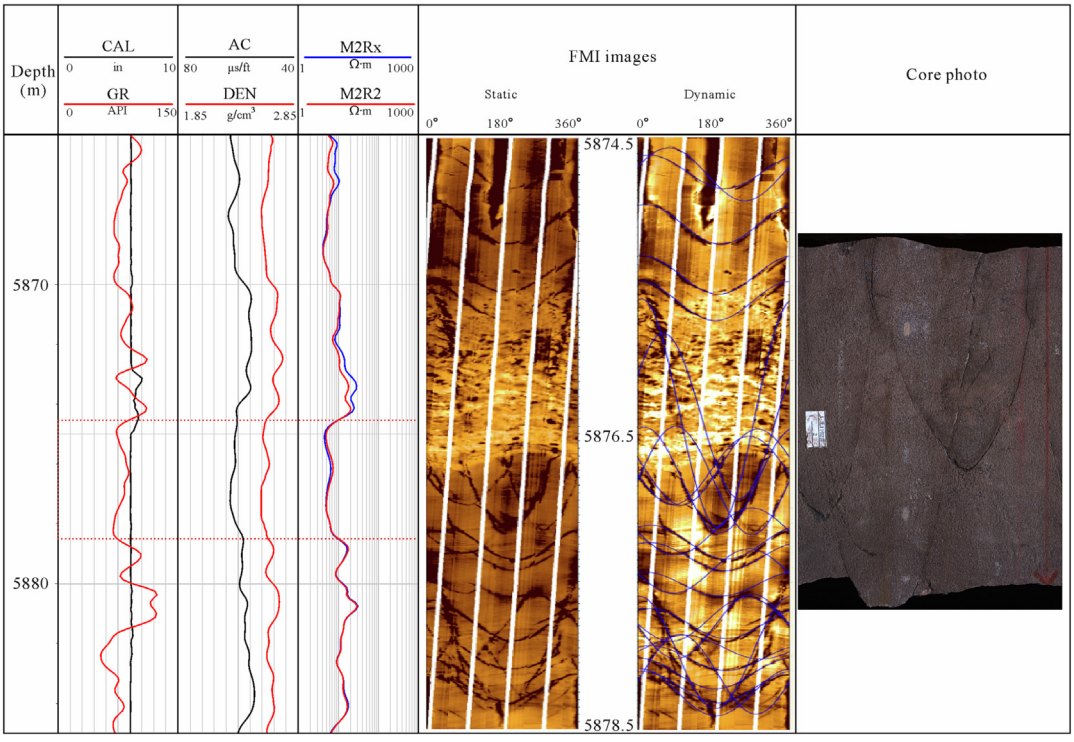

Fig. 10. Well log (conventional and image log) responses of natural fractures of Cretaceous Bashijiqike Formation in Kuqa depression, Tarim Basin of China.

fractures. The amplitudes of full wave-forms will show strong attenuations, showing V-shape interferometric fringe due to the presences of fractures (Fig. 12).

The depth of investigation of electrical image logs are only flushed zones, therefore image logs can hardly evaluate the extension length of fracture into the formation (Lai et al., 2018). Therefore, Azimuthal Resistivity Image (ARI) log must be integrated to evaluate the fracture extension length. The ARI log is developed from lateral resistivity logs, and ARI logs have low image quality (resolution) but higher depth of investigation than FMI image logs (Fig. 13). In addition, the variable density image of array sonic logs can also identify the fractures by their "V" shape interferometric fringes (Fig. 13). The sonic waveform is a record of sonic energy level versus time of arrival, and the sonic amplitude is a log that records the first arrival energy in millivolts, therefore fractures will cause the sonic amplitude attenuation besides cycle skipping (Fig. 13).

Additionally, the extension length of fractures in the radial direction should also be evaluated in terms of hydrocarbon productivity. However, borehole image logs can only detect the

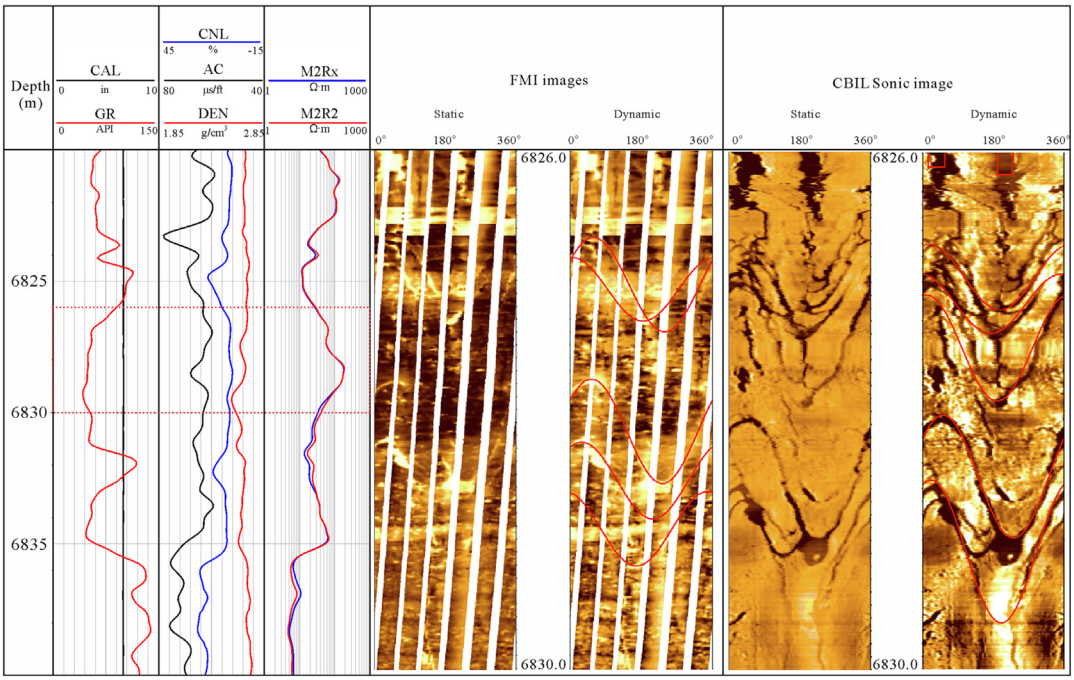

Fig. 11. Appearances of natural fracture on electrical image logs and ultrasonic image logs in oil based drilling muds.

fractures around the borehole with depth of investigation of 10–20 cm (Lai et al., 2018). Therefore, for open fractures which do not crosscut the boreholes, image logs are difficult to detect. Consequently, the ARI and sonic image logs are needed to detect these fractures (Fig. 13). The natural fracture recognized by core observation within Fig. 13 have dark continuous sinusoids with dip direction and dip angle of 205° and 65° on the electrical image logs. Then the array sonic logs and ARI image have also captured this fracture, therefore the fracture has a long extension length (Fig. 13).

For closed fractures (sealed by cements), bright sine waves can be observed on the electrical image logs, indicating the fractures are filled by resistive materials (calcite cements, bitumen) (Fig. 14). The ARI image logs have no evident responses for the closed fractures, and no sine waves will be detected on the ARI images. In addition, the sonic image logs can hardly sense the presences of these closed fractures (Fig. 14). Consequently, closes fractures have no connectivity and they hardly can be recognized by ARI and sonic logs.

Induced fractures, which are formed by drilling processes and have very low extension depth, will evidently be recognized by FMI image logs. However, neither sonic image logs nor ARI images logs can detect the presences of induced fractures (Fig. 15). Consequently, induced fractures are supposed to have no or very low contribution for hydrocarbon productivity.

4.1.4.2. Quantitative calculation of fractures parameters. In water based drilling muds, image logs are widely used for determination of fracture attributes (strike, dip direction and dip angle) and status (open, fill or open-fill) (Barton and Zoback, 2002; Nie et al., 2013; Kosari et al., 2015). Additionally, image logs can provide quantitative fracture parameters including fracture porosity, aperture, density and length can be quantitatively calculated through image logs (Tiab and Donaldson, 2004; Khoshbakht et al., 2012; Xu et al., 2016; Lai et al., 2018, 2022) (Fig. 16).

Fracture porosity is the ratio of fracture area to the total area of boreholes. The range of fracture porosity (FVPA), is 0.1% to 5%, and generally less than 0.5% (Fig. 16) (Tiab and Donaldson, 2004; Zeng and Liu, 2010). However, in some cases, fracture can keep a high value up to more than 1.0% where the rocks are heavily fractured.

Fracture aperture (FVAH) or width is also called fracture opening, which is at millimeter scales, is critical in controlling fracture permeability (Fig. 16) (Tiab and Donaldson, 2004; Wilson et al., 2015; Wennberg et al., 2016).

Fracture length (FVTL) is total fracture lengths in a unit area of boreholes (1 m^2), and it can be calculated by the fracture traces on the image logs (Fig. 16) (Tiab and Donaldson, 2004; Ameen et al., 2012).

Fracture density (FVDC) is the numbers of fractures per unit length or cumulative fracture trace lengths per unit area (Fig. 16) (Ameen et al., 2012; Wennberg et al., 2016).

4.2. Sedimentary geology

4.2.1. Recognition of lithology and lithofacies

Prediction of lithology and lithofacies from well logs has the potential to extend observations from the core scale (centimeters to meters) to the well scale, allowing facies to be mapped (Nabawy and Géraud, 2016; He et al., 2019). Core facies can be defined based on their sedimentological and mineralogical characteristics, including lithology, grain size, and cross beddings (He et al., 2019). Conventional well logs that can be used for lithofacies prediction include gamma ray (GR), resistivity (Rt), and photoelectric factor (Pe), etc. (He et al., 2019). In addition, image logs of high vertical resolution, play an important role in lithofacies interpretation. Image logs measure grain size, rock composition, bedding dips, and sedimentary structure at the millimeter scale, are critical for facies interpretation (Keeton et al., 2015; Brekke et al., 2017). The borehole image logs, combining with cores and conventional logs (GR and RT, etc), can be used to interpret the lithology, sedimentary textures and then lithofacies associations of sedimentary rocks.

Previous studies and the core sedimentology suggested the Chang 7 member (Member 7 of the Upper Triassic Yanchang Formation) in Ordos Basin was deposited at the most expansive stage of the Ordos Lake, and the lithology consists of shales and black

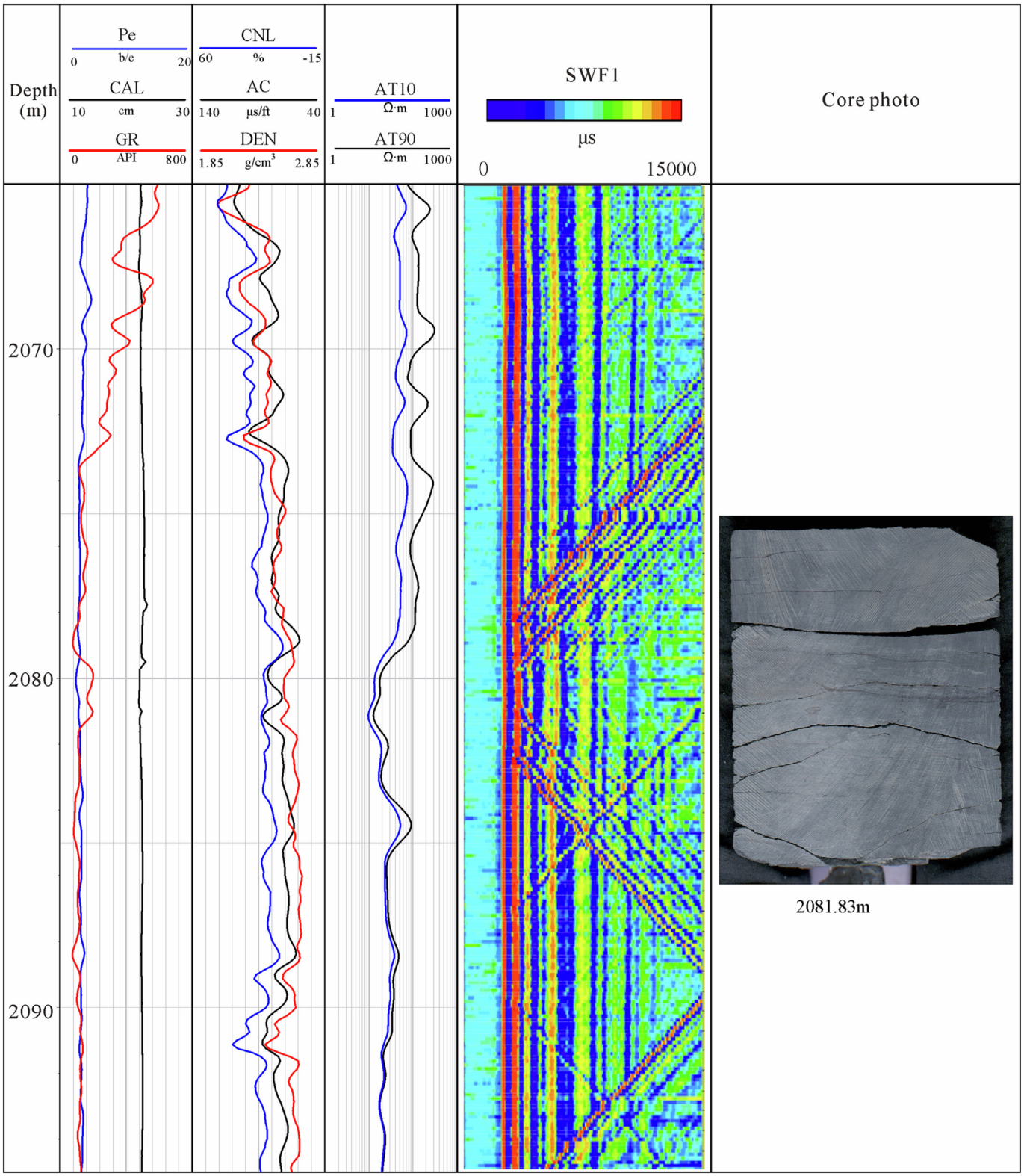

Fig. 12. Well log response of fractures on DSI full-waveform.

mudstones interbedded with thin beds of gravity-flow fine-grained sandstone and siltstone (turbidites, sandy debris and slumps) (Li et al., 2011; Qiu et al., 2014; Lai et al., 2016).

The image log facies of informal stratigraphic Unit A (intervals within 2033 to 2035 m) in Fig. 17 is recognized mainly as massive facies with locally distributed dark spots (speckled facies). No evident internal structures are observed from the dynamic images, which imply the structureless massive sandstones. The core observation shows that the lithology of this unit is grey massive sandstone with floating mudstone clasts but without cross beddings (Fig. 17), therefore the core data supports the image log observation. The GR values remain uniform (low-amplitude box-shaped)

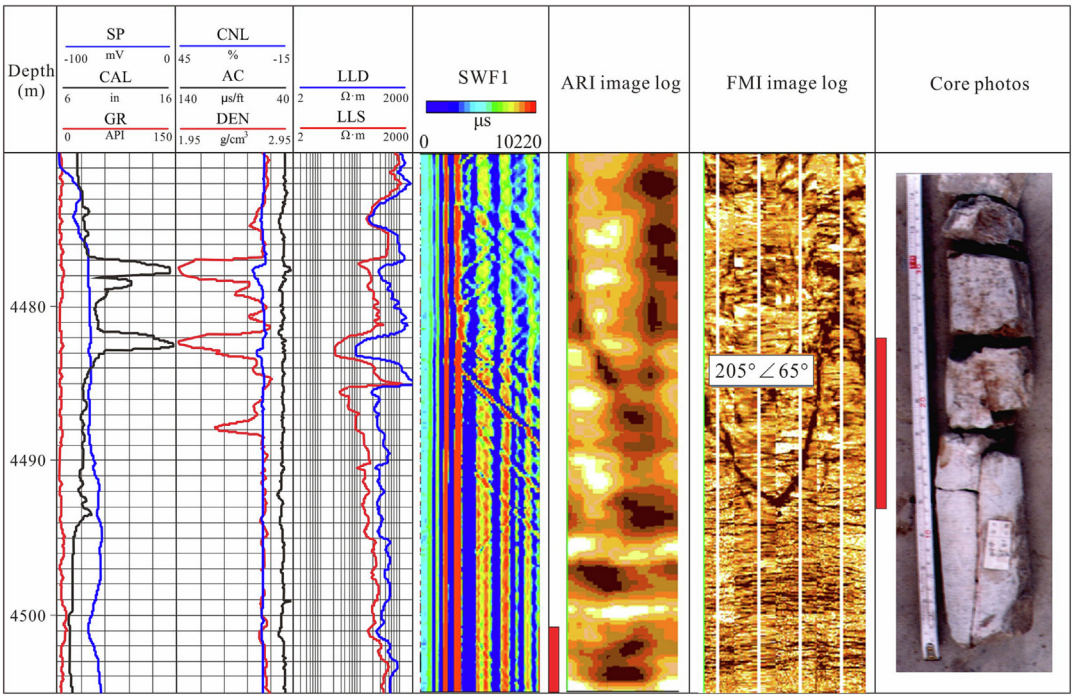

Fig. 13. Fracture extension and effectiveness evaluation using FMI, ARI electrical image logs and DSI sonic logs. The array sonic logs and ARI image have captured this fracture, therefore the fracture has a long extension length.

throughout the entire interval provides further evidence for the lack of a grain-size trend (c.f., Keeton et al., 2015). These massive clast-rich sandstones are commonly interpreted as sandy debris flows (Li et al., 2011; Zou et al., 2012; Ran et al., 2016).

The image log facies of Unit B (intervals within 2058 to 2060 m) in Fig. 17 is recognized as truncated facies, and the rapid color changes from dark to bright is interpreted as the erosional surface. The image facies are stacked from dark massive to low laminated facies in a general fining upward trend. The core data supports this interpretation since the massive mudstone layers are scoured by the overlying fine-grained laminated sandstones (Fig. 17). The fine-grained sandstone exhibits a sharp basal contact with adjacent mudstone and thin layers of normal grading (Zou et al., 2012). Turbidites in Chang 7 member in Ordos basin are characterized by incomplete Bouma sequences (Zou et al., 2012; Qiu et al., 2014), and these fine-grained sandstones with thin layers of normal grading are interpreted to be deposits of turbidity currents from suspension settling (i.e., turbidites) (Zou et al., 2012; Ran et al., 2016).

Laminated image facies are recognized of Unit C (intervals within 2070 to 2072 m) in Fig. 17, and this indicated the appearance of shales. Even the static images are very bright, and laminations are well imaged in the dynamic images. Dark spots are interpreted as pyrite nodules, and the well-developed lamination in mm scale with low dip angles refer to the shale breaks (Fig. 17). The high GR amplitudes and very high resistivity values supports this interpretation, and give signatures to the richness in organic matters (Fig. 17). The lithology, sedimentary structures and lithofacies associations of the whole intervals (2030–2070 m) are interpreted by image logs, and combined with core observation and conventional well logs of GR and RT (Ran et al., 2016).

However, there are some special petrophysical behaviors of lithology, for instance, high gamma sandstones. Clean sandstones are suggested to have low gamma-ray readings (<60 API) (Sarhan, 2019), but high GR values (>100 API) will be encountered when they are rich in radioactive K-rich rock fragments and U-rich deposits (Fig. 18).

Consequently, the high-resolution core-calibrated borehole image logs and conventional logs enable the interpretation of textural and lithological facies in terms of depositional elements (Xu, 2007; Xu et al., 2009; Folkestad et al., 2012; Muniz and Bosence, 2015).

4.2.2. Depositional facies description

Identification of depositional microfacies is based on both qualitative and quantitative descriptions of mineral composition, texture, sedimentary structures, grain-size distribution, bioturbation, and these data can be obtained from core and outcrop observation (He et al., 2019). However, the description of depositional facies core is limited due to the lacking of continuous coring data and related core analysis data. Therefore, the well log data, especially the high resolution image logs, which provide continuous digital records of information on composition, texture, paleoflow directions, and sedimentary sequences, play important roles in interpretation of depositional microfacies and depositional trends (Donselaar and Schmidt, 2005; Xu, 2007; Folkestad et al., 2012; Lai et al., 2021).

4.2.3. Sequence stratigraphy analysis

Sequence stratigraphy aims to establish a chronological stratigraphy framework, which can help govern sedimentary processes and improve the success of hydrocarbon exploration (Catuneanu et al., 2009; Melo et al., 2021). Rapid and impressive evolution has been witnessed in sequence stratigraphy during the past several decades (Mansour et al., 2018). Sequence stratigraphy is a collection or "toolkit" of methods intended for various spatial scales, depositional context, data input (Donovan, 2010). Electric well logs, which can recognize sequence boundary and indicate the gradual rise of relative sea or lake level, are widely used for sequence stratigraphy analysis (Kadkhodaie and Rezaee, 2017; Ayyad et al., 2020; LaGrange et al., 2020; Magalhães et al., 2020).

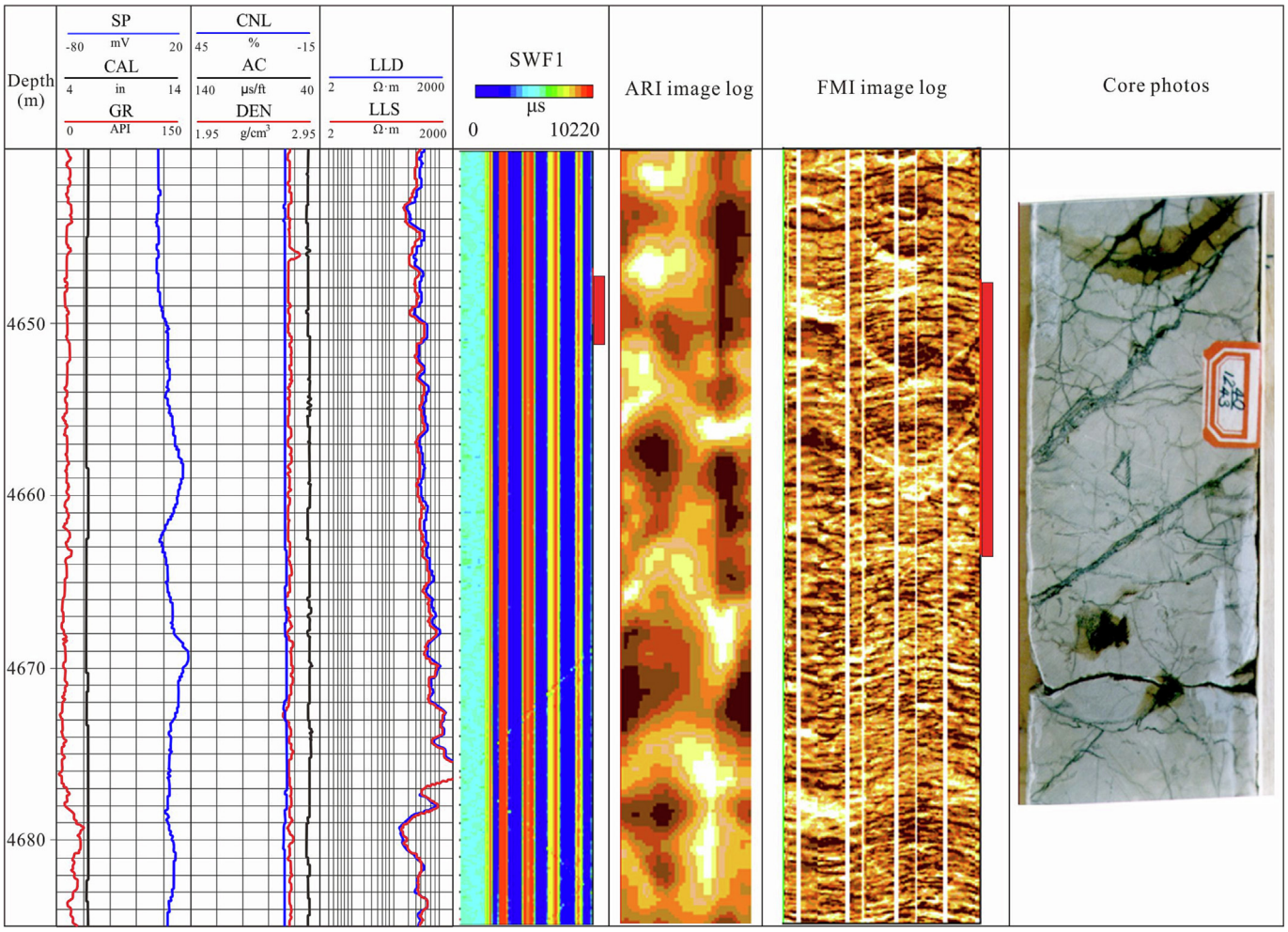

Fig. 14. Application of FMI, ARI electrical image logs and DSI sonic logs in evaluating closed (sealed) fractures. The closes fractures have no connectivity and they hardly can be recognized by ARI and sonic logs.

Sequences are subdivided into systems tracts, which are bounded by sequence surfaces (sequence boundary and maximum flooding surfaces). Stratal stacking patterns (progradation, retrogradation, aggradation) varied significantly for various systems tracts (Catuneanu et al., 2009; Kadkhodaie and Rezaee, 2017). Low-stand system tracts (LST) form during sea level fall, while transgressive systems tracts (TST) forms as sea level start to rise. TST are characterized by retrogradational parasequence, while high-stand systems tracts (HST) are recognized by aggradation and then progradation of parasequences (Kadkhodaie and Rezaee, 2017). Sequence boundaries are recognized as rapid changes in lithological associations due to sea level fall (Sfidari et al., 2021). The LST and HST are favorable for development of reservoirs. Source rocks are usually related to maximum flooding surfaces and TST, which are characterized by low sedimentation rate but constant supply of organic matters (Mansour et al., 2018; Souza et al., 2021).

The Upper Triassic Yanchang Formation in Ordos Basin (West China) is a super long-term sequence cycle (2rd order sequence), and the Chang 7 lacustrine black oil shales and mudstones correspond to the Maximum Flooding Surfaces (MFS) (Qiu et al., 2014). Five long-term 3rd order sequence cycles corresponding to five regional lake transgression-lake regression sedimentary cycles can be identified. For each long-term sequence cycles, LST, TST and HST can be recognized according to the curve shapes, and stacking patterns of well logs (GR and RT) (Fig. 19). The LST is characterized by aggradation stacking patterns, with the GR curve mainly box-shaped, and indicates a high depositional energy, and the lithology are sandstones. The TST is typical of high GR and high resistivity, indicating a high lake level, and organic matter-rich shales are encountered. The HST is characterized by coarsening upward sequence with retrogradation or aggradation stacking patterns, and the GR curve is typically of serrated funnel-shapes (Fig. 19).

Wavelet transform, which is a signal processing tool, and provides a new way to divide high-resolution sequence stratigraphy using well logs (Kadkhodaie and Rezaee, 2017). The principles and methods of wavelet transform are described in previous studies (Kadkhodaie and Rezaee, 2017). The wavelet conversion, or even Fourier transform of gamma ray and spontaneous potential curves, will provide the time frequency characteristics, which can be applied in the sequence stratigraphic subdivision, with the results more objective and effective (Fig. 20) (Wang et al., 2013; Kadkhodaie and Rezaee, 2017). In addition, wavelet transform can reveal the hidden information on Milankovitch cycles, which can be further used for paleoclimate analysis (Kadkhodaie and Rezaee, 2017; Falahatkhah et al., 2021).

4.3. Petroleum geology

4.3.1. Calculation of petrophysical parameters

Conventional (full suite) logs evaluation can be used to derive porosity, water saturation, and permeability (Yarmohammadi

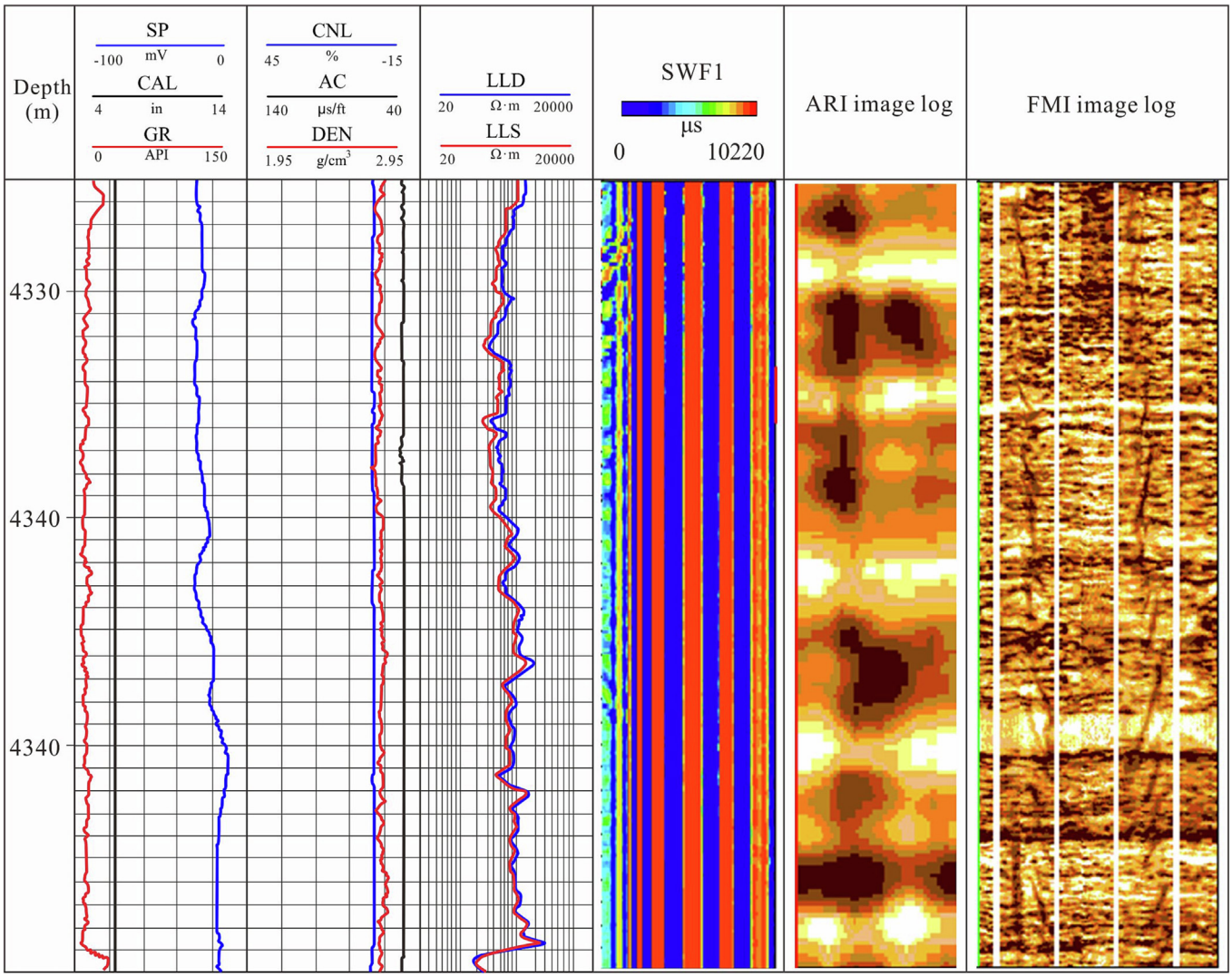

Fig. 15. Responses of induced fracture on FMI, ARI electrical image logs and DSI sonic logs.

et al., 2020). Finding the hydrocarbon presented in the formation is the initial goal of well log interpretation (Luthi, 2001; Tiab and Donaldson, 2004; Nabawy and El Sharawy, 2018). The first questions of well log data that need to be answered are what is the type of fluids and where are the hydrocarbons? (Ellis and Singer, 2007). Well logs can be used for directly qualitative recognition of hydrocarbon (oil or gas) bearing layers. For instance, the Layer 1 (5971.5–5985.5 m) in Fig. 21 is a typical gas bearing layer, and the GR log is characterized by box-shape and low amplitude, indicating low shale content (Fig. 21). The three porosity logs give a relatively high porosity, and the deep and shallow resistivity logs have evident deviations (Fig. 21). Conversely, the water zone is characterized by rather low-resistivity readings and the lack of separation between the deep and shallow laterolog readings (Ellis and Singer, 2007). Additionally, the hydrocarbon-mud logs (C1, C2, C3, Total gas) all show high values in Layer 1, and this indicates a high gas bearing property. Consequently, the Layer 1 in Fig. 21 can be easily interpreted as gas bearing layer according to the comprehensive analysis of well log data.

4.3.2. Shale content and porosity

Well logs can be quantitatively used for calculation of petrophysical parameters including shale content, porosity, permeability and hydrocarbon saturation (Rider, 2002; Tiab and Donaldson, 2004; Ellis and Singer, 2007).

Gamma-ray tool measures the radioactivity (Serra, 1984), and a GR log is commonly used for determination of shale content, where high GR readings imply high shale content (Fig. 21). Mudstone intervals (organic-poor) generally exhibit high GR but low resistivity (Shalaby et al., 2019; Wang et al., 2019).

Porosity (φ) is that fraction of the volume of a rock (Ellis and Singer, 2007), and the three porosity logs (AC, CNL, DEN) can be used for the calculation of porosity (Iqbal et al., 2018).

The sonic log measures the interval transit time (Δt), which is the shortest time for a compressional wave to travel through 1 ft (or 1 m) of formation parallel to the wellbore (Tiab and Donaldson, 2004). The time average equation to calculate porosity is written as (Eq. (5)) (Tiab and Donaldson, 2004; Bateman, 2020). However, in shaly sandstones, the sonic velocity of shales is different from sandstones, and the Eq. (5) should be rewritten as Eq. (6):

$$\varphi_s = \frac{\Delta t - \Delta t_{ma}}{\Delta t_f - \Delta t_{ma}} \frac{1}{C_p} \tag{5}$$

$$\varphi_s = \frac{\Delta t - \Delta t_{ma}}{\Delta t_f - \Delta t_{ma}} \frac{1}{C_p} - V_{sh} \frac{\Delta t_{sh} - \Delta t_{ma}}{\Delta t_f - \Delta t_{ma}} \tag{6}$$

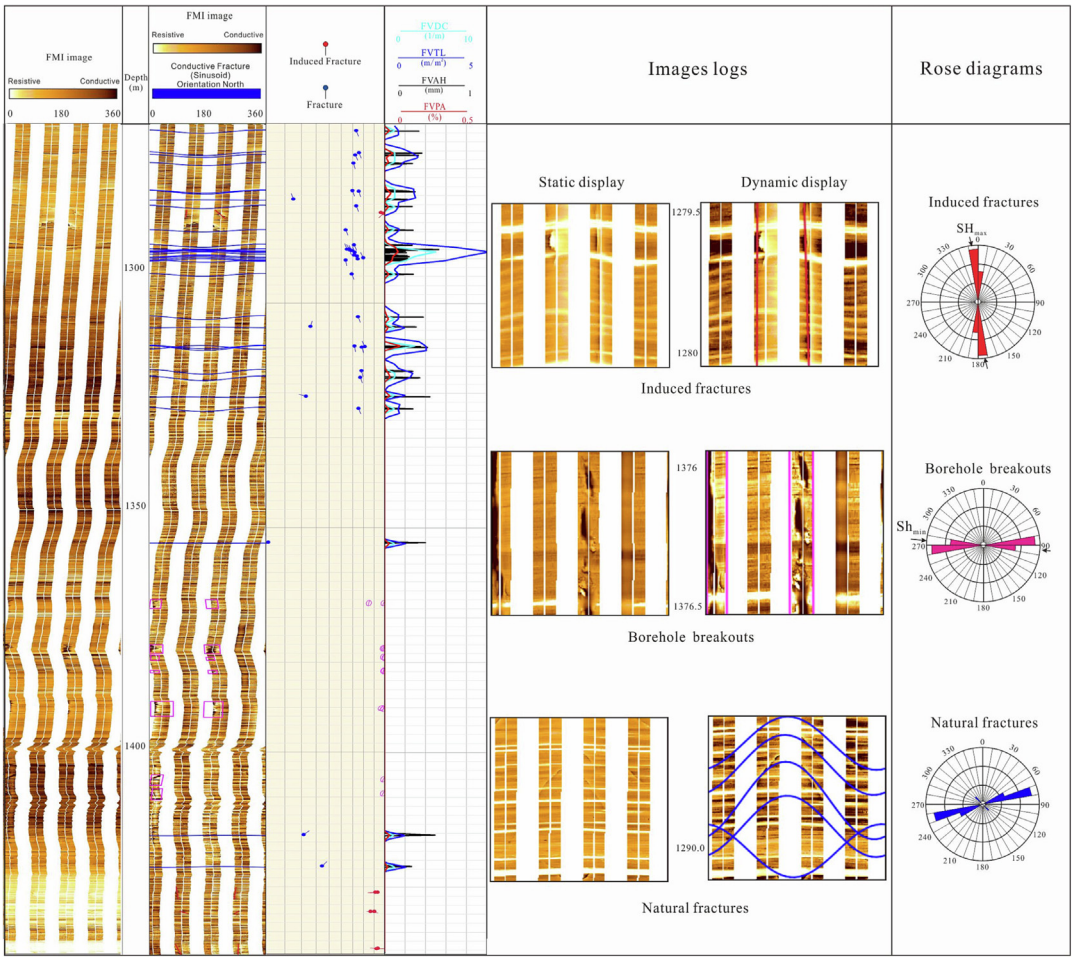

Fig. 16. Comprehensive evaluation of natural fractures, induced fractures and fracture effectiveness using image logs.

In Eqs. (5) and (6), Δt_f is fluid sonic transit time, and is assumed to be 189 μs/ft, and Δt_{ma} (matrix sonic transit time) for sandstones is 55.5 μs/ft. φ_s is sonic porosity. Δt is sonic transit time from well logs, V_{sh} is the shale (clay) content. C_p is compaction correction factor (ranging from 1 to 2), and C_p is taken as 1.0 when no compaction correction is used Tiab and Donaldson (2004).

Density log can also be used for porosity calculation using the following Eqs. (7) and (8) (Tiab and Donaldson, 2004; Stadtmuller et al., 2018). In Fig. 4, the porosity is derived from the density logs, and are coinciding with the core-measured porosity (Fig. 21).

$$\varphi_D = \frac{\rho_{ma} - \rho_b}{\rho_{ma} - \rho_f} \tag{7}$$

$$\varphi_D = \frac{\rho_{ma} - \rho_b}{\rho_{ma} - \rho_f} - V_{sh}\frac{\rho_{ma} - \rho_{sh}}{\rho_{ma} - \rho_f} \tag{8}$$

In Eqs. (7) and (8), ρ_f is fluid density, and is assumed to be 1.0 g/cm^3 (fresh muds) or 1.1 g/cm^3 (salty drilling muds), and ρ_{ma} (matrix density) for sandstones is 2.65 g/cm^3. φ_D is density-derived porosity. ρ is bulk density from well logs, V_{sh} is the shale (clay) content.

Neutron logs also can also be used to determine porosity, however, neutron porosity is affected by the shale content, organic matter content, and presence of gas, therefore neutron logs are needed to calibrate with core-measured porosity to build the predictable model of porosity. Actually, modern neutron log data is recorded directly in apparent porosity units, and they can be used for porosity calculation with a correction. In addition, porosity can also be determined from the combination of neutron and density logs "crossover of neutron log versus density log" (Tiab and Donaldson, 2004; Bateman, 2020).

4.3.3. Permeability

There are no direct logging tools to measure permeability, however, permeability can be estimated according to the correlation relationships between core-measured permeability versus core-measured porosity (Fig. 21). In addition, NMR logs which can provide the information of NMR porosity, free fluid index (FFI), bulk volume irreducible (BVI), geometric mean of the T_2 distribution (T_{2gm}) (Tan et al., 2014; Wang et al., 2020). Furthermore, DST (drill stem test), modular dynamics formation tester (MDT), as a new technique, can estimate permeability in natural conditions (but mostly effective permeability) (Liu et al., 2005). Wireline repeat formation tester (RFT) can be further used for identifying formation pressure and fluid contacts (Radwan et al., 2021).

There are commonly two models used to derive permeability using the NMR logs, known as Schlumberger Doll Research (SDR) Eq. (9) and Coates model Eq. (10).

$$K_{SDR} = D\varphi^4 (T_{2gm})^2 \tag{9}$$

K_{SDR} (mD) is permeability from SDR model, and D is a constant (Glover et al., 2006; Rezaee et al., 2012).

Coates et al. (1991) developed the Coates model to derive permeability using free fluid index (FFI) and the bulk volume irreducible (BVI) (Eq. (10)):

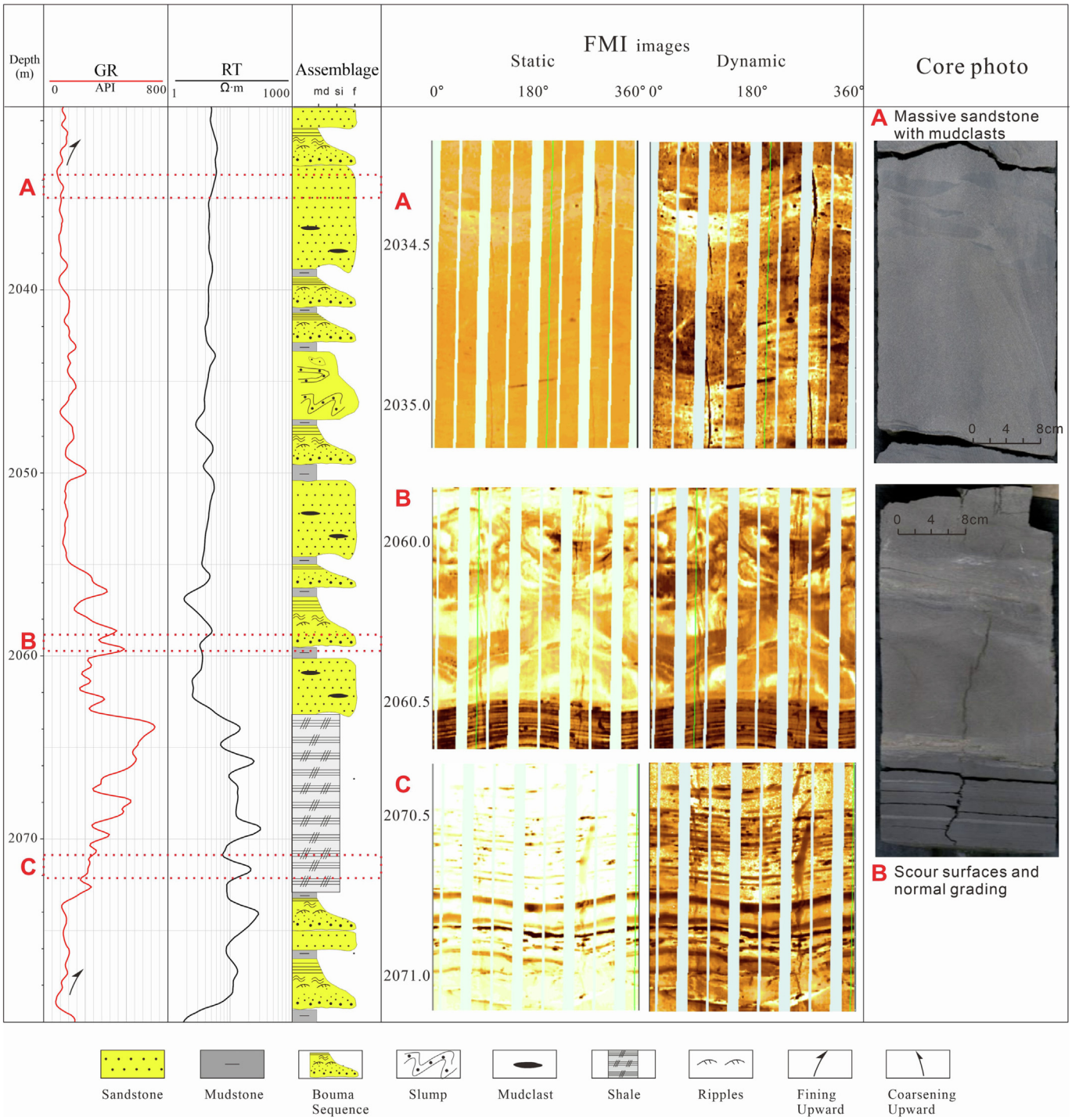

Fig. 17. Lithofacies prediction using image logs combined with cores and conventional logs.

$$K_{NMR} = \left[\left(\frac{\varphi}{C}\right)^2 \left(\frac{FFI}{BVI}\right)\right]^2 \quad (10)$$

K_{NMR} (mD) is permeability from Coates model, and C is a constant (Coates et al., 1991; Rezaee et al., 2012).

4.3.4. Hydrocarbon saturation

Water saturation (S_w) is the fraction of the porosity which contains water (Ellis and Singer, 2007). Archie (1942) proposed the well-known Archie's formula to calculate hydrocarbon saturation (Eqs. (11) and (12)).

$$F = \frac{R_0}{R_w} = \frac{a}{\varphi^m} \quad (11)$$

$$I = \frac{R_t}{R_0} = \frac{b}{S_w^n} \quad (12)$$

F is the formation factor, R_0 is the resistivity of rock which are 100% water saturated, R_w is the water resistivity (Ω·m). I is resistivity index, R_t is true formation resistivity (Ω·m). a is the tortusity factor, b is the lithology factor, m is the cementation exponent; and n is the saturation exponent. Generally, a and b are taken as 1.0, while m

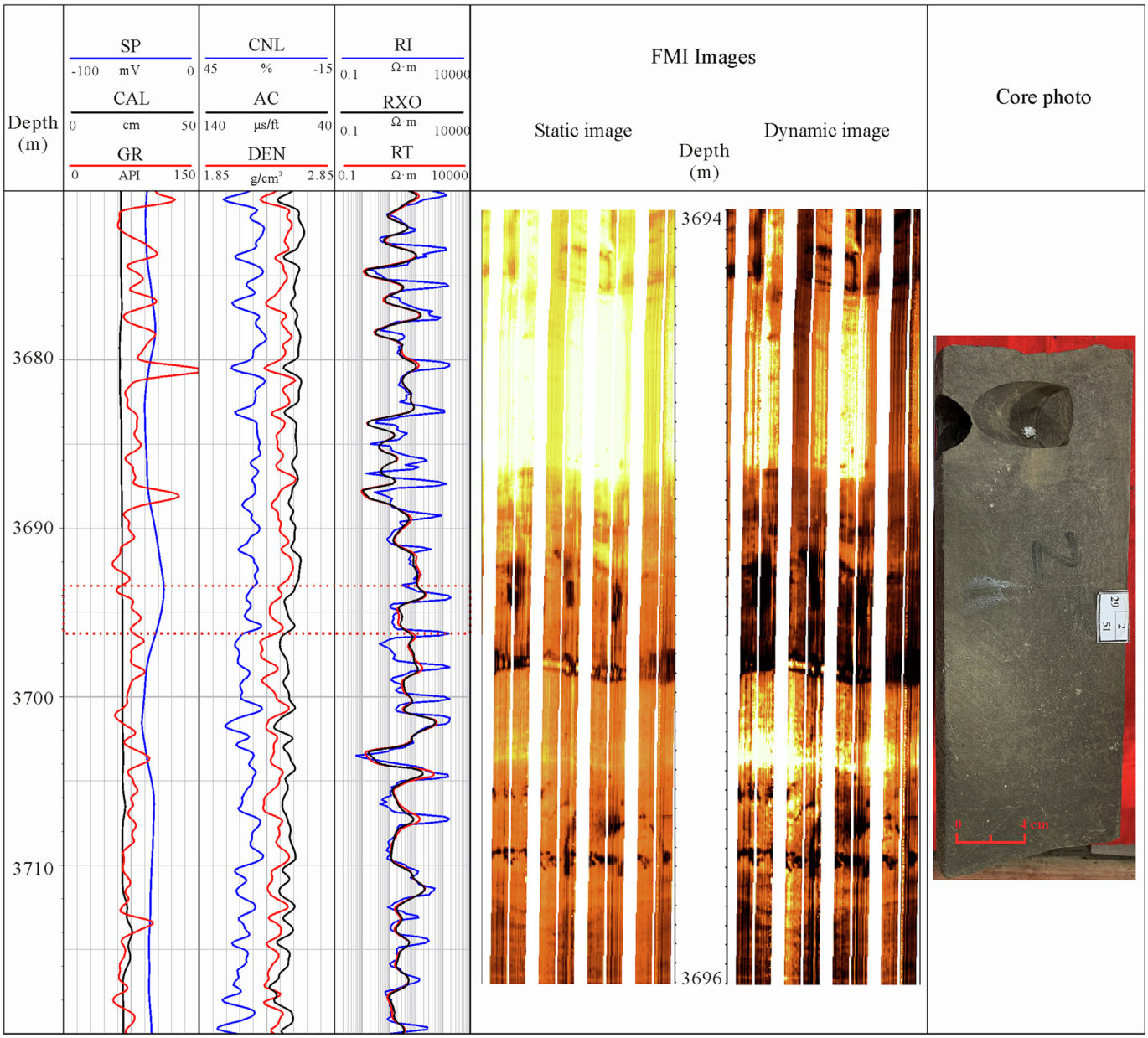

Fig. 18. High gamma sandstones which are oil stained in Jimusar Sag, Junngar Basin of China (Well J10025).

and n are taken as 2.0 (Archie, 1942; Adebayo et al., 2015; Liu et al., 2015; Nabawy, 2015; Qin et al., 2016).

Eqs. (11) and (12) can be combined to derive Eq. (13), and consequently, water saturation (S_w) can therefore be calculated from well logs since a, b, m, n are constant, φ can be derived from density log, and R_t can be directly read from deep lateral logs (Fig. 21). The calculated gas saturation of Layer 1 in Fig. 21 is high than 60%, and implying a good gas bearing interval, and the gas test data prove the results since a daily natural gas production of 335, 302 m^3 is obtained for Layer 1 in Fig. 21.

$$S_w = \left(\frac{abR_w}{R_t\varphi^m}\right)^{1/n} \quad (13)$$

Besides Archie's formula, there are Indonesian formula (without considering cation exchanges) and the Waxman-Smits model (clay has additional conductivity due to cation exchange) (Poupon et al., 1954; Poupon and Leveaux, 1971; Zhu et al., 2022), dual water system (Clavier, et al., 1984), and Simandoux with the capacity for argillaceous correction (Simandoux, 1963; Pan et al., 2022) that can be used to estimate hydrocarbon saturation in reservoirs (Li et al., 2021).

4.3.5. Low resistivity oil layers

High shale content (conductive minerals including mixed layers of illite/smectite), complex pore structure, high irreducible water saturation as well as saline formation water will result in the formation of low-resistivity or low contrast oil pay (Bai et al., 2019; Iqbal et al., 2019). The well log responses of oil layers and water layers become similar, but the resistivity log responses are much lower than the normal and typical oil pays (Bai et al., 2019). Low resistivity oil layers usually display a low-resistivity contrast with a resistivity ratio of oil layer versus water layer less than 2.0 (Hamada and Al-Awad, 2000; Worthington, 2000; Bai et al., 2019).

The low resistivity oil layers have only about 4 Ω·m deep resistivity in the Dongying Formation in Napu Sag of Bohai Bay Basin (Lai et al., 2019b) (Fig. 22). A daily oil production of 57.9 m^3 is

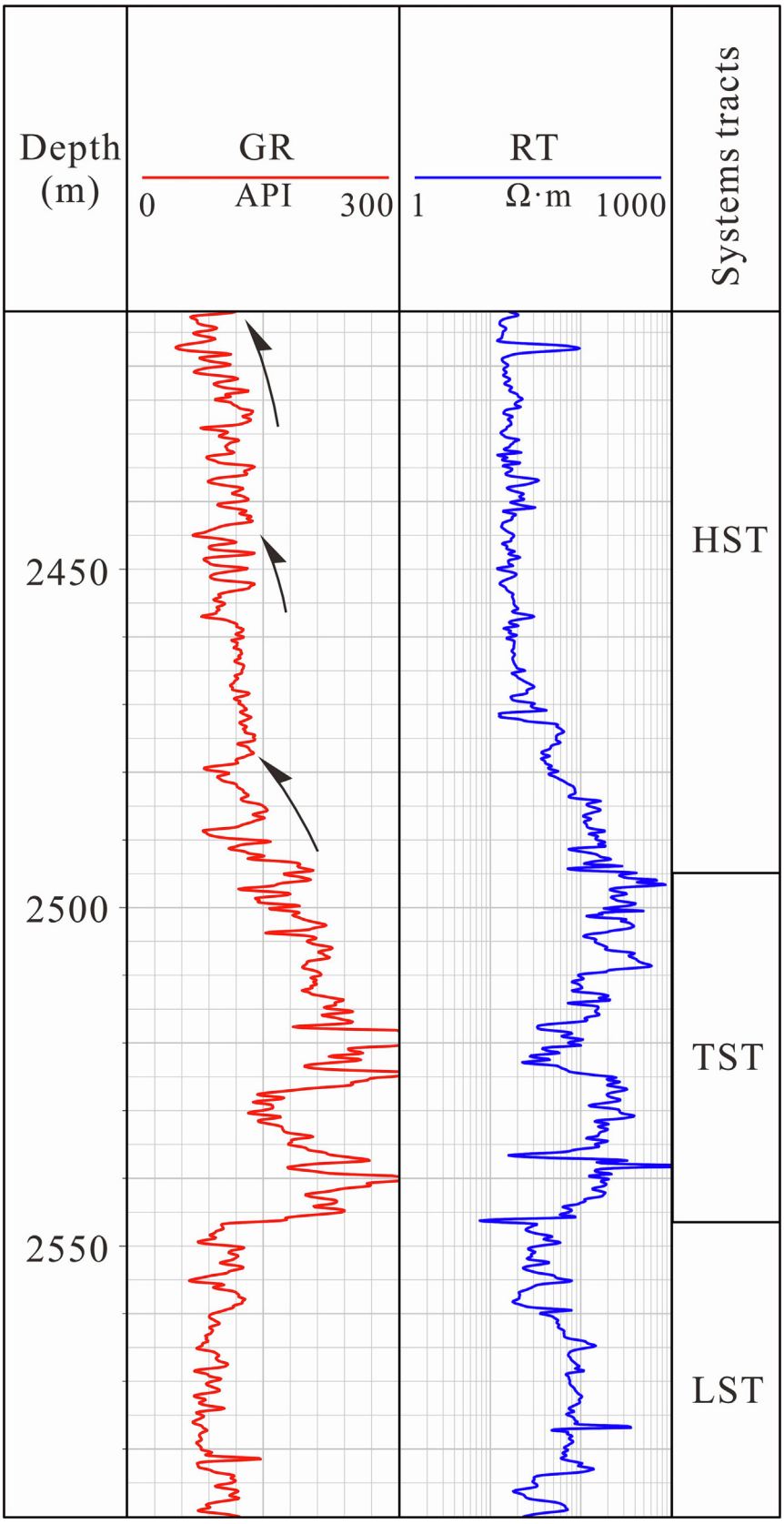

Fig. 19. Well logs showing the vertical patterns of various systems tract.

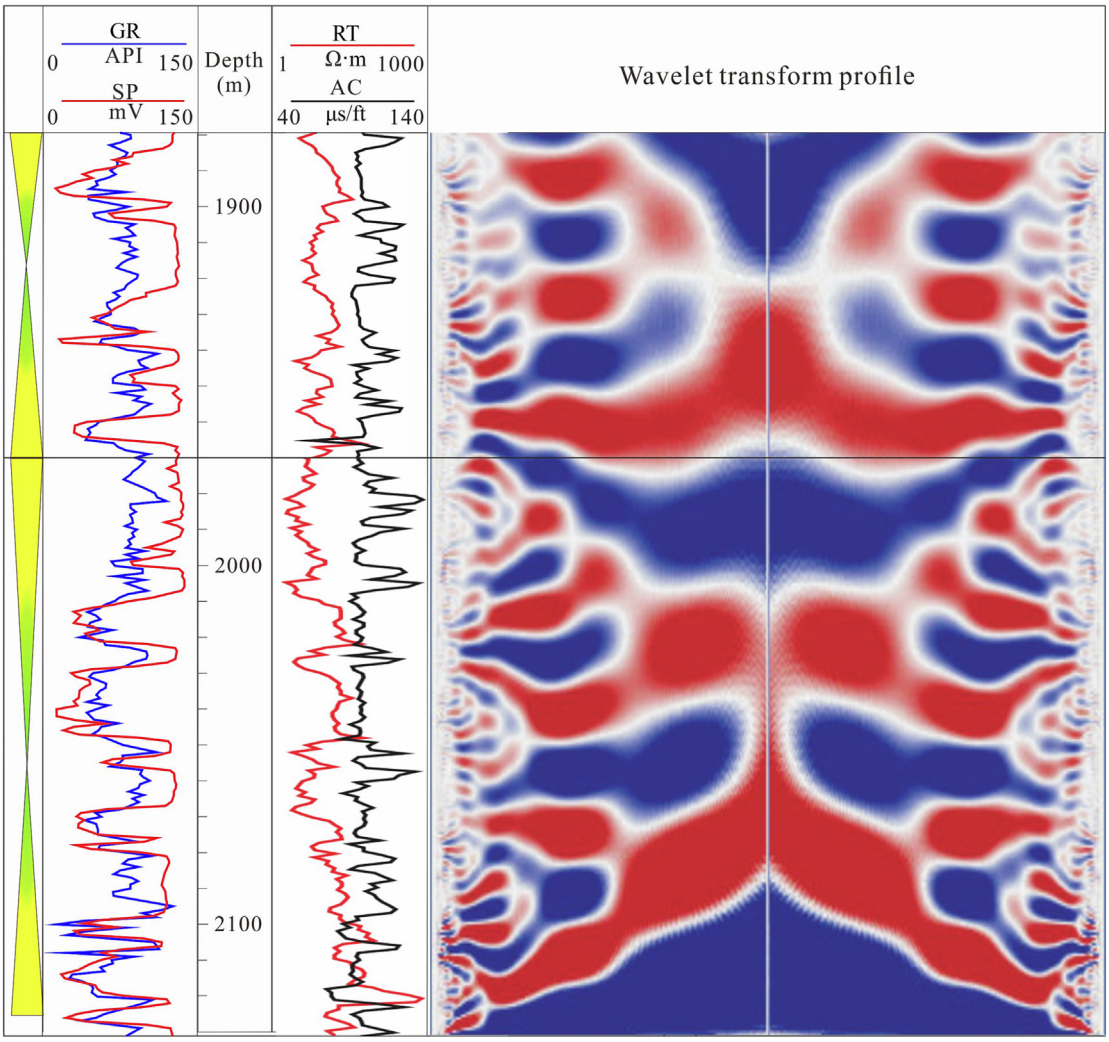

Fig. 20. Sequence stratigraphy division using wavelet frequency analysis (Wang et al., 2013).

obtained during oil test under a drawdown pressure of 4.0 MPa and a choke width of 12.7 mm, and no water is produced (Fig. 22). The highest deep resistivity in Layer 4 is about 10 Ω·m, therefore high rate of oil production can be obtained from these low resistivity oil layers. The water layers in this zone have deep resistivity about 4–5 Ω·m, and the Layer 6 and 7 are typical water layers in which only water is produced during production test (Fig. 23). The above Layer 1, 3 and 4 are oil–water bearing layers, in which both oil and water can be produced from production test, and oil layers show similar deep resistivity of 4–5 Ω·m with water layers (Fig. 23) (Lai et al., 2019b).

Low resistivity or low contrast zones are usually overlooked due to the absence of high-end well logging techniques (Iqbal et al., 2019). Detection of low-resistivity reservoir and the accurate determination of the petrophysical parameters using conventional log reservoirs is challenging (Hamada et al., 2001). NMR logs can provide the transversal relaxation time (T_2) spectrum, longitudinal relaxation time (T_1) spectrum, as well as diffusion coefficient (D) (Tan et al., 2014; Olatinsu et al., 2017; Wang et al., 2020). The NMR data contain abundant information about pore size distribution, porosity, permeability, fluid types (bound and free pore fluid, and hydrocarbon) (Tan et al., 2014; Bauer et al., 2015; Dada et al., 2015), and NMR logs are widely used for fluid property identification and estimating the movable oil content (Wang et al., 2020; Pang et al., 2022). The NMR log has evident advantages in fluid identification over conventional well logs in unconventional oil and gas reservoirs (Fig. 24) (Hamada et al., 2001; Chatterjee et al., 2012; Bai et al., 2019). However, the high cost and long time of acquiring data will limit the application of NMR logs (Hamada et al., 2001).

The NMR logging is very cost-effective tool in the low-contrast resistivity reservoirs, according to the contrast in the relaxation parameters (T_1, T_2 and diffusion) between water and oil and gas (Hamada et al., 2001). Though the low-contrast resistivity oil zone may have similar resistivity with water zone, they show high contrast NMR relaxation times with water zone (Hamada et al., 2001). Hydrocarbon has long T_2 time, while water has short T_2 relaxation time. Differential spectrum method (DSM) can be used to identify the low resistivity oil zone (Hu et al., 2012). MRIL-Prime NMR logging tool can choose different wait time (T_w) and echo spacing (TE), and hydrocarbon and water signals can be divided providing that long and short wait time are used respectively (Hu et al., 2012). The T_w is set as 12.998 s and 1.0 s, respectively, and the T_2 spectra are obtained at the different waiting time (Fig. 24) (Hu et al., 2012). For water layer, low amounts of signals are detected in the differential spectrum, while in the oil layers, there are high signal amplitudes in the differential spectrum (Fig. 24). Consequently, the NMR logs can be used for the fluid property evaluation in low resistivity oil zone.

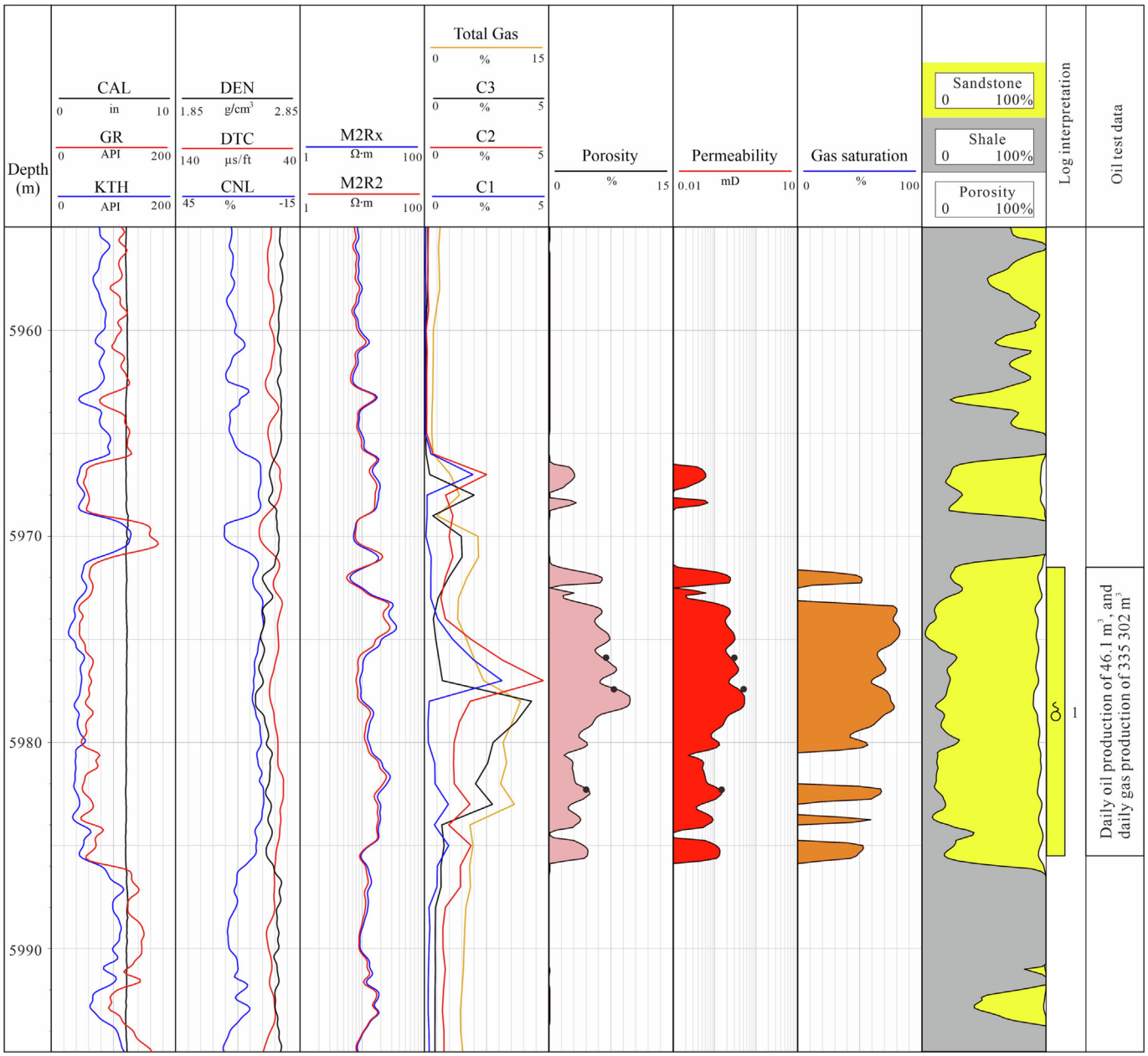

Fig. 21. Application of well log data in calculating porosity, permeability and hydrocarbon saturation. Oil test data: 5971.5–5985.5 m depth intervals, 6 mm choke width, and the drawdown pressure is 81.8 MPa. The daily oil production is 46.1 m^3, and the daily natural gas production is 335,302 m^3.

5. Evaluation of unconventional oil and gas reservoirs

Increasingly in recent years, some oil and gas resources are considered "unconventional" because of the advance completion technologies like hydraulic fracturing and horizontal drilling. Consequently, unconventional oil and gas reservoirs need petrophysical logs to determine how to optimize the sweet spots (Avanzini et al., 2016; Abuamarah et al., 2019; Zou et al., 2019; Lai et al., 2022). Sweet spots are the best zones or horizons for hydrocarbon production, and there are geological and engineering (geomechanical) sweet spots in terms of well log evaluation (Zhao et al., 2019; Lai et al., 2022). Geological sweet spots are reservoirs with high reservoir quality and oil bearing property, while engineering sweet spots refer to the intervals that are favorable for hydraulic fracturing and are characterized by high brittleness index and low *in situ* stress anisotropy (Rybacki et al., 2016; Iqbal et al., 2018; Zhao et al., 2019; Lai et al., 2022). A productive interval for unconventional hydrocarbon resources represents the good combination between geological and engineering sweet spot (Avanzini et al., 2016; Amin et al., 2021; Lai et al., 2022).

5.1. Evaluation of geological sweet spots

The Lucaogou Formation in the Jimusar Sag (Junngar Basin, West China) is characterized by a coexisting combination of tight oil and shale oil (Yang et al., 2019). Petrophysical logs are used to optimize the sweet spots. Geological sweet spots should evaluate the reservoir property (presences of fracture) and oil bearing property (Zhao et al., 2019). Porosity, permeability and oil saturation can be calculated using NMR logs and the NMR T_2 spectrum is presented to show the fluid property (Fig. 25). There are two layers $P_2l_2^2$ (including $P_2l_2^{2\text{-}1}$, $P_2l_2^{2\text{-}2}$, $P_2l_2^{2\text{-}3}$) as well as $P_2l_1^2$ (including

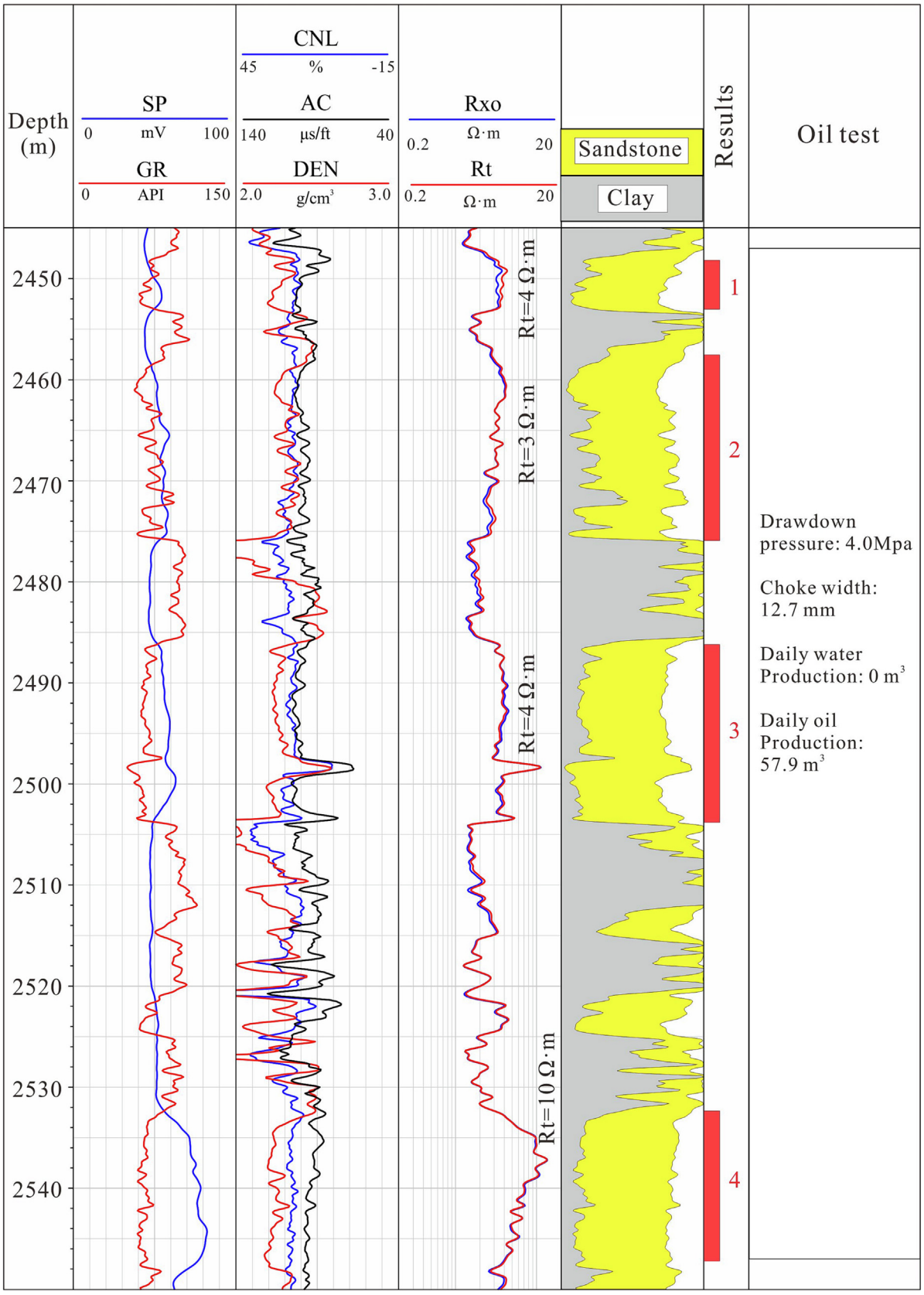

Fig. 22. Low resistivity oil layers with deep resistivity of 4 Ω·m (NP 208).

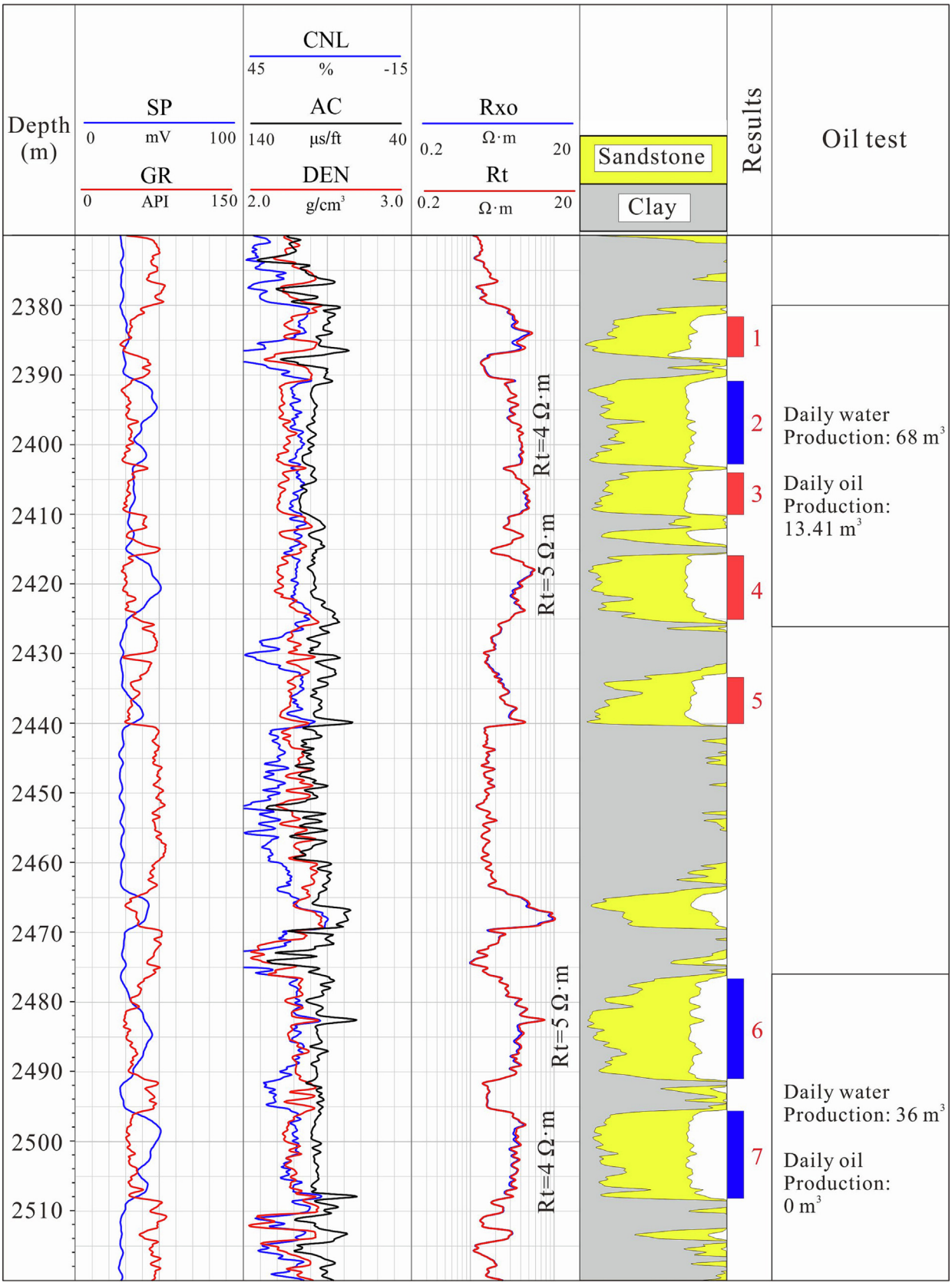

Fig. 23. Water layers and low resistivity oil layers with similar deep resistivity of 4–5 Ω·m (NP 1).

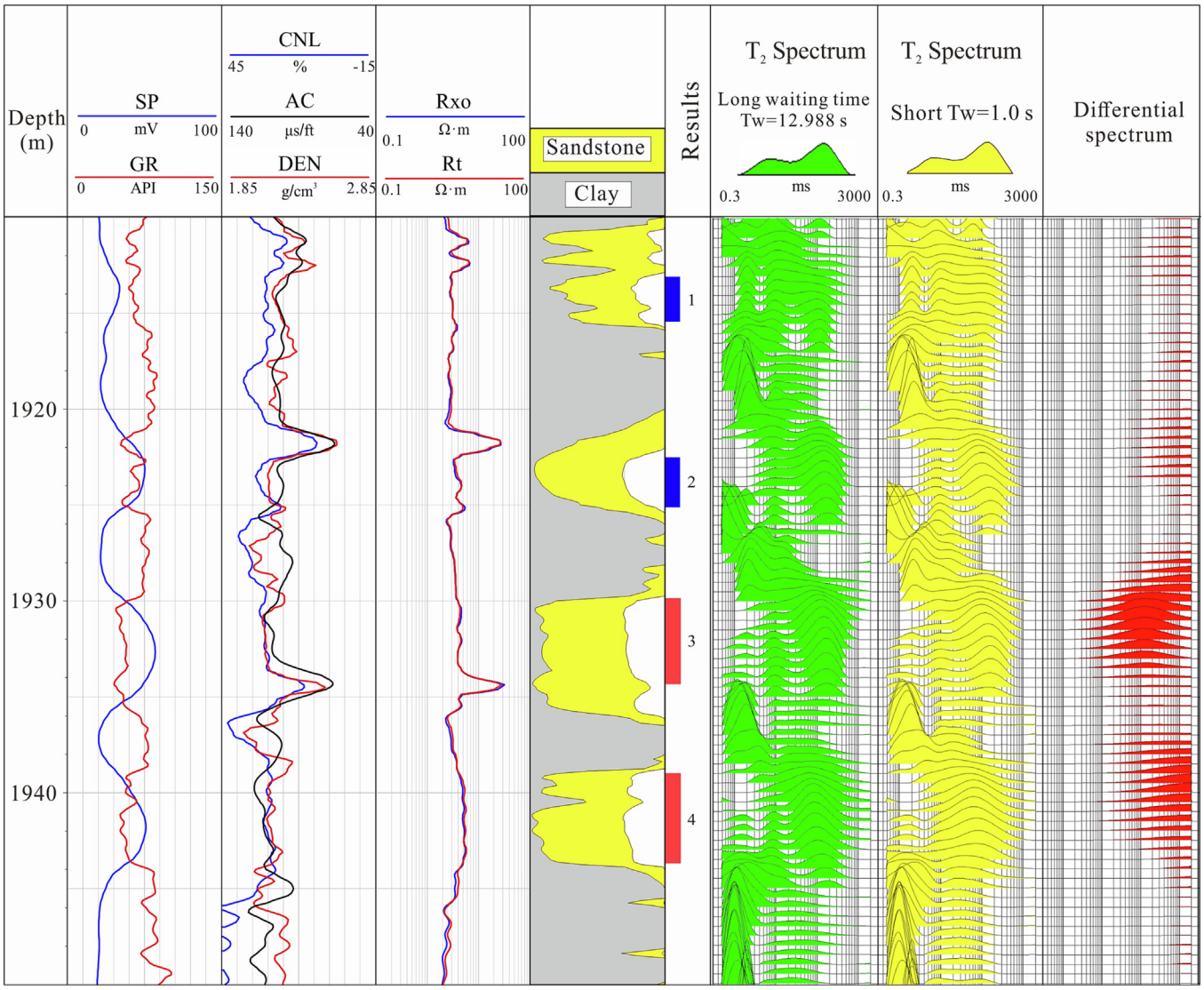

Fig. 24. Application of NMR log (differential spectrum method) in finding low resistivity oil layer (NP1-1).

$P_2l_1^{2\text{-}1}$, $P_2l_1^{2\text{-}2}$, $P_2l_1^{2\text{-}3}$) which are characterized by high porosity, permeability and oil saturation, and the T_2 distributions are wide and even contain tail distributions (Fig. 25). Therefore, these two layers are recognized by petrophysical logs as geological sweet spots. Actually, previous studies also show that $P_2l_2^2$ and $P_2l_1^2$ are two sets of "sweet sections" in the Lucaogou Formation in the Jimusar Sag (Yang et al., 2019).

5.2. Evaluation of brittleness and engineering sweet spots

Unconventional oil and gas reservoirs have no natural productivity and need hydraulic stimulation for economic hydrocarbon production (Josh et al., 2012; Rybacki et al., 2016; Schultz et al., 2020). High rates of hydrocarbon production are usually associated with brittle formations (Jarvie et al., 2007; Dong et al., 2018). Engineering sweet spot optimization evaluates brittleness, fracability and *in situ* stress anisotropy (Rybacki et al., 2016; Iqbal et al., 2018; Zhao et al., 2019). The *in situ* stress magnitude determination using well logs are discussed in a previous section. To optimize engineering sweet spots, the calculation of brittleness index is indispensable since brittleness is an important property that should be evaluated for unconventional hydrocarbon resources.

5.2.1. Brittleness index determination

During hydraulic fracturing, rocks are needed to be brittle enough to initiate fractures within and keep such fractures open (Josh et al., 2012; Avanzini et al., 2016). The layers with high brittleness index (brittle layers) are considered prospected for fracturing (Rickman et al., 2008; Sondergeld et al., 2010; Herwanger et al., 2015; Iqbal et al., 2018). Ductile rock tends to heal natural and artificial fractures and is not favorable for hydrocarbon production (Rickman et al., 2008; Guo et al., 2015; Lai et al., 2015; Iqbal et al., 2018). Therefore brittleness evaluation using well logs are of utmost importance for better design of fracturing treatment (Rickman et al., 2008; Iqbal et al., 2018).

Brittleness is related to Young's modulus and Poisson's ratio from a geomechanical perspective (Iqbal et al., 2018). Brittleness can be evaluated by the combination of these two parameters (Rickman et al., 2008; Iqbal et al., 2018). There are typically two methods for calculating brittleness index, and they include the geomechanical method and ratio of brittleness minerals (Lai et al., 2015; Zhao et al., 2019). One commonly used method is to calculate brittleness index by using mechanical parameters (Iqbal et al., 2018). The brittleness index (%) in this way can be defined as the average of the BI_E and BI_ν (Eqs. (16)–(18)) (Guo et al., 2013; Lai et al., 2015; Iqbal et al., 2018).

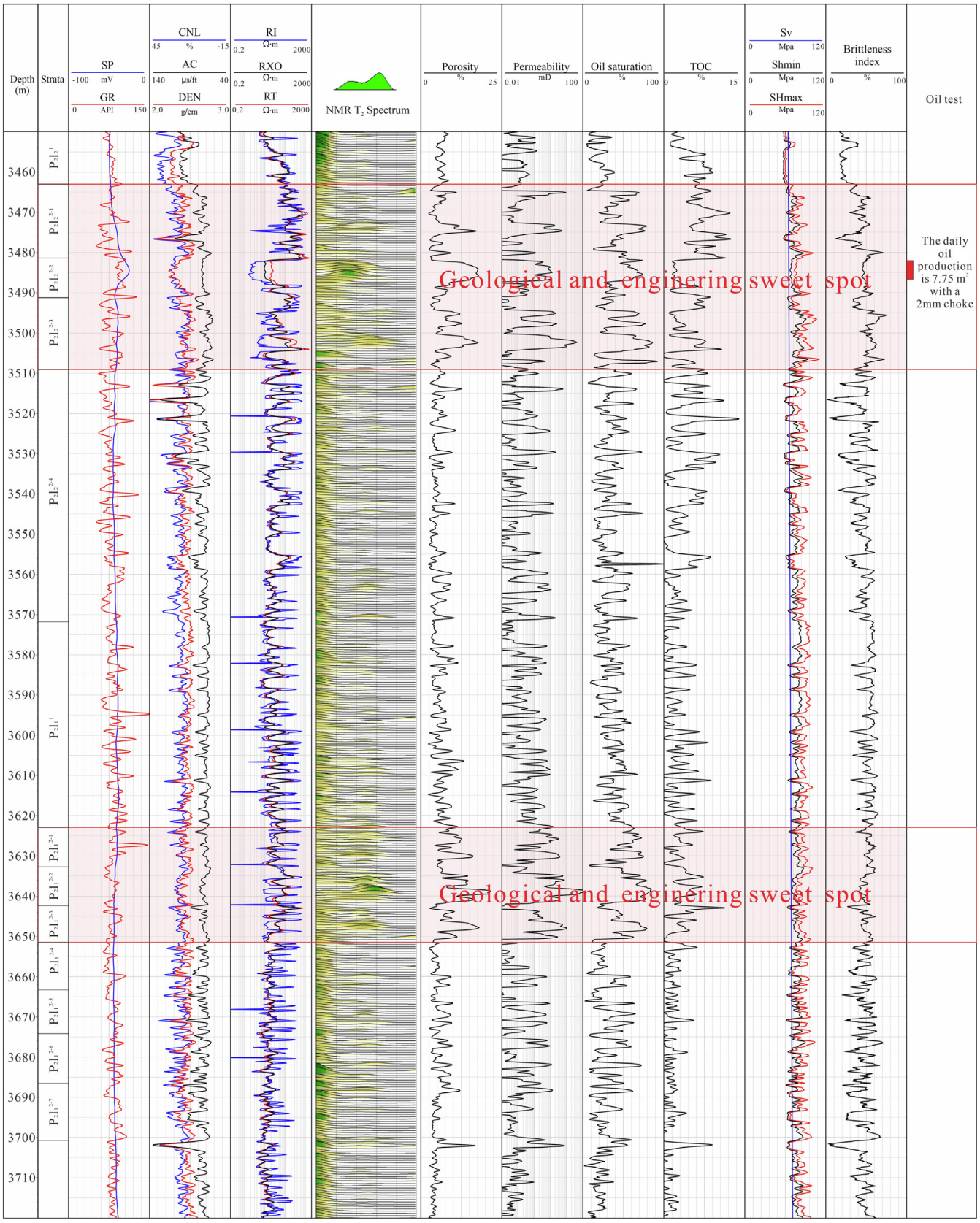

Fig. 25. Comprehensive well log evaluation of lithology, reservoir property, hydrocarbon bearing property, electronic well log responses, source rock property, brittleness, and *in situ* stress magnitude and direction (Well Ji 10024). Two sweet spots are optimized, and the daily oil production is 7.75 m^3 with a 2 mm choke at 3482.0–3486.5 m depth intervals.

$$BI = \frac{BI_E + BI_v}{2} \times 100\% \quad (16)$$

$$BI_E = \frac{E - E_{\min}}{E_{\max} - E_{\min}} \quad (17)$$

$$BI_v = \frac{v - v_{\max}}{v_{\min} - v_{\max}} \quad (18)$$

$E_{\min}$ and $E_{\max}$ are the minimum and maximum Young's modulus, while $v_{\min}$ and $v_{\max}$ are the minimum and maximum Poisson's ratio. The dynamic E and v can be calculated from compressional (P waves) wave velocities (m/s) (V_p), shear wave (S waves) velocities (m/s) (V_s) and bulk density log (ρ) data (kg/m^3) (Eq. (19)–(20)) (Lai et al., 2015).

$$E = \frac{\rho}{V_s^2} \frac{3V_p^2 - 4V_s^2}{V_p^2 - V_s^2} \quad (19)$$

$$v = \frac{V_p^2 - 2V_s^2}{2(V_p^2 - V_s^2)} \quad (20)$$

Another method to calculate brittleness index is according to the proportion of brittle minerals (quartz, carbonate) (Eq. (21)).

$$BI = (\mathrm{Qz} + \mathrm{Car})/(\mathrm{Qz} + \mathrm{Car} + \mathrm{Fels} + \mathrm{Clay}) \times 100\% \quad (21)$$

Qz is quartz content, Car is the carbonate content, Fels is the feldspar content, and Clay is the total clay content (Guo et al., 2015; Lai et al., 2015).

Brittle rock has a higher Young's modulus but lower Poisson's ratio due to high amount of brittle quartz and carbonate minerals (Rybacki et al., 2016; Iqbal et al., 2018; Kumar et al., 2018). Conversely, ductile rock with high clay content needs more energy/fracturing pressure to break (Iqbal et al., 2018).

5.2.2. Evaluation of engineering sweet spots

The brittleness index is calculated using Poisson- Young's method, and the *in situ* stress magnitudes are determined using the above equation. Geological sweet spots are characterized by high brittleness index but low horizontal stress difference, and the layers with high brittleness index easily sustain fracture aperture, while the intervals with low horizontal stress difference are favorable for formation of complex fracture network systems during hydraulic stimulation (Lai et al., 2022).

Consequently, the engineering sweet spots are also easily to be identified in the log profile, the layers $P_2I_2^2$ ($P_2I_2^{2\text{-}1}$, $P_2I_2^{2\text{-}2}$, $P_2I_2^{2\text{-}3}$) as well as $P_2I_1^2$ ($P_2I_1^{2\text{-}1}$, $P_2I_1^{2\text{-}2}$, $P_2I_1^{2\text{-}3}$) are typical geological and engineering sweet spots (Fig. 25). The comprehensive log evaluation of geological and engineering sweet spots will support decisions by engineers and geologists through the exploration and exploitation of unconventional oil and gas resources (Avanzini et al., 2016; Li et al., 2020; Lai et al., 2022).

6. Prospects

6.1. Extension of application of well logs

Well logs have been used in various aspects of geosciences and engineering fields. With increasing demands of industry and improvements of advanced well logging techniques, more areas require geophysical well logs to answer the scientific and technical questions. Actually, many of the fields that do not traditionally use well logs can reuse existing well log databases. For instance, CCUS are looking to reuse depressurized reservoirs as potentially storage for CO_2 or maybe as temporary storage for hydrogen. Actually, well logs have already been used in studies such as groundwater investigation (Maliva et al., 2009), geothermal potential assessment (Nasr et al., 2018; Shakirov et al., 2021), gas hydrate evaluation (Lee and Waite, 2008; Collett et al., 2011; Kang et al., 2020), coal bed methane exploitation (Liang et al., 2018; Karthikeyan et al., 2020), Milankovitch cycle recognition (Falahatkhah et al., 2021), paleoclimate and paleoenvironment reconstruction (Gould et al., 2014).

However, the applications of borehole geophysical logs in the above fields are at a relatively lower technological level. With increasing demands and technical improvements, the application of well logs will extend in more and more geological fields and engineering fields.

6.2. Improvements of advanced well logs

More and more advanced borehole geophysical logging techniques such as high definition induction log, ECS and LithoScanner log, electrical and sonic image logs, and NMR logs, are developed driven by the increasing demands in oil and gas industry, and these new well log suits will provide new insights to solve geological issues (Maliva et al., 2009; Collett et al., 2011). A series of advanced logging data are used to determine the occurrence of gas hydrates (Collett et al., 2011). In addition, horizontal well logging and logging while drilling data will be used to solve the geological issues.

A porosity histogram can be obtained by applying the Archie's formula to the flushed zone, and the porosity spectrum from an image log are used for reservoir quality prediction in carbonate rocks, and the high quality reservoirs have very broad porosity spectrum with long tails (Maliva et al., 2009). The fullbore image can be produced in the Techlog platform, and then a slab-like image can be created from image log by filling the image gap between pads and flaps (Fig. 26) (Kumar et al., 2014; Bize et al., 2015; Morelli et al., 2016). The colorful slab-like images are very similar with the core slab photos, and include much geological information. The slab-like, bright-yellow-bright images are due to the variation of mineral composition which can be determined by thin section observation, and slab images help pick out the bedding or lamina when the cores are not available (Fig. 26) (Morelli et al., 2016).

The ECS and LithoScanner log can directly provide the mineralogy of the rocks, and are used for mineral composition determination, lithology recognition, and even TOC calculation (Guo et al., 2019; Lai et al., 2022). However, ECS and LithoScanner logs still require some interpretation in sedimentary formations versus an igneous formation. Two-dimensional nuclear magnetic resonance (2D-NMR) logs, which provide lithology-independent T_1 (spin–lattice or longitudinal relaxation time), T_2 (pinspin or transverse relaxation time) distributions and diffusion coefficient, have advantages for petrophysical characterization differentiating bound and free fluids (water, gas, heavy and light oil) of shales and heterogeneous porous media (Du et al., 2020; Osogba et al., 2020; Yarmohammadi et al., 2020).

6.3. Artificial intelligence

To better fill the technologic gap between well logs and geological interpretation, artificial intelligence is introduced to improve the accuracy and speed, and diminish uncertainties. Big data science and artificial intelligence may provide new insights for accelerating data driven discovery in Earth evolution (Wang et al., 2021). The artificial intelligence helps unravel the hidden relations among various factors and discover controlling factors of a particular phenomenon (Hui et al., 2021; Lan et al., 2021). Machine learning algorithms, in particular deep learning (DL), which are subsets of artificial intelligent methods (Lv et al., 2021), are data-driven approaches providing automatic and fine

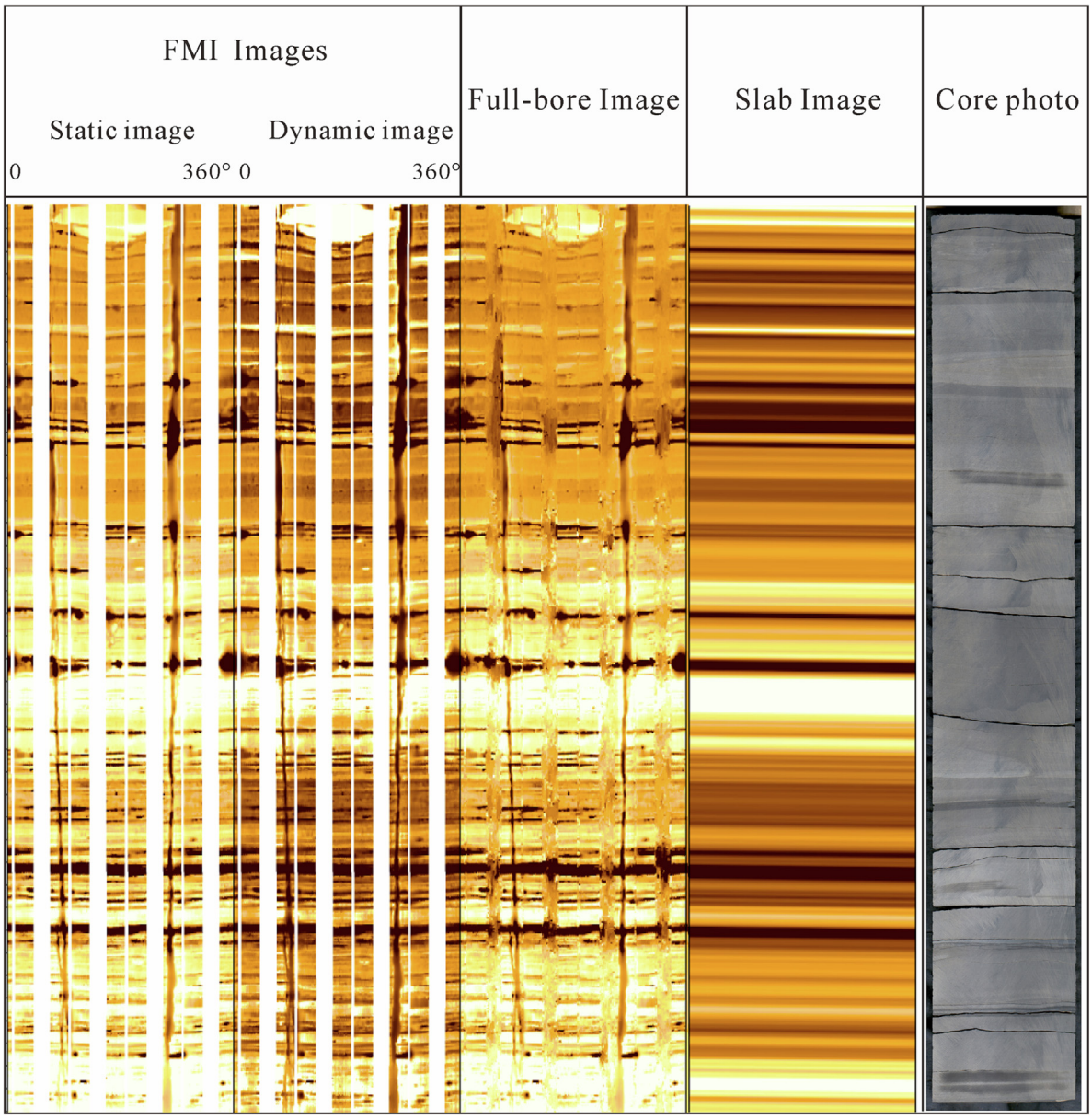

Fig. 26. Advanced image log processed procedures including static, dynamic image, fullbore image and slab image.

interpretation of scientific and technical issues efficiently (Dunham et al., 2020; Wood, 2020; Hui et al., 2021; Lan et al., 2021; Yu and Ma, 2021).

Over the past two decades there have been many attempts to use machine learning methods to generate pseudo log curves, calculate petrophysical parameters, predict lithofacies and enhance oil recovery (Zhang et al., 2018; Geng and Wang, 2020; Wood, 2020; Mahmoud et al., 2021; Tatsipie and Sheng, 2021). The application of AI in the links between well logs and geological interpretation will significantly reduce human workload and improve efficiency and accuracy (Wood, 2020; Amosu et al., 2021; Lv et al., 2021; Zhang et al., 2023).

(1) Construct a pseudo log curve

Well logs are in some cases missing, and Long Short-Term Memory (LSTM) network, convolutional neural network (CNN), recurrent neural networks (RNNs) and bidirectional long short-term memory (BiLSTM) can be used to generate synthetic well logs from the existing log data (Zhang et al., 2018; Osarogiagbon et al., 2020; Shan et al., 2021; Tatsipie and Sheng, 2021).

(2) Lithology and lithofacies prediction

Machine learning techniques including artificial neural networks (ANN), and functional neural networks (FNN) are used to predict the lithology changes (Mahmoud et al., 2021). Automatic interpretation of lithofacies via machine learning methods is feasible, as the data-driven machine learning method can model the complex relationship between rock properties and lithofacies (Al-Mudhafar, 2020; Feng, 2020), and artificial neural networks (Raeesi et al., 2012), supervised and unsupervised machine learning methods (Bhattacharya et al., 2016) are widely used for lithofacies interpretation using well logs (Al-Mudhafar, 2020; Feng, 2021).

(3) Recognition of pore, cavity and fracture

Carbonate rocks are heterogeneous, and have complex reservoir spaces (vugs, cavity and fracture) (Lan et al., 2021). A series of machine learning techniques (supervised support vector machine (Supervised-SVM) and supervised artificial neural network) can be applied to predict vugs, cavities and fractures using basic wireline logs (Haagsma et al., 2021; Lan et al., 2021).

(4) Permeability, porosity and TOC prediction

Direct logging interpretation of formation properties (porosity, permeability, water saturation) is time-consuming, and machine learning diminishes uncertainties and improves efficiency (Ao et al., 2019; Wood, 2020). There are no direct log curves used for permeability measurement, and neural network (Al Khalifah et al., 2020), support vector machine (SVM) (Al-Anazi and Gates, 2010), and principal component analysis networks (PCAN) are used for permeability prediction (Lv et al., 2021). The resistivity, sonic, density, and gamma ray logs are used to predict TOC in shales using SVM, ANN, and fully connected deep network (FCDN) methods (Shalaby et al., 2019; Handhal et al., 2020; Amosu et al., 2021; Zheng et al., 2021).

(5) Engineering fields

Application of artificial intelligence methods in various aspects of petroleum engineering is growing over time (Mahmoud et al., 2021). Machine learning approaches are widely used in the engineering fields of oil recovery enhancing (Kumar and Hassanzadeh, 2021), rock's mechanical property prediction (Mahmoud et al., 2021), and hydraulic fracturing (Hui et al., 2021).

The improvements of advanced well logs, and integration of future methods and technology may change workflows or solve outstanding geological problems that would yield great benefit in the near future.

7. Summary and conclusions

Geophysical well logging was invented in 1927, and the developments can be divided into four stages, and various series of well logging tools were developed to solve geological issues. Vertical resolutions, depth of investigation and applications of various well log suits are summarized, and the vertical resolution ranges from 5 mm to about 3.0 m. The depth of investigation ranges from micrometer to about 2.0 m. The conventional well logs and advanced well logs have their advantages and limitations, and can be used in various fields of geosciences.

Well logs are used in finding the hydrocarbon reservoirs and calculating petrophysical parameters. Well logs are used in basic geology in terms of structural geology, sedimentary geology and sequence stratigraphy. Structures around the borehole, which include unconformity surface, fault and fold, can be picked out by dipmeter log and image logs. Direction of *in situ* stress and stress magnitude can be derived from image logs and sonic logs. Fracture attitudes and status can be picked out from image logs. Geological and engineering sweet spots in unconventional oil and gas resources can be optimized using well logs through calculating brittleness index, *in situ* stress and petrophysical parameters. Lithology, lithofacies and depositional microfacies can be described and predicted by conventional well log curve values and shapes as well as image logs. The log curve shape and vertical stacking patterns as well as wavelet transformation can be used for sequence stratigraphy division.

Geophysical well logs are extending their application in groundwater investigation, geothermal energy assessment, gas hydrate evaluation, Milankovitch cycle recognition, and paleoenvironment reconstruction. With the rapid development of artificial intelligence, geophysical well logs are hoped to solve geological issues more efficiently.

CRediT authorship contribution statement

Jin Lai: Conceptualization, Methodology, Software, Data curation, Writing – original draft, Visualization, Investigation, Writing – review & editing. **Yang Su:** Conceptualization, Methodology, Software, Data curation, Writing – original draft. **Lu Xiao:** Data curation, Writing – original draft. **Fei Zhao:** Data curation, Writing – original draft. **Tianyu Bai:** Data curation, Writing – original draft. **Yuhang Li:** Conceptualization, Methodology, Software. **Hongbin Li:** Visualization, Investigation. **Yuyue Huang:** Visualization, Investigation. **Guiwen Wang:** Conceptualization, Methodology, Software, Writing – review & editing. **Ziqiang Qin:** Visualization, Investigation.

Declaration of competing interest

The authors declare that they have no known competing financial interests or personal relationships that could have appeared to influence the work reported in this paper.

Acknowledgments

This work is financially supported by National Natural Science Foundation of China (Grant No. 42002133), strategic cooperation project of PetroChina and CUPB (China University of Petroleum, Beijing) (ZLZX2020-01), and Science Foundation of China University of Petroleum, Beijing (No. 2462023QNXZ010). The authors would like to express their sincere thanks to the PetroChina Xinjiang, Tarim, Southwest and Changqing Oilfield Company for their assistance in providing data and for their technical input to this work.

References

Abuamarah, B.A., Nabawy, B.S., Shehata, A.M., Kassem, O.M.K., Ghrefat, H., 2019. Integrated geological and petrophysical characterization of Oligocene deep marine unconventional poor to tight sandstone gas reservoir. Mar. Pet. Geol. 109, 868–885.

Adebayo, A.R., Al-Yousef, H.Y., Mahmoud, M.A., 2015. An investigation of the effect of CO_2 –brine–rock interaction on determination of Archie's saturation exponent for carbon dioxide evaluation in carbonate reservoirs. J. Pet. Sci. Eng. 133 (335), 665–676.

Aghli, G., Soleimani, B., Moussavi-Harami, R., Mohammadian, R., 2016. Fractured zones detection using conventional petrophysical logs by differentiation method and its correlation with image logs. J. Pet. Sci. Eng. 142, 152–162.

Al Khalifah, H., Glover, P., Lorinczi, P., 2020. Permeability prediction and diagenesis in tight carbonates using machine learning techniques. Mar. Pet. Geol. 112, 104096.

Al-Anazi, A.F., Gates, I.D., 2010. Support-vector regression for permeability prediction in a heterogeneous reservoir: a comparative study. SPE Reserv. Eval. Eng. 13 (3), 485–495.

Allaud, L., Martin, M., 1977. Schlumberger: The History of a Technique. Wiley, New York.

Al-Mudhafar, W.J., 2020. Integrating machine learning and data analytics for geostatistical characterization of clastic reservoirs. J. Pet. Sci. Eng. 195, 107837.

Ameen, M.S., 2016. Fracture modes in the Silurian Qusaiba shale play, northern Saudi Arabia and their geomechanical implications. Mar. Pet. Geol. 78, 312–355.

Ameen, M.S., Hailwood, E.A., 2008. A new technology for the characterization of microfractured reservoirs (test case: Unayzah reservoir, Wudayhi field, Saudi Arabia). AAPG Bull. 92 (1), 31–52.

Ameen, M.S., MacPherson, K., Al-Marhoon, M.I., Rahim, Z., 2012. Diverse fracture properties and their impact on performance in conventional and tight-gas reservoirs, Saudi Arabia: The Unay. AAPG Bull. 96 (3), 459–492.

Amin, S., Wehner, M., Heidari, Z., Tice, M.M., 2021. Rock classification in the eagle ford formation through integration of petrophysical, geological, geochemical, and geomechanical characterization. AAPG Bull. 105 (7), 1357–1381.
Amosu, A., Imsalem, M., Sun, Y., 2021. Effective machine learning identification of TOC-rich zones in the Eagle Ford Shale. J. Appl. Geophys. 188, 104311.
Ao, Y., Li, H., Zhu, L., Ali, S., Yang, Z., 2019. The linear random forest algorithm and its advantages in machine learning assisted logging regression modeling. J. Pet. Sci. Eng. 174, 776–789.
Archie, G.E., 1942. The electrical resistivity log as an aid in determining some reservoir characteristics. Trans. AIME 146, 54–62.
Avanzini, A., Balossino, P., Brignoli, M., Spelta, E., Tarchiani, C., 2016. Lithologic and geomechanical facies classification for sweet spot identification in gas shale reservoir. Interpretation 4 (3), SL21–SL31.
Ayyad, H.M., Fathy, M., Hewaidy, A.G.A., Abdallah, A., 2020. Sequence stratigraphy of the Burdigalian Rudeis Formation in Ras El-Ush oil field, Gulf of Suez: application of gamma-ray analysis and biostratigraphy. Mar. Pet. Geol. 122, 104694.
Bai, Z., Tan, M., Li, G., Shi, Y., 2019. Analysis of low-resistivity oil pay and fluid typing method of Chang 8_1 Member, Yanchang Formation in Huanxian area, Ordos Basin, China. J. Pet. Sci. Eng. 175, 1099–1111.
Barton, C.A., Zoback, M.D., 2002. Discrimination of natural fractures from drilling-induced wellbore failures in wellbore image data-implications for reservoir permeability. SPE Reserv. Eval. Eng. 5, 249–254.
Bateman, R.M., 2020. Formation Evaluation with Pre-Digital Well Logs. Elsevier, Amsterdam, Netherlands.
Bauer, K., Kulenkampff, J., Henninges, J., Spangenberg, E., 2015. Lithological control on gas hydrate saturation as revealed by signal classification of NMR logging data. J. Geophys. Res.: Solid Earth 120, 6001–6017.
Bell, J.S., 1996. Petro geoscience 2. In situ stresses in sedimentary rocks (part 2): applications of stress measurements. Geosci. Can. 23 (3), 135–153.
Bhattacharya, S., Carr, T.R., Pal, M., 2016. Comparison of supervised and unsupervised approaches for mudstone lithofacies classification: case studies from the Bakken and Mahantango-Marcellus Shale, USA. J. Nat. Gas Sci. Eng. 33, 1119–1133.
Bize, E., Karoon, A.T., Laronga, R., Bize-Forest, N., 2015. Virtual Core: State-of-the-Art Wireline Technologies to Provide a Viable Substitute for Whole Conventional Coring. Presentation at the Offshore Technology Conference Brazil. Rio de Janeiro, Brazil, 27–29 October 2015. OTC-26206-MS.
Brekke, H., MacEachern, J.A., Roenitz, T., Dashtgard, S.E., 2017. The use of microresistivity image logs for facies interpretations: An example in point-bar deposits of the McMurray Formation, Alberta, Canada. AAPG Bull. 101 (5), 655–682.
Brudy, M., Zoback, M.D., 1999. Drilling-induced tensile wall-fractures: implications for determination of in situ stress orientation and magnitude. Int. J. Rock Mech. Min. Sci. 36, 191–215.
Carrasquilla, A., Lima, R., 2020. Basic and specialized geophysical well logs to characterize an offshore carbonate reservoir in the Campos Basin, southeast Brazil. J. S. Am. Earth. Sci. 98, 102436.
Catuneanu, O., Abreu, V., Bhattacharya, J.P., Blum, M.D., Dalrymple, R.W., Eriksson, P. G., Fielding, C.R., Fisher, W.L., Galloway, W.E., Gibling, M.R., Giles, K.A., Holbrook, J.M., Jordan, R., Kendall, C.G., St, C., Macurda, B., Martinsen, O.J., Miall, A.D., Neal, J.E., Nummedal, D., Pomar, L., Posamentier, H.W., Pratt, B.R., Sarg, J.F., Shanley, K. W., Steel, R.J., Strasser, A., Tucker, M.E., Winker, C., 2009. Towards the standardization of sequence stratigraphy. Earth-Sci. Rev. 92 (1–2), 1–33.
Chatterjee, R., Gupta, S.D., Farooqui, M.Y., 2012. Application of nuclear magnetic resonance logs for evaluating low-resistivity reservoirs: a case study from the Cambay basin, India. J. Geophys. Eng. 9 (5), 595.
Clavier, C., Coates, G., Dumanoir, J., 1984. Theoretical and experimental bases for the dual-water model for interpretation of shaly sands. Soc. Pet. Eng. J. 24 (2), 153–168.
Coates, G.R., Peveraro, R.C.A., Hardwick, A., Roberts, D., 1991. The magnetic resonance imaging log characterized by comparison with petrophysical properties and laboratory core data: Proceedings of the 66th Annual Technical Conference and Exhibition, Formation Evaluation and Reservoir Geology. SPE Reservoir Evaluation and Engineering, 22723, 627–635.
Coates, G.R., Xiao, L., Prammer, M.G., 1999. NMR Logging. Principle and Applications, Halliburton, Houston, TX.
Collett, T.S., Lewis, R.E., Winters, W.J., Lee, M.W., Rose, K.K., Boswell, R.M., 2011. Downhole well log and core montages from the Mount Elbert Gas Hydrate Stratigraphic Test Well, Alaska North Slope. Mar. Pet. Geol. 28, 561–577.
Dada, O.M., Awojoyogbe, O.B., Ukoha, A.C., 2015. A computational analysis for quantitative evaluation of petrol-physical properties of rock fluids based on Bloch NMR diffusion model for porous media. J. Pet. Sci. Eng. 127, 137–147.
Dixit, N.C., Hanks, C.L., Wallace, W.K., Ahmadi, M., Awoleke, O., 2017. In situ stress variations associated with regional changes in tectonic setting, northeastern Brooks Range and eastern North Slope of Alaska. AAPG Bull. 101 (3), 343–360.
Dong, T., Harris, N.B., Knapp, L.J., McMillan, J.M., Bish, D.L., 2018. The effect of thermal maturity on geomechanical properties in shale reservoirs: An example from the Upper Devonian Duvernay Formation, Western Canada Sedimentary Basin. Mar. Pet. Geol. 97, 137–153.
Donovan, A.D., 2010. The Sequence Stratigraphy Family Tree: Understanding the Portfolio of Sequence Methodologies. In: Ratcliffe, K.T., Zaitlin, B.A. (Eds.), Application of Modern Stratigraphic Techniques: Theory and Case Histories. SEPM Society for Sedimentary Geology, Volume 94. SEPM Special Publication. GeoScienceWorld, McLean, VA.
Donselaar, M.E., Schmidt, J.M., 2005. Integration of outcrop and borehole image logs for high-resolution facies interpretation: example from a fluvial fan in the Ebro Basin, Spain. Sedimentology 52, 1021–1042.
Du, Y., Fan, T., Machel, H.G., Gao, Z., 2018. Genesis of Upper Cambrian-Lower Ordovician dolomites in the Tahe oilfield, Tarim basin, NW China: several limitations from petrology, geochemistry, and fluid inclusions. Mar. Pet. Geol. 91, 43–70.
Du, Q., Xiao, L., Zhang, Y., Liao, G., Liu, H., Guo, J., 2020. A novel two-dimensional NMR relaxometry pulse sequence for petrophysical characterization of shale at low field. J. Magn. Reson. 310, 106643.
Dunham, M.W., Malcolm, A., Welford, J.K., 2020. Improved well log classification using semisupervised Gaussian mixture models and a new hyper-parameter selection strategy. Comput. Geosci. 140, 104501.
Eaton, B.A., 1969. Fracture gradient prediction and its application in oilfield operations. J. Pet. Technol. 246, 1353–1360.
Egbue, O., Kellogg, J., Aguirre, H., Torres, C., 2014. Evolution of the stress and strain fields in the Eastern Cordillera, Colombia. J. Struct. Geol. 58, 8–21.
Ellis, D.V., Singer, J.M., 2007. Well Logging for Earth Scientists. Springer, Dordrecht, The Netherlands.
Engelder, T., 1993. Stress Regimes in the Lithosphere. Princeton University Press, New Jersey.
Falahatkhah, O., Kordi, M., Fatemi, V., Koochi, H.H., 2021. Recognition of Milankovitch cycles during the Oligocene-Early Miocene in the Zagros Basin, SW Iran: Implications for paleoclimate and sequence stratigraphy. Sediment. Geol. 421, 105957.
Farrag, A.A., Ebraheem, M.O., Sawires, R., Ibrahim, H.A., Khalil, A.L., 2019. Petrophysical and aquifer parameters estimation using geophysical well logging and hydrogeological data, Wadi El-Assiuoti, Eastern Desert, Egypt. J. Afr. Earth Sci. 149, 42–54.
Feng, R., 2020. Lithofacies classification based on a hybrid system of artificial neural networks and hidden Markov models. J. Afr. Earth Sci. 221, 1484–1498.
Feng, R., 2021. Improving uncertainty analysis in well log classification by machine learning with a scaling algorithm. J. Pet. Sci. Eng. 196, 107995.
Folkestad, A., Veselovsky, Z., Roberts, P., 2012. Utilising borehole image logs to interpret delta to estuarine system: A case study of the subsurface Lower Jurassic Cook Formation in the Norwegian northern North Sea. Mar. Pet. Geol. 29, 255–275.
Geng, Z., Wang, Y., 2020. Physics-guided deep learning for predicting geological drilling risk of wellbore instability using seismic attributes data. Eng. Geol. 279, 105857.
Glover, P.W.J., Zadjali, I.I., Frew, K.A., 2006. Permeability prediction from MICP and NMR data using an electrokinetic approach. Geophysics 71 (4), F49–F60.
Goodall, T.M., Moller, N.K., Ronningsland, T.M., 1998. The integration of electrical image logs 237 with core data for improved sedimentological interpretation. Geol. Soc. London Spec. Pub. 136, 237–248.
Gould, K.M., Piper, D.J.W., Pe-Piper, G., MacRae, R.A., 2014. Facies, provenance and paleoclimate interpretation using spectral gamma logs: Application to the Lower Cretaceous of the Scotian Basin. Mar. Pet. Geol. 57, 445–454.
Gozalpour, F., Danesh, A., Todd, A.C., Tohidi, B., 2007. Application of tracers in oil-based mud for obtaining high-quality fluid composition in lean gas/condensate reservoirs. SPE Reserv. Eval. Eng. 10 (1), 5–11.
Grollimund, B., Zoback, M.D., Wiprut, D.J., Arnesen, L., 2001. Stress orientation, pore pressure and least principal stress in the Norwegian sector of the North Sea. Pet. Geosci. 7, 173–180.
Guo, Z., Li, X., Liu, C., Feng, X., Shen, Y., 2013. A shale rock physics model for analysis of brittleness index, mineralogy and porosity in the Barnett Shale. J. Geophys. Eng. 10 (2), 1742–2132.
Guo, P., Liu, C., Wang, L., Zhang, G., Fu, X., 2019. Mineralogy and organic geochemistry of the terrestrial lacustrine pre-salt sediments in the Qaidam Basin: Implications for good source rock development. Mar. Pet. Geol. 107, 149–162.
Guo, T., Zhang, S., Ge, H., Wang, X., Lei, X., Xiao, B., 2015. A new method for evaluation of fracture network formation capacity of rock. Fuel 140, 778–787.
Haagsma, A., Scharenberg, M., Keister, L., Schuetter, J., Gupta, N., 2021. Secondary porosity prediction in complex carbonate reefs using 3D CT scan image analysis and machine learning. J. Pet. Sci. Eng. 207, 109087.
Hamada, G.M., Al-Awad, M.N.J., 2000. Petrophysical evaluation of low resistivity sandstone reservoirs. J. Can. Pet. Tech. 39 (7), 7–14.
Hamada, N.M., Al-Blehed, A.S., Al-Awad, M.N., Al-Saddique, M.A., 2001. Petrophysical evaluation of low-resistivity sandstone reservoir with nuclear magnetic resonance log. J. Pet. Sci. Eng. 39 (2), 129–138.
Handhal, A.M., Al-Abadi, A.M., Chafeet, H.E., Ismail, M.J., 2020. Prediction of total organic carbon at Rumaila oil field, Southern Iraq using conventional well logs and machine learning algorithms. Mar. Pet. Geol. 116, 104347.
Hassani, A.H., Veyskarami, M., Al-Ajmi, A.M., Masihi, M., 2017. A modified method for predicting the stresses around producing boreholes in an isotropic in-situ stress field. Int. J. Rock Mech. Min. Sci. 96, 85–93.
He, J., Croix, A.D.L., Wang, J., Ding, W., Underschultz, J.R., 2019. Using neural networks and the Markov Chain approach for facies analysis and prediction from well logs in the Precipice Sandstone and Evergreen Formation, Surat Basin, Australia. Mar. Pet. Geol. 101, 410–427.
Herwanger, J.V., Bottrill, A.D., Mildren, S.D., 2015. Uses and abuses of the brittleness index with applications to hydraulic stimulation. Unconventional Resources Technology Conference, San Antonio, Texas. https://doi.org/10.15530/urtec-2015-2172545.

Hu, F.L., Zhou, C.C., Li, C.L., Xu, H.J., Zhou, F.M., Si, Z.W., 2012. Fluid identification method based on 2D diffusion-relaxation nuclear magnetic resonance (NMR). Pet. Explor. Dev. 39 (5), 591–596.
Hui, G., Chen, S., He, Y., Wang, H., Gu, F., 2021. Machine learning-based production forecast for shale gas in unconventional reservoirs via integration of geological and operational factors. J. Nat. Gas Sci. Eng. 94, 104045.
Iqbal, O., Ahmad, M., Kadir, A., 2018. Effective evaluation of shale gas reservoirs by means of an integrated approach to petrophysics and geomechanics for the optimization of hydraulic fracturing: A case study of the Permian Roseneath and Murteree Shale Gas reservoirs, Cooper Basin, Australia. J. Nat. Gas Sci. Eng. 58, 34–58.
Iqbal, M.A., Salim, A.M.A., Baioumy, H., Gaafar, G.R., Wahi, A., 2019. Identification and characterization of low resistivity low contrast zones in a clastic outcrop from Sarawak, Malaysia. J. Appl. Geophys. 160, 207–217.
Jarvie, D.M., Hill, R.J., Ruble, T.E., 2007. Unconventional shale-gas systems: the Mississippian Barnett Shale of north-central Texas as one model for thermogenic shale-gas assessment. AAPG Bull. 91, 475–499.
Ji, X., Wang, H., Ge, Y., Liang, J., Xu, X., 2022. Empirical mode decomposition-refined composite multiscale dispersion entropy analysis and its application to geophysical well log data. J. Pet. Sci. Eng. 208, 109495.
Josh, M., Esteban, L., Delle Piane, C., Sarout, J., Dewhurst, D.N., Clennell, M.B., 2012. Laboratory characterisation of shale properties. J. Pet. Sci. Eng. 88–89, 107–124.
Ju, W., Wang, K., 2018. A preliminary study of the present-day in-situ stress state in the Ahe tight gas reservoir, Dibei Gasfield, Kuqa Depression. Mar. Pet. Geol. 96, 154–165.
Ju, W., Shen, J., Qin, Y., Meng, S., Wu, C., Shen, Y., Yang, Z., Li, G., Li, C., 2017. In-situ stress state in the Linxing region, eastern Ordos basin, China: implications for unconventional gas exploration and production. Mar. Pet. Geol. 86, 66–78.
Kadkhodaie, A., Rezaee, R., 2017. Intelligent sequence stratigraphy through a wavelet-based decomposition of well log data. J. Nat. Gas Sci. Eng. 40, 38–50.
Kana, J.D., Djongyang, N., Raïdandi, D., Nouck, P.N., Dadjé, A., 2015. A review of geophysical methods for geothermal exploration. Renew. Sustain. Energy Rev. 44, 87–95.
Kang, D., Lu, J., Zhang, Z., Liang, J., Kuang, Z., Lu, C., Kou, B., Lu, Q., Wang, J., 2020. Fine-grained gas hydrate reservoir properties estimated from well logs and lab measurements at the Shenhu gas hydrate production test site, the northern slope of the South China sea. Mar. Pet. Geol. 122, 104676.
Karthikeyan, G., Jagadish, C., Rima, C., 2020. Impact of geomechanics in coal bed methane development and production, Barakar coals in central India. J. Pet. Sci. Eng. 194, 107515.
Keeton, G., Pranter, M., Cole, R.D., Gustason, E.R., 2015. Stratigraphic architecture of fluvial deposits from borehole images, spectral-gamma-ray response, and outcrop analogs, Piceance Basin, Colorado. AAPG Bull. 99 (10), 1929–1956.
Khair, H.A., Cooke, D., Hand, M., 2015. Paleo stress contribution to fault and natural fracture distribution in the Cooper Basin. J. Struct. Geol. 79, 31–41.
Khoshbakht, F., Memarian, H., Mohammadnia, M., 2009. Comparison of Asmari, Pabdeh and Gurpi formation's fractures, derived from image log. J. Pet. Sci. Eng. 67, 65–74.
Khoshbakht, F., Azizzadeh, M., Memarian, H., Nourozi, G.H., Moallemi, S.A., 2012. Comparison of electrical image log with core in a fractured carbonate reservoir. J. Pet. Sci. Eng. 86–87, 289–296.
Kosari, E., Ghareh-Cheloo, S., Kadkhodaie-Ilkhchi, A., Bahroudi, A., 2015. Fracture characterization by fusion of geophysical and geomechanical data: a case study from the Asmari reservoir, the Central Zagros fold-thrust belt. J. Geophys. Eng. 12, 130–143.
Kumar, S., Das, S., Bastia, R., Ojha, K., 2018. Mineralogical and morphological characterization of Older Cambay Shale from North Cambay Basin, India: Implication for shale oil/gas development. Mar. Pet. Geol. 97, 339–354.
Kumar, A., Laronga, R., Kherroubi, J., Bringer, F., Kear, G., Herrera, J., 2014. Visualizing Borehole Images in a Slabbed-Core Format: EAGE Borehole Geology Workshop, Dubai, United Arab Emirates, 12-15 October 2014, Paper BG20.
Kumar, A., Hassanzadeh, H., 2021. A qualitative study of the impact of random shale barriers on SAGD performance using data analytics and machine learning. J. Pet. Sci. Eng. 205, 108950.
LaGrange, M.T., Konhauser, K.O., Catuneanu, O., Harris, B.S., Playter, T.L., Gingras, M. K., 2020. Sequence stratigraphy in organic-rich marine mudstone successions using chemostratigraphic datasets. Earth-Sci. Rev. 203, 103137.
Lai, J., Wang, G., Fan, Q., Zhao, F., Zhao, X., Li, Y., Zhao, Y., Pang, X., 2023a. Towards the scientific interpretation of geophysical well logs: typical misunderstandings and countermeasures. Surv. Geophys. 44, 463–494.
Lai, J., Zhao, F., Zhang, M., Bai, T.Y., Huang, Y.Y., Li, D., Wang, G.W., Qin, Z.Q., 2023b. How high can fracture porosity become in the ultra-deep subsurface? Geosci. Front. 14, 101617.
Lai, J., Wang, G., Huang, L., Li, W., Ran, Y., Wang, D., Zhou, Z., Chen, J., 2015. Brittleness index estimation in a tight shaly sandstone reservoir using well logs. J. Nat. Gas Sci. Eng. 27, 1536–1545.
Lai, J., Wang, G., Ran, Y., Zhou, Z., Cui, Y., 2016. Impact of diagenesis on the petrophysical properties of tight oil reservoirs: The case of Upper Triassic Yanchang Formation Chang 7 oil layers in Ordos Basin, China. J. Pet. Sci. Eng. 145, 54–65.
Lai, J., Wang, G., Fan, Z., Wang, Z., Chen, J., Zhou, Z., Wang, S., Xiao, C., 2017. Fracture detection in oil-based drilling mud using a combination of borehole image and sonic logs. Mar. Pet. Geol. 84, 195–214.
Lai, J., Wang, G., Wang, S., Cao, J., Li, M., Pang, X., Han, C., Fan, X., Yang, L., He, Z., Qin, Z., 2018. A review on the applications of image logs in structural analysis and sedimentary characterization. Mar. Pet. Geol. 95, 139–166.
Lai, J., Li, D., Wang, G., Xiao, C., Hao, X., Luo, Q., Lai, L., Qin, Z., 2019a. Earth stress and reservoir quality evaluation in high and steep structure: The Lower Cretaceous in the Kuqa Depression, Tarim Basin, China. Mar. Pet. Geol. 101, 43–54.
Lai, J., Pang, X., Xu, F., Wang, G., Fan, X., Xie, W., Chen, J., Qin, Z., Zhou, Z., 2019b. Origin and formation mechanisms of low oil saturation reservoirs in Nanpu Sag, Bohai Bay Basin, China. Mar. Pet. Geol. 110, 317–334.
Lai, J., Wang, S., Zhang, C., Wang, G., Song, Q., Chen, X., Yang, K., Yuan, C., 2020. Spectrum of pore types and networks in the deep Cambrian to Lower Ordovician dolostones in Tarim Basin, China. Mar. Pet. Geol. 112, 104081.
Lai, J., Liu, S., Xin, Y., Wang, S., Xiao, C., Song, Q., Chen, X., Wang, G., Qin, Z., Ding, X., 2021. Geological-petrophysical insights in the deep Cambrian dolostone reservoirs in Tarim Basin, China. AAPG Bull. 105 (11), 2263–2296.
Lai, J., Wang, G., Fan, Q., Pang, X., Li, H., Zhao, F., Li, Y., Zhao, X., Zhao, Y., Huang, Y., Bao, M., Qin, Z., Wang, Q., 2022. Geophysical well log evaluation in the era of unconventional hydrocarbon resources: A review on current status and prospects. Surv. Geophys. 43, 913–957.
Lan, X., Zou, C., Kang, Z., Wu, X., 2021. Log facies identification in carbonate reservoirs using multiclass semi-supervised learning strategy. Fuel 302, 121145.
Laubach, S.E., 2003. Practical approaches to identifying sealed and open fractures. AAPG Bull. 87 (4), 561–579.
Laubach, S.E., Olson, J.E., Gale, J.F.W., 2004. Are open fractures necessarily aligned with maximum horizontal stress? Earth Planet. Sci. Lett. 222 (1), 191–195.
Laubach, S.E., Lander, R.H., Criscenti, L.J., Anovitz, L.M., Urai, J.L., Pollyea, R.M., Hooker, J.N., Narr, W., Evans, M.A., Kerisit, S.N., Olson, J.E., Dewers, T., Fisher, D., Bodnar, R., Evans, B., Dove, P., Bonnell, L.M., Marder, M.P., Pyrak-Nolte, L., 2019. The role of chemistry in fracture pattern development and opportunities to advance interpretations of geological materials. Rev. Geophys. 57 (3), 1065–1111.
Lee, M.W., Waite, W.F., 2008. Estimating pore-space gas hydrate saturations from well log acoustic data. Geochem. Geophys. Geosyst. 9, Q07008.
Li, X., Chen, Q., Liu, H., Wan, Y., Wei, L., Liao, J., Long, L., 2011. Features of sandy debris flows of the Yanchang Formation in the Ordos Basin and its oil and gas exploration significance. Acta Geol. Sin.-English Edition 85 (5), 187–1202.
Li, Y., Hu, Z., Cai, C., Liu, X., Duan, X., Chang, J., Li, Y., Mu, Y., Zhang, Q., Zeng, S., Guo, J., 2021. Evaluation method of water saturation in shale: a comprehensive review. Mar. Pet. Geol. 128, 105017.
Li, G., Li, G., Wang, Y., Qi, S., Yang, J., 2020. A rock physics model for estimating elastic properties of upper Ordovician-lower Silurian mudrocks in the Sichuan Basin, China. Eng. Geol. 266, 105460.
Liang, M., Peng, S., Du, W., Lu, Y., 2018. Tectonic stress estimation from ultrasonic borehole image logs in a coal bed methane well, northeastern Qinshui Basin, China. J. Nat. Gas Sci. Eng. 52, 44–58.
Liu, C.R., 2017. Theory of Electromagnetic Well Logging. Elsevier.
Liu, J., Dong, S., Zhang, L., Ma, Q., Wu, C., 2015. Estimation of archie parameters by a novel hybrid optimization algorithm. J. Pet. Sci. Eng. 135, 232–239.
Liu, J., Ding, W., Wang, R., Yang, H., Wang, X., Li, A., 2018. Correlation analysis of element contents and mechanical characteristics of shale reservoirs: A case study in the Cen'gong block, South China. Mar. Pet. Geol. 91, 19–28.
Liu, T., Ma, Z., Wang, J., Lv, H., 2005. Integrating MDT, NMR log and conventional logs for one-well evaluation. J. Pet. Sci. Eng. 46, 73–80.
Luthi, S., 2001. Geological Well Logs: Their Use in Reservoir Modeling. Springer-Verlag, Berlin Heidelberg New York.
Lv, A., Cheng, L., Aghighi, M.A., Masoumi, H., Roshan, H., 2021. A novel workflow based on physics-informed machine learning to determine the permeability profile of fractured coal seams using downhole geophysical logs. Mar. Pet. Geol. 131, 105171.
Magalhães, A.J.C., Raja Gabaglia, G.P., Fragoso, D.G.C., Bento Freire, E., Lykawka, R., Arregui, C.D., Silveira, M.M.L., Carpio, K.M.T., Gasperi, A.D., Pedrinha, S., Artagão, V.M., Terra, G.J.S., Bunevich, R.B., Roemers-Oliveira, E., Gomes, J.P., Hernández, J. I., Hernández, R.M., Bruhn, C.H.L., 2020. High-resolution sequence stratigraphy applied to reservoir zonation and characterisation, and its impact on production performance-shallow marine, fluvial downstream, and lacustrine carbonate settings. Earth-Sci. Rev. 210, 103325.
Mahmoud, A.A., Elkatatny, S., Al-AbdulJabbar, A., 2021. Application of machine learning models for real-time prediction of the formation lithology and tops from the drilling parameters. J. Pet. Sci. Eng. 203, 108574.
Maleki, S., Moradzadeh, A., Riabi, R.G., Sadaghzadeh, F., 2014. Comparison of several different methods of in situ stress determination. Int. J. Rock Mech. Min. Sci. 71 (71), 395–404.
Maliva, R.G., Clayton, E.A., Missimer, T.M., 2009. Application of advanced borehole geophysical logging to managed aquifer recharge investigations. Hydrogeol. J. 17 (6), 1547–1556.
Mansour, A., Mohamed, O., Tahoun, S.S., Elewa, A.M.T., 2018. Sequence stratigraphy of the Raha Formation, Bakr Oil Field, Gulf of Suez, Egypt: Insights from electrical well log and palynological data. J. Afr. Earth Sci. 139, 205–221.
Marzan, I., Martí, D., Lobo, A., Alcalde, J., Ruiz, M., Alvarez-Marron, J., Carbonell, R., 2021. Joint interpretation of geophysical data: Applying machine learning to the modeling of an evaporitic sequence in Villar de Canas (Spain). Eng. Geol. 288, 106126.
Massiot, C., Mcnamara, D.D., Lewis, B., 2015. Processing and analysis of high temperature geothermal acoustic borehole image logs in the Taupo volcanic zone, New Zealand. Geothermics 53, 190–201.
Melo, A.H., Magalhães, A.J.C., Menegazzo, M.C., Fragoso, D.G.C., Florencio, C.P., Lima-Filho, F.P., 2021. High-resolution sequence stratigraphy applied for the improvement of hydrocarbon production and reserves: A case study in

Cretaceous fluvial deposits of the Potiguar basin, northeast Brazil. Mar. Pet. Geol. 130, 105124.
Moreau, J., Joubert, J.B., 2016. Glacial sedimentology interpretation from borehole image log: Example from the Late Ordovician deposits, Murzuq Basin (Libya). Interpretation 4 (2), B1–B16.
Morelli, C., Kodaira, C., Irie, S., 2016. Maximize the value of image log data and core samples: how to utilize geological data. The 22Nd Formation Evaluation Symposium of Japan.
Movahed, Z., Junin, R., Safarkhanlou, Z., Akbar, M., 2014. Formation evaluation in Dezful embayment of Iran using oil-based-mud imaging techniques. J. Pet. Sci. Eng. 121, 23–37.
Muniz, M.C., Bosence, D.W.J., 2015. Pre-salt microbialites from the campos basin (offshore Brazil): image log facies, facies model and cyclicity in lacustrine carbonates. Geol. Soc. London Spec. Pub. 418, 221–242.
Nabawy, B.S., 2015. Impacts of the pore- and petro-fabrics on porosity exponent and lithology factor of Archie's equation for carbonate rocks. J. Afr. Earth Sci. 108, 101–114.
Nabawy, B.S., El Sharawy, M.S., 2018. Reservoir assessment and quality discrimination of Kareem Formation using integrated petrophysical data, Southern Gulf of Suez, Egypt. Mar. Pet. Geol. 93, 230–246.
Nabawy, B.S., Géraud, Y., 2016. Impacts of pore- and petro-fabrics, mineral composition and diagenetic history on the bulk thermal conductivity of sandstones. J. Afr. Earth Sci. 115, 48–62.
Nabawy, B.S., Rochette, P., Géraud, Y., 2010. Electric pore fabric of the Nubia sandstones in south Egypt: Characterization and modelling. J. Afr. Earth Sci. 183 (2), 681–694.
Najibi, A.R., Ghafoori, M., Lashkaripour, G.R., Asef, M.R., 2017. Reservoir geomechanical modeling: In-situ stress, pore pressure, and mud design. J. Pet. Sci. Eng. 151, 31–39.
Nasr, M., Raymond, J., Malo, M., Gloaguen, E., 2018. Geothermal potential of the St. Lawrence Lowlands sedimentary basin from well log analysis. Geothermics 75, 68–80.
Nie, X., Zou, C., Pan, L., Huang, Z., Liu, D., 2013. Fracture analysis and determination of in-situ stress direction from resistivity and acoustic image logs and core data in the Wenchuan Earthquake Fault Scientific Drilling Borehole-2 (50–1370 m). Tectonophysics 593, 161–171.
Olatinsu, O.B., Olorode, D.O., Clennell, B., Esteban, L., Josh, M., 2017. Lithotype characterizations by nuclear magnetic resonance (NMR): A case study on limestone and associated rocks from the Eastern Dahomey basin, Nigeria. J. Afr. Earth Sci. 129, 701–712.
Osarogiagbon, A.U., Oloruntobi, O., Khan, F., Venkatesan, R., Butt, S., 2020. Gamma ray log generation from drilling parameters using deep learning. J. Pet. Sci. Eng. 195, 107906.
Osogba, O., Misra, S., Xu, C., 2020. Machine learning workflow to predict multi-target subsurface signals for the exploration of hydrocarbon and water. Fuel 278, 118357.
Ozkan, A., Cumella, S.P., Milliken, K.L., Laubach, S.E., 2011. Prediction of lithofacies and reservoir quality using well logs, Late Cretaceous Williams Fork Formation, Mamm Creek field, Piceance Basin, Colorado. AAPG Bull. 95 (10), 1699–1723.
Pan, B., Wang, X., Guo, Y., Zhang, L., Ruhan, A., Zhang, N., Zhang, P., Li, Y., 2022. Study on reservoir characteristics and evaluation methods of altered igneous reservoirs in Songliao Basin, China. J. Pet. Sci. Eng. 212, 110266.
Pang, X., Wang, G., Kuang, L., Li, H., Zhao, Y., Li, D., Zhao, X., Wu, S., Feng, Z., Lai, J., 2022. Insights into the pore structure and oil mobility in fine-grained sedimentary rocks: The Lucaogou Formation in Jimusar Sag, Junggar Basin, China. Mar. Pet. Geol. 137, 105492.
Passey, Q., Creaney, S., Kulla, J., Moretti, F., Stroud, J., 1990. A practical model for organic richness from porosity and resistivity logs. AAPG Bull. 74, 1777–1794.
Podugu, N., Goswami, D., Akkiraju, V.V., Roy, S., 2023. In-situ physical and elastic properties of Archaean basement granitoids in the Koyna seismogenic zone, western India from 3 km downhole geophysical well logs: Implications for water percolation at depth. Tectonophysics 848, 229725.
Poupon, A., Leveaux, J., 1971. Evaluation of water saturation in shaly formations. SPWLA 12 Annual Logging Symposium.
Poupon, A., Loy, M.A., Tixier, M.P., 1954. A ccontribution to electrical log interpretation in shaly sands. J. Pet. Technol. 6 (6), 27–34.
Prioul, R., Donald, A., Koepsell, R., Marzouki, Z.E., Bratton, T., 2007. Forward modeling of fracture-induced sonic anisotropy using a combination of borehole image and sonic logs. Geophysics 72 (4), 135–147.
Qin, Z., Pan, H., Ma, H., Konaté, A.A., Hou, M., Luo, S., 2016. Fast prediction method of Archie's cementation exponent. J. Nat. Gas Sci. Eng. 34, 291–297.
Qiu, X., Liu, C., Mao, G., Deng, Y., Wang, F., Wang, J., 2014. Late Triassic tuff intervals in the Ordos basin, Central China: Their depositional, petrographic, geochemical characteristics and regional implications. J. Asian Earth Sci. 80, 48–160.
Radwan, A.A., Nabawy, B.S., Abdelmaksoud, A., Lashin, A., 2021. Integrated sedimentological and petrophysical characterization for clastic reservoirs: A case study from New Zealand. J. Nat. Gas Sci. Eng. 88, 103797.
Raeesi, M., Moradzadeh, A., Ardejani, F.D., Rahimi, M., 2012. Classification and identification of hydrocarbon reservoir lithofacies and their heterogeneity using seismic attributes, logs data and artificial neural networks. J. Pet. Sci. Eng. 82–83, 151–165.
Rajabi, M., Sherkati, S., Bohloli, B., Tingay, M., 2010. Subsurface fracture analysis and determination of in-situ stress direction using FMI logs: An example from the Santonian carbonates (Ilam Formation) in the Abadan Plain, Iran. Tectonophysics 492, 192–200.
Rajabi, M., Tingay, M., Heidbach, O., 2016. The present-day state of tectonic stress in the darling basin, Australia: implications for exploration and production. Mar. Pet. Geol. 77, 776–790.
Ran, Y., Wang, G.W., Zhou, Z.L., Lai, J., Dai, Q.Q., Chen, J., Fan, X.Q., Wang, S.C., 2016. Identification of lithology and lithofacies type and its application to Chang 7 tight oil in Heshui area, Ordos Basin. Geol. China 43 (4), 1331–1340 (in Chinese with English abstract).
Rezaee, R., Saeedi, A., Clennell, B., 2012. Tight gas sands permeability estimation from mercury injection capillary pressure and nuclear magnetic resonance data. J. Pet. Sci. Eng. 88–89, 92–99.
Rickman, R., Mullen, M.J., Petre, J.E., Grieser, B., Kundert, D., 2008. A practical use of shale petrophysics for stimulation design optimization: all shale plays are not clones of the Barnett Shale. SPE Annual Technical Conference and Exhibition. Society of Petroleum Engineers.
Rider, M.H., 2002. The Geological Interpretation of Well Logs. Sutherland, Scotland, p. 280.
Rybacki, E., Meier, T., Dresen, G., 2016. What controls the mechanical properties of shale rocks? Part II: Brittleness. J. Pet. Sci. Eng. 144, 39–58.
Sarhan, M.A., 2019. Seismic delineation and well logging evaluation for Albian Kharita Formation, South West Qarun (SWQ) field, Gindi Basin, Egypt. J. Afr. Earth Sci. 158, 103544.
Schlumberger, 1981. Dipmeter interpretation. Volume 1- Fundamentals. Schlumberger, New York.
Schlumberger, 1989. Log Interpretation Principles and Applications, Schlumberger Educational Services.
Schlumberger, 2004. Schlumberger WTA Marketing Service: FMI Fullbore Formation MicroImager. Schlumberger Educational Services, Houston, Texas, 2 pp.
Schlumberger, 2006. ECS Elemental Capture Spectroscopy Sonde. Schlumberger, Houston, TX.
Schlumberger, 2013. Log Interpretation Charts. Schlumberger Publication.
Schultz, R., Skoumal, R.J., Brudzinski, M.R., Eaton, D., Baptie, B., Ellsworth, W., 2020. Hydraulic fracturing-induced seismicity. Rev. Geophys. 58, e2019RG000695.
Serra, O., 1984. Fundamentals of Well-log Interpretation. Elsevier, Amsterdam, The Netherlands.
Serra, O., 1989. Formation Microscanner Image Interpretation. Schlumberger Educational Services, Houston Texas, p. 117.
Sfidari, E., Sharifi, M., Amini, A., Zamanzadeh, S.M., Kadkhodaie, A., 2021. Reservoir quality of the Surmeh (Arab-D) reservoir in the context of sequence stratigraphy in Salman Field. Persian Gulf. J. Pet. Sci. Eng. 198, 108180.
Shakirov, A., Chekhonin, E., Popov, Y., Popov, E., Spasennykh, M., Zagranovskaya, D., Serkin, M., 2021. Rock thermal properties from well-logging data accounting for thermal anisotropy. Geothermics 92, 102059.
Shalaby, M.R., Jumat, N., Lai, D., Malik, O., 2019. Integrated TOC prediction and source rock characterization using machine learning, well logs and geochemical analysis: Case study from the Jurassic source rocks in Shams Field, NW Desert, Egypt. J. Pet. Sci. Eng. 176, 369–380.
Shan, L., Liu, Y., Tang, M., Yang, M., Bai, X., 2021. CNN-BiLSTM hybrid neural networks with attention mechanism for well log prediction. J. Pet. Sci. Eng. 205, 108838.
Shazly, T.F., Tarabees, E., 2013. Using of dual laterolog to detect fracture parameters for Nubia Sandstone Formation in Rudeis-Sidri area, Gulf of Suez, Egypt. Egypt. J. Petrol. 22, 313–319.
Simandoux, P., 1963. Dielectric Measurements on Porous Media Application to the Measurement of Water Saturations: Study of the Behaviour of Argillaceous Formations vol. 18, 193–215.
Sondergeld, C.H., Newsham, K.E., Comisky, J.T., 2010. Petrophysical considerations in evaluating and producing shale gas resources. SPE Unconventional Gas Conference. Society of Petroleum Engineers.
Souza, A.C.B., Nascimento, Jr. D.R., Filho, F.N., Batezelli, A., Santos, F.H., Oliveira, K.M. L., Almeida, N.M., 2021. Sequence stratigraphy and organic geochemistry: An integrated approach to understand the anoxic events and paleoenvironmental evolution of the Ceara basin, Brazilian Equatorial margin. Mar. Pet. Geol. 129, 105074.
Stadtmuller, M., Lis-Sledziona, A., Słota-Valim, M., 2018. Petrophysical and geomechanical analysis of the Lower Paleozoic shale formation, North Poland. Interpretation 6 (3), SH91–SH106.
Tan, M., Wang, P., Mao, K., 2014. Comparative study of inversion methods of three-dimensional NMR and sensitivity to fluids. J. Appl. Geophys. 103 (4), 12–30.
Tatsipie, N.R.K., Sheng, J.J., 2021. Generating pseudo well logs for a part of the upper Bakken using recurrent neural networks. J. Pet. Sci. Eng. 200, 108253.
Tiab, D., Donaldson, E.C., 2004. Petrophysics: Theory and Practice of Measuring Reservoir Rock and Fluid Transport Properties. Second Edition. Elsevier. https://doi.org/10.1016/B978-0-7506-7711-0.X5000-2.
Tingay, M.R.P., Hillis, R.R., Morley, C.K., King, R.C., Swarbrick, R.E., Damit, A.R., 2009. Present-day stress and neotectonics of Brunei: implications for petroleum exploration and production. AAPG Bull. 93, 75–100.
Tokhmchi, B., Memarian, H., Rezaee, M.R., 2010. Estimation of the fracture density in fractured zones using petrophysical logs. J. Pet. Sci. Eng. 72, 206–213.
Verweij, J.M., Boxem, T.A.P., Nelskamp, S., 2016. 3D spatial variation in vertical stress in on- and offshore Netherlands; integration of density log measurements and basin modeling results. Mar. Pet. Geol. 78, 870–882.
Wang, C., Hazen, R.M., Cheng, Q., Stephenson, M.H., Zhou, C., Fox, P., Shen, S., Oberhansli, R., Hou, Z., Ma, X., Feng, Z., Fan, J., Ma, C., Hu, X., Luo, B., Wang, J., Schiffries, C.M., 2021. The Deep-Time Digital Earth program: data-driven discovery in geosciences. Natl. Sci. Rev. 8, nwab027.

Wang, G.W., Xu, J.L., Yang, N., Lai, J., Zhao, X.L., 2013b. Using wavelet frequency analysis to divide sedimentary sequence cycles and isochronous correlation. Geol. J. China Univ. 19 (1), 70–77.
Wang, G.W., Lai, J., Liu, B.C., Fan, Z.Y., Liu, S.C., Shi, Y.J., Zhang, H.T., Chen, J., 2020. Fluid property discrimination in dolostone reservoirs using well logs. Acta Geol. Sin.-Engl. Edit. 94 (3), 831–846.
Wang, J., Wang, H., Chen, H., Jiang, S., Zhao, S., 2013a. Responses of two lithosomes of Lower Cretaceous coarse clastic rocks to tectonism in Kuqa foreland sub–basin, Northern Tarim Basin, Northwest China. Sediment. Geol. 289, 182–193.
Wang, H., Wu, W., Chen, T., Dong, X., Wang, G., 2019. An improved neural network for TOC, S1 and S2 estimation based on conventional well logs. J. Pet. Sci. Eng. 176, 664–678.
Wennberg, O.P., Casini, G., Jonoud, S., Peacock, D.C.P., 2016. The characteristics of open fractures in carbonate reservoirs and their impact on fluid flow: a discussion. Pet. Geosci. 22, 91–104.
Wilson, M.E.J., Lewis, D., Yogi, O., Holland, D., Hombo, L., Goldberg, A., 2013. Development of a Papua New Guinean onshore carbonate reservoir: a comparative borehole image (BHI) and petrographic evaluation. Mar. Pet. Geol. 44, 164–195.
Wilson, T.H., Smith, V., Brown, A., 2015. Developing a model discrete fracture network, drilling, and enhanced oil recovery strategy in an unconventional naturally fractured reservoir using integrated field, image log, and three-dimensional seismic data. AAPG Bull. 99 (4), 735–762.
Wood, D., 2020. Predicting porosity, permeability and water saturation applying an optimized nearest-neighbour, machine-learning and data-mining network of well-log data. J. Pet. Sci. Eng. 184, 106587.
Worthington, P.F., 2000. Recognition and evaluation of low-resistivity pay. Pet. Geosci. 6 (1), 77–92.
Xiang, M., Wang, Z., Liu, J., 2015. Extracting array acoustic logging signal information by combining fractional Fourier transform and Choi-Williams distribution. Appl. Acoust. 90, 111–115.
Xu, C., 2007. Interpreting shoreline sands using borehole images—A case study of the Cretaceous Ferron sands in Utah. AAPG Bull. 91, 1319–1338.
Xu, C., Cronin, T.P., McGinness, T.E., Steer, B., 2009. Middle Atokan sediment gravity flows in the Red Oak field, Arkoma Basin, Oklahoma: A sedimentary analysis using electrical borehole images and wireline logs. AAPG Bull. 93 (1), 1–29.
Xu, C., Gehenn, J.M., Zhao, D., Xie, G., Teng, M.K., 2015. The fluvial and lacustrine sedimentary systems and stratigraphic correlation in the Upper Triassic Xujiahe Formation in Sichuan Basin, China. AAPG Bull. 99 (11), 2023–2041.
Xu, J., Zhang, B., Qin, Y., Cao, G., Zhang, H., 2016. Method for calculating the fracture porosity of tight-fracture reservoirs. Geophysics 81 (4), IM57-IM70.
Yang, Z., Zou, C., Hou, L., Wu, S., Lin, S., Luo, X., Zhang, L., Zhao, Z., Cui, J., Pan, S., 2019. Division of fine-grained rocks and selection of "sweet sections" in the oldest continental shale in China: Taking the coexisting combination of tight and shale oil in the Permian Junggar Basin. Mar. Pet. Geol. 109, 339–348.
Yao, Y., Liu, D., Che, Y., Tang, D., Tang, S., Huang, W., 2009. Non-destructive characterization of coal samples from China using microfocus X-ray computed tomography. Int. J. Coal Geol. 80 (2), 113–123.
Yarmohammadi, S., Kadkhodaie, A., Hosseinzadeh, S., 2020. An integrated approach for heterogeneity analysis of carbonate reservoirs by using image log based porosity distributions, NMR T_2 curves, velocity deviation log and petrographic studies: A case study from the South Pars gas field, Persian Gulf Basin. J. Pet. Sci. Eng. 192, 107283.
Yu, S., Ma, J., 2021. Deep learning for geophysics: current and future trends. Rev. Geophys. 59, e2021RG000742.
Zaree, V., Riahi, M.A., Khoshbakht, F., Hemmati, H.R., 2016. Estimating fracture intensity in hydrocarbon reservoir: an approach using DSI data analysis. Carbonates Evaporites 31, 101–107.
Zazoun, R.S., 2013. Fracture density estimation from core and conventional well logs data using artificial neural networks: The Cambro-Ordovician reservoir of Mesdar oil field, Algeria. J. Afr. Earth Sci. 83, 55–73.
Zeng, L., Liu, H., 2010. Influence of fractures on the development of low-permeability sandstone reservoirs: A case study from the Taizhao district, Daqing Oilfield, China. J. Pet. Sci. Eng. 72, 120–127.
Zhang, J., 2011. Pore pressure prediction from well logs: Methods, modifications, and new approaches. Earth-Sci. Rev. 108 (1–2), 50–63.
Zhang, D.X., Chen, Y.T., Meng, J., 2018. Synthetic well logs generation via recurrent neural networks. Pet. Explor. Dev. 45 (4), 598–607.
Zhang, H., Wu, W., Wu, H., 2023. TOC prediction using a gradient boosting decision tree method: A case study of shale reservoirs in Qinshui Basin. J. Pet. Sci. Eng. 221, 111271.
Zhao, Y.L., Ge, S.Q., Han, C., Mo, J., Shuai, S.C., Wei, G., Pan, F., 2019b. Application of new-generation oil-based microresistivity image logs in evaluating low-porosity sandstone reservoir in Kuqa Depression. Well Logging Technol. 43 (5), 514–518 (in Chinese).
Zhao, J., Tang, D., Qin, Y., Xu, H., 2018. Experimental study on structural models of coal macrolithotypes and its well logging responses in the Hancheng area, Ordos Basin, China. J. Pet. Sci. Eng. 166, 658–672.
Zhao, X., Zhou, L., Pu, X., Han, W., Jin, F., Xiao, D., Shi, Z., Deng, Y., Zhang, W., Jiang, W., 2019a. Exploration breakthroughs and geological characteristics of continental shale oil: A case study of the Kongdian Formation in the Cangdong Sag, China. Mar. Pet. Geol. 102, 544–556.
Zheng, D., Wu, S., Hou, M., 2021. Fully connected deep network: An improved method to predict TOC of shale reservoirs from well logs. Mar. Pet. Geol. 132, 105205.
Zhu, L., Ma, Y., Cai, J., Zhang, C., Wu, S., Zhou, X., 2022. Key factors of marine shale conductivity in southern China—Part II: The influence of pore system and the development direction of shale gas saturation models. J. Pet. Sci. Eng. 209, 109516.
Zoback, M., Barton, C., Brudy, M., Castillo, D., Finkbeiner, T., Grollimund, B., Moos, D., Peska, P., Ward, C., Wiprut, D., 2003. Determination of stress orientation and magnitude in deep wells. Int. J. Rock Mech. Min. Sci. 40, 1049–1076.
Zoback, M.D., Moose, D., Mastin, L., Anderson, R.N., 1985. Well-bore breakouts and in situ stress. J. Geophys. Res. 90, 5523–5538.
Zoback, M., Townend, J., 2001. Implications of hydrostatic pore pressures and high crustal strength for the deformation of intraplate lithosphere. Tectonophysics 336 (1–4), 19–30.
Zou, C.N., Wang, L., Li, Y., Tao, S., Hou, L.H., 2012. Deep-lacustrine transformation of sandy debrites into turbidites, Upper Triassic, Central China. Sediment. Geol. 265–266, 143–155.
Zou, C.N., Zhu, R., Chen, Z., Ogg, J.G., Wu, S., Dong, D., Qiu, Z., Wang, Y., Wang, L., Lin, S., Cui, J., Su, L., Yang, Z., 2019. Organic-matter-rich shales of China. Earth-Sci. Rev. 189, 51–78.